A STUDY TO EVALUATE SCALES IN SOME TURBULENT FLOWS IN VIEW OF QUANTIC BEHAVIOR OF TURBULENCE USING EXPERIMENTAL RESULTS

A THESIS SUBMITTED TO
THE GRADUATE SCHOOL OF NATURAL AND APPLIED SCIENCES
OF
MIDDLE EAST TECHNICAL UNIVERSITY

BY

ELIF BEKOĞLU

IN PARTIAL FULFILLMENT OF THE REQUIREMENTS
FOR
THE DEGREE OF MASTER OF SCIENCE
IN
AEROSPACE ENGINEERING

AUGUST 2021

Approval of the thesis:

A STUDY TO EVALUATE SCALES IN SOME TURBULENT FLOWS IN VIEW OF QUANTIC BEHAVIOR OF TURBULENCE USING EXPERIMENTAL RESULTS

submitted by **ELIF BEKOĞLU** in partial fulfillment of the requirements for the degree of **Master of Science in Aerospace Engineering Department, Middle East Technical University** by,

Prof. Dr. Halil Kalıpçılar
Dean, Graduate School of **Natural and Applied Sciences** _____

Prof. Dr. İsmail Hakkı Tuncer
Head of Department, **Aerospace Engineering** _____

Prof. Dr. Mehmet Cevdet Çelenligil
Supervisor, **Aerospace Engineering, METU** _____

Prof. Dr. Cahit Çıray
Co-supervisor, **Aerospace Engineering, METU** _____

Examining Committee Members:

Prof. Dr. Hasan Umur Akay
Mechanical Engineering, Atılım University _____

Prof. Dr. Mehmet Cevdet Çelenligil
Aerospace Engineering, METU _____

Prof. Dr. Kahraman Albayrak
Mechanical Engineering, METU _____

Prof. Dr. Oğuz Uzol
Aerospace Engineering, METU _____

Prof. Dr. Cahit Çıray
Aerospace Engineering, METU _____

23.08.2021:

I hereby declare that all information in this document has been obtained and presented in accordance with academic rules and ethical conduct. I also declare that, as required by these rules and conduct, I have fully cited and referenced all material and results that are not original to this work.

Name, Surname: Elif Bekoğlu

Signature :

ABSTRACT

A STUDY TO EVALUATE SCALES IN SOME TURBULENT FLOWS IN VIEW OF QUANTIC BEHAVIOR OF TURBULENCE USING EXPERIMENTAL RESULTS

Bekoğlu, Elif
M.S., Department of Aerospace Engineering
Supervisor: Prof. Dr. Mehmet Cevdet Çelenligil
Co-Supervisor: Prof. Dr. Cahit Çıray

August 2021, 124 pages

The knowledge of the energy contents, sizes, and lifetimes of eddies is necessary to understand the structure of turbulent flows. The spectral approach can provide the frequency-dependent energy spectrum, which helps to find out this structure. The present study focuses on finding eddy sizes or wavelengths using the frequency-dependent energy spectrum, which is consistent with the physics of turbulence. This is because the eddy size is related to wavenumber. The turbulence studies in the literature use a dispersion relation that connects frequency to wavenumber. The mentioned dispersion relation is generally used based on Taylor's hypothesis, and examples of this usage are frequently encountered in the literature. Nevertheless, this approach has some deficiencies and limitations. As a result of this, several studies in the literature have tested and made corrections to this hypothesis. Some of them have tried to find alternative methods.

The present thesis study includes the application of an alternative approach named Quantic Behavior of Turbulence (QBT) proposed by Çıray [69, 70, 72]. With this

approach, the nature of turbulence is explained with a dual character, including particle and wavy character. The mathematical procedure offered by this approach finds wavenumber to corresponding frequency.

Within this study, the first step has been an implementation of this method to a Matlab code. This computer code uses the spectral approach to obtain the spectrum in the frequency domain. After that, the wavenumbers are provided by pursuing the mathematical procedure of QBT. Then, several different types of turbulent flows have been analyzed by this code. As a consequence of these analyses, the spectrum in the wavenumber domain is obtained in accordance with the data from the literature. With this approach, results such as sizes, lifespans, and energy contents of eddies are calculated in conformity with physical behavior. It is aimed that this approach and this study can contribute to more accurate understandings and solutions of turbulence problems.

Keywords: the physics of turbulence, length scales, eddy sizes, energy spectrum

ÖZ

DENEYSEL SONUÇLARI KULLANARAK TÜRBÜLANSIN KUANTİK DAVRANIŞI YAKLAŞIMIYLA BAZI TÜRBÜLANSLI AKIMLARDA ÖLÇEKLERİ DEĞERLENDİRMEYE YÖNELİK BİR ÇALIŞMA

Bekoğlu, Elif
Yüksek Lisans, Havacılık ve Uzay Mühendisliği Bölümü
Tez Yöneticisi: Prof. Dr. Mehmet Cevdet Çelenligil
Ortak Tez Yöneticisi: Prof. Dr. Cahit Çıray

Ağustos 2021 , 124 sayfa

Günümüzde türbülanslı akımların yapısını anlamak için; türbülansı oluşturan çevrintilerin boyutları, ömür süreleri ve enerji içeriklerinin bilinmesi gerekmektedir. Spektral yaklaşım, bu yapının bulunmasına yardımcı olan, frekansa bağlı enerji spektrumunun elde edilmesini sağlayabilir. Bu tez çalışmasında, türbülansın fiziği ile tutarlı olan frekansa bağlı enerji spektrumu kullanılarak, çevrintilerin boyutlarının yani dalga boylarının bulunmasına odaklanılmaktadır. Bunun nedeni, türbülanslı akımlardaki çevrintilerin boyutlarının, dalga boyu ve dolayısıyla dalga sayısı ile ilişkili olmasıdır. Literatürdeki türbülansa yönelik çalışmalar, dalga sayısını elde etmek için frekans ve dalga sayısı arasındaki saçılım ilişkisini kullanmaktadır. Bahsedilen saçılım ilişkisi genellikle Taylor'ın donuk türbülans yaklaşımına dayanmaktadır ve literatürde, bu ilişkinin kullanıldığı çalışmalara sıklıkla rastlanılmaktadır. Fakat, bu yaklaşımın bazı eksiklikleri ve sınırlamaları bulunmaktadır. Bu yüzden, literatürde bu metot ile ilgili birçok çalışma bulunmaktadır. Bu çalışmaların bir kısmı metodu test ederken, bir kısmı metot üzerinde düzeltme yapmakta ve diğer çalışmalar ise bu me-

toda alternatif yöntem aramaktadır.

Mevcut tez çalışması, C. Çıray tarafından önerilen ve Taylor'ın yaklaşımına alternatif olarak ortaya çıkmış olan Türbülansın Kuantik Davranışı metodunun uygulamalarından oluşmaktadır [69, 70, 72]. Bu metot, türbülansın doğasını, parçacık ve dalga karakteri de dahil olmak üzere ikili bir karakter ile açıklamaktadır ve her bir frekansa karşılık gelen dalga sayısının bulunabilmesi için matematiksel hesaplama prosedürü sunmaktadır.

Mevcut tez çalışmasının ilk adımı, bu metodun Matlab kodu haline getirilmesidir. Bahsedilen kod, frekansa bağlı enerji spektrumunu elde etmek amacıyla spektral yaklaşımı kullanmaktadır. Sonrasında, alternatif metodun matematiksel prosedürü takip edilerek her bir frekansa karşılık gelen dalga sayıları elde edilir. Bu çalışmada, bahsedilen kod kullanılarak, çeşitli türbülanslı akım deneylerinin analizi yapılmıştır. Bu analizlerin sonucu olarak, dalga sayısına bağlı enerji spektrumu, literatürdeki çalışmalarla uyumlu bir şekilde elde edilmiştir. Böylece, çevrintilerin boyutları, ömürleri ve enerji içerikleri de türbülansın fiziksel davranışına uygun olarak hesaplanmıştır. Literatüre C. Çıray tarafından kazandırılan bu yaklaşımla ve bu yaklaşımın farklı akımlara uygulanmasıyla, türbülansın fiziğinin daha doğru anlaşılması ve türbülansa yönelik endüstriyel problemlerin çözümüne katkıda bulunulması hedeflenmiştir.

Anahtar Kelimeler: türbülansın fiziği, uzunluk ölçekleri, çevrinti boyutları, enerji spektrumu

To esteemed Prof. Dr. Cahit Çıray,

who has influenced me the most

in every sense...

ACKNOWLEDGMENTS

First of all, I would like to thank my advisor, Prof. Dr. Cahit Çıray. In the last four years that I have known him, I have been very honored to take his courses and continue my master's study with him. Prof. Dr. Cahit Çıray's perspective, motivation, guidance, and endless support taught me a lot, not just academically but in many ways. He made me understand better what kind of person and academician I want to be. Thanks to his teachings, I learned that good things can always be done with hard work and not by giving up.

I would also like to express my deep gratitude to Prof. Dr. M. Cevdet Çelenligil. I am grateful to him for his support, interest, and his detailed feedback.

I appreciate Dr. Eda Doğan very much for sharing the experimental data of her doctoral studies with us. I am especially grateful to her for her care, attentive and pleasant feedback, and kind support.

In addition, I would like to thank Anas Abdulrahim, M. Tuğrul Akpolat, Abdelrahman Hassanein for sharing the experimental data they measured for their studies, and RÜZGEM, that made this possible. I especially thank the department secretary Derya Kaya for her kind help.

I am grateful to my family, especially my mother and sister, for their endless support over the years. I hope I would be as strong as my mother and my sister, and I could give them the same support now and in the future.

I would especially like to send my warmest thanks to İzzet Tarık Tandoğan. His presence and unlimited support are so precious to me. My deepest thanks are also for my dear friends, Merve Eşdur, Çiğdem Ekiz and Deniz Bilgin. I am so glad for our togetherness and support for each other, in good and bad times. I believe that together we can overcome anything. I would also like to thank my friends Ilgın Çolak, Turgay Kaya and İlknur Çoban for their support and the joyful times we spent together.

TABLE OF CONTENTS

LIST OF TABLES

TABLES

LIST OF FIGURES

FIGURES

LIST OF ABBREVIATIONS

ABBREVIATIONS

ABL	Atmospheric Boundary Layer
CPU	Central Processing Unit
DFT	Discrete Fourier Transform
DNS	Direct Numerical Simulation
FFT	Fast Fourier Transform
FST	Freestream Turbulence
LES	Large Eddy Simulation
LHS	Left-hand-side
N-S	Navier-Stokes
PDF	Probability Density Function
PIV	Particle Image Velocimetry
QBT	Quantic Behavior of Turbulence
RANS	Reynolds Averaged Navier-Stokes
RHS	Right-hand-side
1-D	1 Dimensional
3-D	3 Dimensional

SYMBOLS

ROMAN SYMBOLS

$a(\eta)$	Fourier coefficient of cosine term (real part) in continuous form, [m]
a_f	Fourier coefficient of cosine term in the code, [m/s]
a_η	Fourier coefficient of cosine term (real part) in discrete form, [m/s]
$b(\eta)$	Fourier coefficient of sine term (imaginary part) in continuous form, [m]
b_f	Fourier coefficient of sine term in the code, [m/s]
b_η	Fourier coefficient of sine term (imaginary part) in discrete form, [m/s]
c	Phase velocity, [m/s]
f	Frequency, [Hz]
f_c	Nyquist critical frequency, [Hz]
k	Wavenumber, [m^{-1}]
n	Determined number by QBT for each data, [-]
t	Time, [s]
t_L	Lifespan of eddy, [s]
u	Instantaneous fluctuation velocity in x-direction, [m/s]
u'	Root-mean-square (rms) of instantaneous velocity fluctuations in x-direction, [m/s]
u_t	Discrete sample data, [m/s]
x	Non-dimensional instantaneous fluctuation velocity in x-direction, [-]
y	Non-dimensional instantaneous velocity in x-direction, [-]
A	Constant property of PDF, [-]
B	Determined number by QBT for each data, [-]

D	Diameter, [in.]
$E(k)$	Energy density per unit wavenumber, [m^3/s^2]
G	Any property of an eddy, [-]
$G(f)$	Normalized frequency-dependent energy spectrum function, [s]
I	Turbulence intensity, [-]
I_{act}	Actual turbulence intensity found from experimental data, [-]
I_{calc}	Calculated turbulence intensity by QBT, [-]
L	Integral scale, [m]
M	Mesh size of grids, [cm, in.]
N	The number of discrete data, [-]
$P(x)$	Probability density function (PDF) in terms of x, [-]
$P(y)$	Probability density function (PDF) in terms of y, [-]
$P(1)$	Constant property of PDF, [-]
$P_L(x)$	LHS of PDF in terms of x, [-]
$P_R(x)$	RHS of PDF in terms of x, [-]
Re_λ	Reynolds number based on Taylor microscale, [-]
Re_x	Reynolds number based on streamwise distance, x, [-]
SR	Sampling rate, [Hz]
Q_E	Correlation function, [m^2/s^2]
T	Period, [s]
U	Instantaneous velocity in x-direction, [m/s]
$\overline{U}$	Mean velocity in x-direction, [m/s]
U_c	Convective velocity, [m/s]
U_η	Fourier transform of u_t, [-]
$\overline{V}$	Mean velocity in y-direction, [m/s]
$\overline{W}$	Mean velocity in z-direction, [m/s]

GREEK SYMBOLS

ϵ	Viscous dissipation rate, [m^2/s^3]
η	Frequency, [Hz]
η_k	Kolmogorov scale, [mm]
κ_1	Wavenumber in longitudional direction, [mm]
λ	Taylor microscale, [cm]
μ^κ	Normalized κ^{th} moment, [-]
${\mu_{act}}^2$	Normalized actual 2^{nd} order moment found from experimental data, [-]
${\mu_{calc}}^2$	Normalized calculated 2^{nd} order moment by QBT, [-]
ν	Kinematic viscosity, [m^2/s]
ξ	Any variable, [-]
ω	Circular frequency, [rad/s]
Δ	Sampling interval, [s]

OTHER SYMBOLS

$k-\epsilon$	Turbulence kinetic energy, [m^2/s^2] - Viscous dissipation rate, [m^2/s^3]
$k-\omega$	Turbulence kinetic energy, [m^2/s^2] - Specific rate of dissipation, [s^{-1}]

CHAPTER 1

INTRODUCTION

1.1 Turbulence and Length Scales

A large part of the flows observed in nature and those created in laboratories or industrial applications are turbulent flows for most of the cases. In other words, from the water flowing in the tap to the ocean currents, from the natural gas carried by pipes to the flow surrounding cars, airplanes, submarines, ships are all turbulent flows. It is understood that turbulent flow has a wide range of appearances in nature and the applications in industry [86]. These flows can cover large and small space dimensions. The widespread existence of turbulent flow requires understanding its physics and solving it mathematically in many engineering applications. Even today, there does not seem to exist a unified theory for turbulent flows.

Turbulent flow has a random character in essence. This means that all turbulent flow properties are random functions of time and space, that motion is unpredictable. This description, which distinguishes turbulence from laminar, was observed by Reynolds with his historical experiments and was introduced in [73, 74]. Reynolds also gave at the same time governing equations of turbulent flow, called today Reynolds Averaged Navier-Stokes (RANS) equations. In this approach, any instantaneous quantity is separated into mean (time-averaged) and fluctuation parts. Then, Navier-Stokes (N-S) equations are written with these separated quantities, and the average of these equations is taken. The difference from the RANS and N-S equations can be classified with three items:

(i) Instantaneous quantities seem to be replaced by the average quantities.

(ii) The nonlinear terms in N-S equations give nonlinear combinations of the correlations of the fluctuating velocity, which are called Reynolds stresses. These terms represent the transport of momentum due to turbulent fluctuations [53].

(iii) In spite of the fact that turbulent flow is essentially random in character, RANS equations are deterministic [62]. Since the statistical values of turbulent flow properties are deterministic functions that depend on time and space [16], they are used in RANS equations. This is also called statistical approach [58].

It is clear that to be able to solve RANS equations, one needs to know the distribution of Reynolds stress term in the interested domain. This term is the average of the products of fluctuation velocities in different directions. Its space derivative appears in the momentum equation. However, this term is not easy to calculate. In order to be able to measure velocities in different directions at the same time and obtain their space derivative, measurements should be made in more than one location and for more than one direction. Considering that the experimental uncertainty and measurement probes will also affect the flow, it is challenging to measure this term realistically by experiment. As a result, another method to obtain Reynolds stresses is needed, and modeling them is found as a solution.

One of the first studies for turbulence models is Boussinesq's hypothesis, published in 1877 [9], and provides an expression that allows calculating the Reynolds stress tensor. This assumption relates shear stress to mean velocity gradients and a new defined constant, eddy viscosity. Later, the mixing length approach was proposed by Taylor and Prandtl at the same time [83], [64]. This approach is almost the same as the Boussinesq hypothesis. The different point is that eddy viscosity is not a fixed value and depends on the turbulent length scale, which is a flow-dependent variable [16]. Knowledge of this scale is required by eddy viscosity based turbulence models such as Spalart-Allmaras, $k-\epsilon$, and $k-\omega$ [79]. More detailed information about this scale is given in the following parts.

Many turbulence models, including the mentioned ones, are used frequently in literature. These models are based on semi-empirical equations and use several correction constants obtained by experiments. Since they have no strong physical background, they give satisfying results for specific cases and those with boundary conditions sim-

ilar to these cases. Another critical point is that it is not possible to understand the effects of turbulence fluctuations using these turbulence models. Therefore, an alternative method, Large Eddy Simulation (LES), is suggested to solve this problem. The turbulent flow consists of coherent turbulent structures at different sizes named eddies, which are discussed later. While the large eddies are affected by the boundary conditions of flow, small eddies are universal for all turbulent flows if the Reynolds number is sufficiently high. LES tries to simulate the instantaneous properties of the flow in the interested domain considering the energy contribution of large eddies. Even though LES models small scales and may not represent large eddies exactly [16], it is important to understand turbulence structure, especially large eddies. Because in order to solve turbulence problems more accurately, a better understanding of turbulence is a necessity.

The mentioned coherent structure of turbulence, *eddy*, is a group of fluid molecules that act within a particular group for a period of time, and the group personality is preserved during this time [72]. The concept of personality is perceived in different ways. For instance, while Prandtl assumes personality as momentum, Taylor takes it as vorticity [71]. That is, turbulent flow is expressed as the movement of eddies. In a turbulent flow, eddies of different sizes and different levels of kinetic energy exist. Energy transfer between eddies was described as an energy cascade by Richardson in 1922 [75]. By this definition, the largest eddies are born due to the effects of boundary conditions of flow. These eddies divide, forming smaller eddies and transferring their energy to the eddies created by this division. The process continues in this manner until the smallest eddies are formed. Finally, the smallest eddies disappear by viscous dissipation.

A correct comprehension of energy transfer and viscous dissipation mechanism mentioned in specific turbulent flow cases is important for obtaining an accurate solution. This circumstance creates a requirement of obtaining sizes and energy contributions of all eddies. In literature, eddy sizes are associated with the wavelengths, so wavenumbers. Therefore, the energy contributions of eddies are represented as an energy spectrum in the wavenumber domain, as given in Fig. 1.1. The first region includes large eddies, and these eddies create velocity fluctuations in low frequency. They are mostly affected by the boundary conditions of flow. As it can be seen from

Fig. 1.1, these eddies are in the largest sizes. So, they correspond to the smallest wavenumber values. The second region is related to the energetic eddies. Their energy density, $E(k)$, is very high and has a peak in this region. These eddies are represented by the integral scale, L, as eddy size. This scale is comparable to the characteristic length of flow, such as diameter for pipe flow, chord for flow around an airfoil. The universal equilibrium region is the last in the energy spectrum. Kolmogorov introduced two similarity hypotheses about this region in 1941 [46].

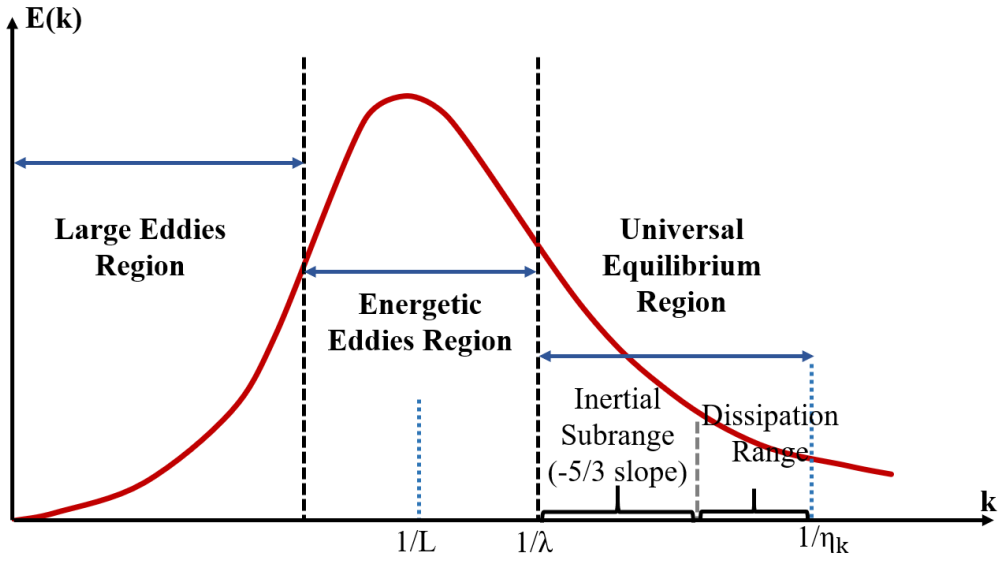

Figure 1.1: Regions of the energy spectrum where $E(k)$ is the energy density, and k is wavenumber reproduced from Figure XIV. 20 in [16]

The first hypothesis says that the statistics of the small-scale motions are universal. The only condition is being Reynolds number sufficiently high. If it is performed, small-scale motions are independent of the boundary conditions of flow and universal. In the second hypothesis, inertial subrange under the universal equilibrium range is defined, and in this region, the energy dissipation rate is independent of viscosity. In inertial subrange, energy density, $E(k)$ is found as proportional to $k^{-5/3}$. This region is represented by the Taylor microscale, λ [84]. The second subrange of this universal equilibrium range consists of the dissipating eddies. The viscous dissipation occurs very rapidly. The representative length scale of this region is the Kolmogorov scale, η_k as shown in Fig. 1.1.[1]

[1] Although the Kolmogorov scale is indicated with η in the literature, it is shown with symbol η_k in this study to avoid any symbolic problems.

The regions of the energy spectrum can be understood better on a logarithmic scale, as shown in Fig. 1.2. The axes of the spectrum are plotted as non-dimensional. In the large eddies region, the difference of boundary conditions of the flows is more apparent. However, the inertial subrange has a $-5/3$ slope for all cases, and the dissipating eddies also have the same behavior.

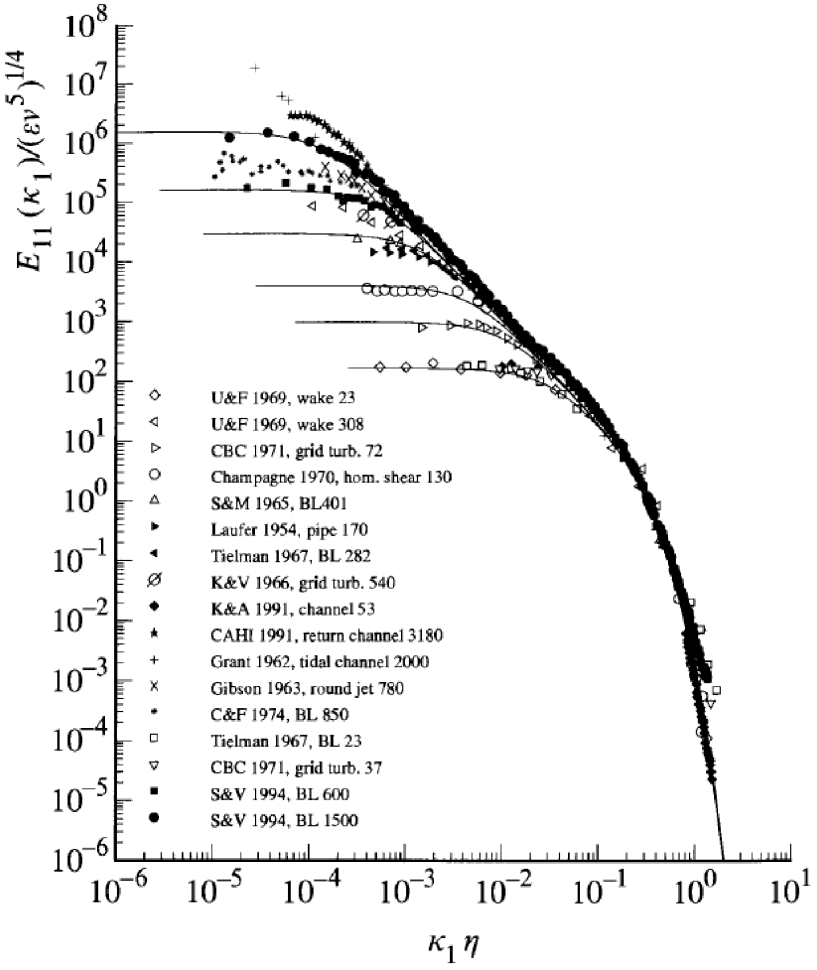

Figure 1.2: 1-D longitudinal scaled energy spectrum of different experiments on logarithmic scale, $Re_\lambda = 30, 70, 130, 300, 600, 1500$ (lines from down to up) where $E(\kappa_1)/(\epsilon\nu^5)^{1/4}$ is a non-dimensional spectrum function, ϵ is viscous dissipation rate, ν is kinematic viscosity, and κ_1 is wavenumber in longitudinal direction [62]. Experimental data is provided by [4, 13, 17, 18, 36, 38, 44, 50, 77, 78, 87, 89].

Another issue that should be mentioned is how to obtain a wavenumber-dependent

energy spectrum. Firstly, from experimental data of instantaneous velocity fluctuations, frequency-dependent energy spectrum can be obtained by Fourier series analysis. Fourier transform methods can be used for this purpose, such as Discrete Fourier Transform (DFT) or Fast Fourier Transform (FFT). After transforming data to the frequency domain from the time domain, a dispersion relation that relates frequency and wavenumber is required. Taylor proposed a dispersion relation based on his frozen turbulence hypothesis [84]. This relation is widely used in literature. The details and use of this theory in literature are explained in the next subsection. Also, its applications and accuracy are evaluated because this thesis is based on applying a different approach to some flow cases, which is an alternative to Taylor's hypothesis.

1.2 Literature Review on Taylor's Frozen Turbulence Hypothesis

The development of technology affects the solutions of fluid mechanics problems and makes solutions more accurately. Computer simulations allow the evaluation of entire flow fields and make turbulence phenomena more understandable. But still, turbulence problems maintain their difficulty. One of the main problems is that there does not seem to exist an applicable model for all turbulent flow cases. Another problem is the need for the energy contributions and sizes of the eddies in existing turbulence models solutions.

Taylor proposed that turbulence can be assumed frozen for special cases, such as homogeneous and isotropic turbulence [84]. Therefore, the temporal and spatial gradients can be associated, and eddy sizes can be obtained by a dispersion relation that comes from this association. This assumption is based on the idea that if the velocity fluctuations are small compared to mean velocity, the temporal gradient at a fixed point in space is created by the spatial gradient due to mean velocity [55]. Physically, it means that this hypothesis is useful if the timescale of eddies is larger than the time to pass through the sensor [63].

Assume that G is a property of a turbulent flow at location $\xi - \Delta\xi$ and time $t - \Delta t$ as shown in Fig. 1.3. According to Taylor's frozen turbulence hypothesis, property G is moved to location ξ with a constant velocity $\overline{U}$ in time Δt in the x-direction **without**

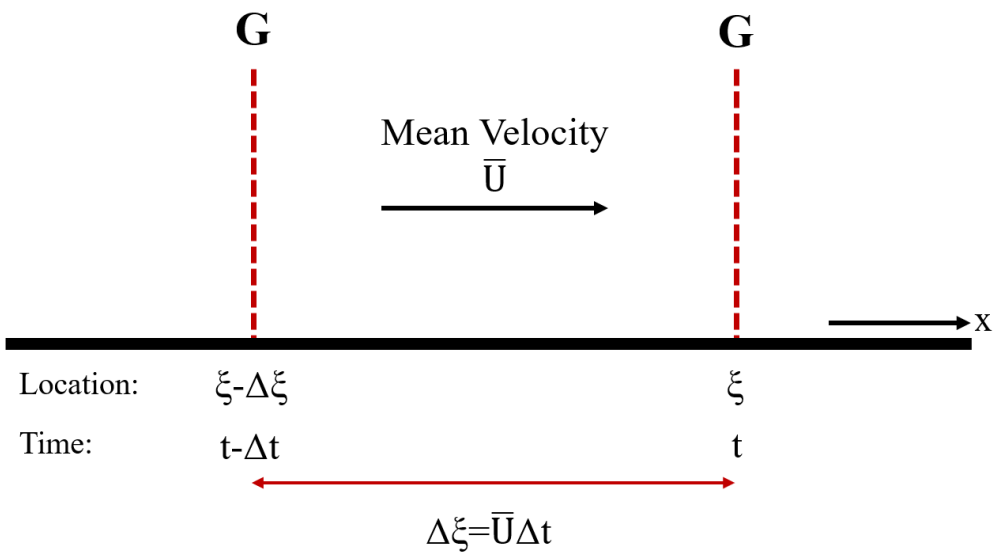

Figure 1.3: The representation of Taylor's frozen turbulence hypothesis reproduced from Figure XIV. 17 in [16]

any change [16]. So if the turbulence at the location $\xi - \Delta\xi$ is frozen, property G is only the function of space. In contrast, the temporal variation of G at location ξ and time t is due to mean velocity $\overline{U}$ to carry the frozen turbulence. This situation can be expressed mathematically as:

$$G(t)\Big|_{\xi} = G(\xi - \overline{U}\Delta t) \; . \tag{1.1}$$

Also, a new parameter η_T is defined as $\eta_T = \xi - \overline{U}\Delta t$. Then, the time derivative of the equality in Eqn. 1.1 is taken,

$$\frac{\partial G}{\partial t}\bigg|_{\xi} = \lim_{\Delta t \to 0} \frac{\Delta G}{\Delta t}\bigg|_{\xi} = \lim_{\Delta t \to 0} \frac{\Delta G}{\Delta \eta_T} . \frac{\Delta \eta_T}{\Delta t} \; . \tag{1.2}$$

For $\Delta t \to 0$,

$$\lim_{\Delta t \to 0} \frac{\Delta G}{\Delta \eta_T} = \frac{\partial G}{\partial \xi}\bigg|_{\xi} , \qquad \frac{\Delta \eta_T}{\Delta t} = -\overline{U} \; . \tag{1.3}$$

Therefore, Eqn. 1.2 can be written as:

$$\frac{\partial G}{\partial t} = -\overline{U}\frac{\partial G}{\partial \xi} \; , \tag{1.4}$$

This is the mathematical representation of Taylor's frozen turbulence hypothesis.

Also, Eqn. 1.4 can be expressed as:

$$\frac{\partial G}{\partial t} + \overline{U}\frac{\partial G}{\partial \xi} = 0 \quad \rightarrow \quad \frac{DG}{Dt} = 0 \; . \tag{1.5}$$

So, the total derivative of G is zero [16]. In other words, property G does not change while following the fluid particles according to this hypothesis. As can be seen from Eqn. 1.4, the mean velocity $\overline{U}$ becomes convective velocity. Thus, the dispersion relation and wavelength, L, based on Taylor's hypothesis are,

$$k = \frac{\omega}{\overline{U}} \; , \tag{1.6a}$$

$$L = \frac{\overline{U}}{\omega} = \frac{1}{k} \; , \tag{1.6b}$$

where k is wavenumber and ω is circular frequency, $\omega = 2\pi f$, and f is frequency. Consequently, wavenumber (wavelength, it is assumed to correspond to the eddy size in the literature) can be calculated by Taylor's frozen turbulence hypothesis. It should be pointed out that this hypothesis is valid for homogenous and isotropic turbulence at the low-intensity level and uniform mean flow. When the literature on this hypothesis is reviewed, it is observed that this hypothesis is widely used. Unfortunately, several researchers showed that this hypothesis is not satisfactory.

Lee et al. applied this hypothesis to the grid-generated (decaying) compressible turbulent flow and compared results with those of experiments and Direct Numerical Simulations (DNS) [51]. They computed turbulence statistics such as space-time correlations of fluctuations in velocity, vorticity, and dilatation. They observed that this hypothesis agrees well with the simulations and experiments for the incompressible part. However, according to their results, this hypothesis does not perform well for the compressible part. Lin questioned the accuracy of applying Taylor's hypothesis to shear flows theoretically [52]. He emphasized that the size and properties of eddies change significantly due to the shear effect. He concluded that pressure and nonlinear terms cannot be neglected, and therefore it would not be correct to use this hypothesis in shear flow. Heskestad proposed an alternative relation for shear flows allowing high turbulent intensities to compute the mean-square space derivative from the mean-square time derivative using hotwire techniques [42]. In this relation, unlike the Taylor hypothesis, the instantaneous velocity is taken as convective velocity. He performed tests of turbulent plane jet to check his relation and observed that it gives accurate results at only high Reynolds numbers.

Turbulent flow properties are usually expressed by the velocity correlations in space, time and space-time. Therefore, especially in flows with high turbulent intensity, the fluctuation velocity, which is constantly changing, should be taken into account in calculations, as well as the mean flow. Fisher and Davies conducted the experiments at the mixing region of a jet using hotwire anemometer [32]. They observed the significant difference between the convection velocity and average velocity for high turbulence intensity. Also, they concluded that the convective velocity cannot be determined as a single value for the entire domain. Zaman et al. studied the convenience of Taylor's hypothesis on large-scale turbulent structures in a circular air jet [99]. They compared spatial distributions of turbulent flow properties obtained using their hotwire measurements at different locations and Taylor's hypothesis. It is noticed that this hypothesis gives accurate results if the turbulent flow structures are not interacting with each other and there are no rapid changes. However, if these conditions exist, the significant distortions of convective velocity from mean velocity are observed. Also, they checked if the convection velocity is taken as local mean or instantaneous velocity. They concluded that when the large-scale structures are observed, none of these velocities and Taylor's hypothesis gives accurate results.

The following table is a list of convective velocities as observed or proposed by different researchers [37]. The ratios of convective velocity, U_c, to the mean velocity, U_0, and the specific flow cases in which they are used and regions or conditions specified are given in Table 1.1.

Table 1.1: Convective velocities used in the literature [37] where D is diameter and M is mesh size of grids.

Flow field	Reference	Region or Condition	U_c/U_0
Round jet	Bradshaw (1967) [10]	noise production region	0.10 - 0.80
	Brunn (1977) [11]	-	0.60 - 0.68
	Davies (1963) [21]	potential core	0.20 - 0.61
		mix region	
	Lau (1975) [49]	-	0.63 - 0.69

Table 1.1 Continued: Convective velocities used in the literature [37] where D is diameter and M is mesh size of grids.

Flow field	Reference	Region or Condition	U_c/U_0
Round jet	Davis (1975) [22]	supersonic	$0.40 - 0.70$
	Wills (1964) [93]	D = 2 in.	0.10 - 0.80
	Wilson (1970) [94]	D = 1 in.	0.667
	Wygnanski (1969) [96]	D = 1.04 in.	0.40 - 1.05
	Wooldridge (1972) [95]	core and mixing region D = 1.5 in.	0.68
	Ko (1971) [45]	D = 2.5 in.	0.65 - 0.75
Boundary layer	Favre (1967) [31]	-	0.80 - 1.28
	Kovasznay (1970) [47]	-	0.93
	Bull (1967) [12]	-	0.53 - 0.825
	Blackwelder (1977) [8]	-	0.80
	Willmarth (1962) [92]	-	0.56 - 0.83
Grid	Favre (1965) [30]	M = 1 in.	1.0
	Comte-Bellot (1971) [18]	M = 5.08 cm	1.0
	Sepri (1976) [81]	Heated grid	≥ 1.0
	Frenkiel (1966) [33]	M = 2.54 cm	1.0
Pipe	Baldwin (1961) [6]	Centre-line D = 8 in.	1.16
	Heidrick (1971) [40]	Near wall center-line D = 3.1 in.	> 1.0
	Willmarth (1959) [91]	D = 4 in.	0.82
	Corcos (1962) [20]	-	0.80 - 0.90
	McConachie (1981) [54]	-	0.75 - 1.12
Homogeneous shear flow	Champagne (1970) [13]	-	~ 1.0
Atmospheric	Antonia (1979) [3]	-	0.58 - 0.89

Table 1.1 Continued: Convective velocities used in the literature [37] where D is diameter and M is mesh size of grids.

Flow field	Reference	Region or Condition	U_c/U_0
Supersonic wake flow	Demetriades (1976) [26]	-	~ 1.0
Wake of disk	Oswald (1971) [59]	-	0.99
2-D Mixing region	Wygnanski (1970) [97]	-	0.85
	Batt (1977) [7]	-	< 1
Wall jet	Chanaud (1970) [14]	-	0.50
Channel	Rajagopalan (1980) [67]	-	0.62 - 0.96

As it can be seen, there is no generally accepted convective velocity. In addition, there is no acceptable physics for Taylor's hypothesis.

In another study in the literature, Alamo and Jimenez estimated the convection velocities of turbulence and tested Taylor's hypothesis [25]. They used the ensemble averages of local time derivatives to obtain convective velocities for channel flow. Also, they decided that the wall distance is correlated with eddy size or wavelength. As a result of comparing the present method with Taylor's hypothesis, they observed that both ways agree far from the wall where the convection velocity is close to the mean velocity. But they contradicted each other near the wall due to the significant difference between convection velocity and mean profile.

The turbulence intensity near the wall region at the high Reynolds numbers is considerable. This situation may be problematic for applying Taylor's hypothesis. But computation of these flow fields by DNS is significantly expensive [15]. Large Eddy Simulation (LES) can be used because it requires less computational effort, but it cannot solve near the wall region [60]. Thus, experimental measurements using hotwire are needed. However, using hotwire is also not easy to get spatial and temporal gradients simultaneously. Despite its inconveniences, Taylor's hypothesis is still used.

In recent years, with advancements in diagnostic technology, several experiments could be made to check Taylor's hypothesis or suggest an alternative method. Ganapathisubramani et al. made PIV (Particle Image Velocimetry) measurements on a turbulent round jet to obtain velocity gradient tensor for resolving small and intermediate scale eddies [34]. Then, they compared their results with Taylor's hypothesis, which showed a good agreement. Davoust and Jacquin defined an optimum convection velocity from continuity equation to use Taylor's hypothesis [23]. They made turbulent jet experiments, used the Fourier transform of continuity to obtain velocity gradients, and described optimum convection velocity as a function of frequency and radius. They observed that results are acceptable for low frequencies for the core and center of the mixing layer but not satisfying outside these regions and frequencies. Another study about DNS analysis of Taylor's hypothesis was done for turbulent channel flow at low Reynolds number by Tardu and Vezin [82]. They concluded that this hypothesis is not useful for the viscous sublayer and buffer layer. Other studies that discussed Taylor's hypothesis for turbulent channel flow at low Reynolds numbers by DNS, such as Zhang et al. [39], Zhao et al. [100], and Geng et al. [35], concluded that this hypothesis becomes inaccurate with closing to the wall. Today, there are still many studies in the literature that studied alternative convective velocity definitions for specific flow cases like Dróżdż et al., Baars et al. and Yang et al. [28], [5], [98].

This literature survey shows that there has been an intense interest to the application of the frozen turbulence hypothesis. In this thesis, no use of frozen turbulence hypothesis or its consequence such as Eqn. 1.6a are included or the only use of them in this thesis just for the sake of the comparison of QBT results vs frozen turbulence concept and consequences. All results shown in following pages are consequential to QBT approach and related mathematics.

1.3 Literature Review on Length Scales in Turbulence

The studies about turbulent flow problems in the literature are based on dimensional analysis and scaling laws. Therefore, identification of different length and time scales is essential for turbulent flow problems. As mentioned before, turbulent flow consists

of a wide range of eddies in terms of sizes, lifespans, and appearances. These eddies appear and disappear with respect to space and time in a random fashion. Large scale is considered in general with the integral scale, L [43]. Also, it has a critical role in the transportation of momentum and energy. Physically, the size of large eddies cannot exceed the boundaries of the flow [48].

Integral scale can be estimated in several different ways. For instance, it can be roughly related to the characteristic length of flow, such as the chord of the airfoil, the diameter of the pipe [48]. In the literature, several methods for the determination of integral length scale are based on correlation or spectrum function [88]. One of the standard ways is using the first zero crossing of the integrated autocorrelation function, as discussed in [56]. For active grid studies, reaching zero of this function is prohibited due to the energy content of eddies at low frequencies as in the study of Dogan et al. [27]. Another typical method for obtaining integral scale is finding the wavenumber corresponding to the peak of pre-multiplied energy spectra. Mydlarski et al. proposed a relation based on this approach to find an integral scale in active grid studies [57]. This relation requires rms of velocity fluctuations, u', and viscous dissipation rate, ϵ, to obtain integral scale. In another study published in 2014 as a NASA technical report for the procedure of finding length scales, El-Gabry et al. made hotwire experiments and analyzed the data by spectral approach as FFT [29]. They used the length scale formulations of macro and microscale eddies proposed for grid turbulence studies by Roach [76]. These scales can be obtained with the help of mean velocity, $\overline{U}$, rms of velocity fluctuations, u', and energy spectrum in the frequency domain, $E(f)$.

The size of the smallest eddies is determined by the Kolmogorov length scale, η_k. This scale represents scales at which the division of eddies is over, and their energy converts to heat due to viscous dissipation. According to Kolmogorov's 1^{st} similarity hypothesis, this scale depends on the dissipation rate, ϵ, and viscosity, ν. In the literature studies, the dissipation rate is generally found by spatial derivatives calculated from temporal derivatives based on Taylor's hypothesis, as in the study of Dogan et al. [27].

As defined before, another significant length scale widely mentioned in the literature

is the Taylor microscale, λ. That is used for estimating the fluctuation strain rate. This scale is calculated by kinematic viscosity, ν, rms of velocity fluctuations, u', and dissipation rate, ϵ, that is obtained by the spatial gradient found by Taylor's hypothesis [27], [85].

1.4 Motivation and Purpose of the Study

Thus far, the importance and example of calculations of length scales in turbulence are introduced. It is observed that Taylor's frozen turbulence hypothesis is frequently used under any condition. Yet, many studies have been conducted to test its accuracy and corrections to this hypothesis have been offered, e.g., [51], [52], [37], [42], [32], [99], [25], [24], [34].

The criticisms about this hypothesis can be compiled in three groups:

- It is not applicable for small intensity cases, as Taylor proposed himself [84]. If turbulence fluctuations are close to mean flow velocity, it creates an extreme error [98].
- Using the constant convective velocity for the entire flow field is a physically wrong approach to the turbulent flow problems [99]. In particular, a gross error is observed in the near the wall region for wall-bounded flows [25].
- For large-scale turbulent structures, this hypothesis does not satisfy the physics [24]. For instance, if the size of the large eddy at 1 Hz frequency for a flow with mean velocity, 10 m/s in 10 cm diameter pipe, is calculated by this hypothesis, it is found as 1.59 m. It is not possible physically [70].

There are also alternative methods to Taylor's hypothesis. However, these methods consist of semi-empirical formulations for specific flow cases under some circumstances.

This study focuses on an alternative method, i.e., Quantic Behavior of Turbulence, proposed by Çıray [69]. The differences of this approach from the methods used in the literature can be summarized as:

- QBT has a basis that seems to reflect the physics of the problem.
- The frequency-based spectrum is taken into consideration within the development of calculations.
- This approach has been used for physically acceptable cases such as grid turbulence, pipe flow, boundary layer, and flow around an airfoil [69].
- The eddy sizes, lifespans, and energy contributions of each frequency can be obtained by following the mathematical procedure of QBT.
- In this approach, the smallest turbulent frequency is taken 1 Hz as a nominal value. Our calculations in this work show that the intrinsic dimensions of the flow domain is not reached at 1 Hz. If the intrinsic dimension of the domain is taken as the largest eddy size, then a frequency less than 1 Hz can be obtained. In this work, no study has been performed to find out what the smallest frequency of turbulent is. One cycle per second or 1 Hz is taken as reference value just for the sake of comparison.

1.5 The Content of the Thesis

The content of this master's thesis consists of implementing the mentioned QBT to a Matlab code and applying the developed code to the different flows measured by hotwire. In Chapter 1, basic background information on turbulent flow problems is briefly mentioned; energy spectrum, energy cascade, and length scales are introduced. The importance of length scales in turbulent flow problems solved by modeling is explained, and case studies in the literature and studies on Taylor's hypothesis used in this solution are examined. As a result, the reasons for the need for QBT are also stated. In Chapter 2, how to obtain the frequency-dependent spectrum with the spectral approach and then how to get wavenumbers, so eddy sizes, by the mathematical procedure of QBT are discussed. The content of Chapter 3 is the explanation of the flow chart and subroutines of the implemented code. In Chapter 4, the experimental setups of the analyzed experiments are introduced. In the last two chapters (Chapters 5 and 6), results such as frequency-dependent spectrum, wavenumber-dependent

spectrum, eddy sizes, and lifespans of some of the turbulent flow data cases are shown. All findings are discussed in detail.

CHAPTER 2

THEORY

2.1 Introduction

In this section, the theoretical foundations of the study are emphasized, and the mathematical procedure used is explained. First, QBT, which is an approach that this study is based on, is concentrated. Then, it is shown how to obtain the frequency-dependent energy spectrum by spectral study. Following the mathematical procedure of QBT with obtained frequency-dependent energy spectrum, wavenumbers and other critical results are obtained, and each step is explained in detail.

2.2 Quantic Behaviour of Turbulence

Quantic Behavior of Turbulence (QBT) is introduced by Çıray [69] for the first time, and in that study, a new dispersion relation is defined as,

$$u = \frac{d\omega}{dk}, \tag{2.1}$$

where u is fluctuation velocity, ω is the circular frequency that is defined as ω=$2\pi f$ and k is the wavenumber. Physically, this definition determines that the turbulence energy is carried by "**discrete material packages of finite lifespan**" [70]. It means that these packages emit energy signals in the waveform, and these energy signals oscillate and change intermittently. In this way, the instantaneous fluctuation velocity becomes the energy transport velocity (group velocity) of the package (eddy).

An *eddy* can be defined as a group of fluid particles that move together and conserve the identity of the group for a while. Therefore, the motion of an eddy is the move-

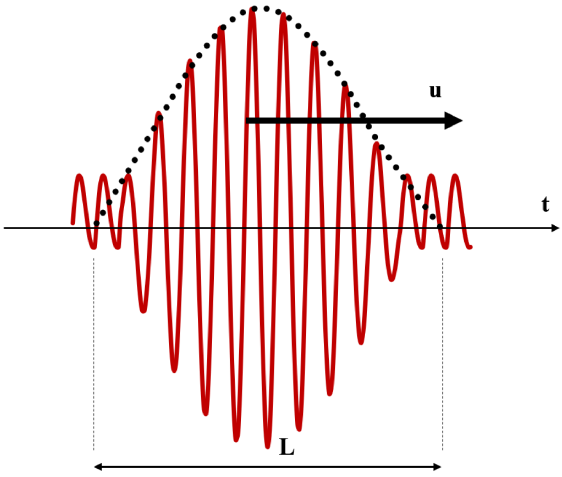

Figure 2.1: Representation of particle and wavy character of turbulence reproduced from Figure 5 in [72]

ment of fluid particles which behave as a group. On the other hand, this motion which borns and dies in time, t, is also the movement of the dispersive wave [72]. This definition is represented in Fig. 2.1 where L is the specific length of both the wave and the particle group (eddy). Consequently, the definition of the fluctuation velocity as the group velocity is based on these dual characteristics of turbulence. This approach forms the basis of QBT.

An essential aspect of this approach is that the own characteristics of turbulent flows are also taken into account in the calculation of wavenumbers. The characteristic information of the flow is provided by the frequency-dependent energy spectrum function, $G(f)$, which is the kinetic energy contribution of specified frequency interval out of one, and it is obtained from the spectral study. This function can be defined as,

$$u'^2 = \overline{u^2} = u'^2 \int_0^\infty G(f)df, \tag{2.2}$$

where u' is root-mean-square (rms) of instantaneous velocity fluctuations and f is frequency. Then, this relation can be written as,

$$\int_0^\infty G(f)df = 1. \tag{2.3}$$

This spectrum function, $G(f)$, carries the actual characteristics of the flow. Therefore, it is crucial to get realistic results for the physics of the flow by this method.

Another critical function used in QBT is the Probability Density Function (PDF) of the fluctuation velocities. The PDF and the frequency-dependent energy spectrum function are related as:

$$\int_{-\infty}^{\infty} P(x)u^2\,dx = u'^2 \int_{0}^{\infty} G(f)\,df, \tag{2.4}$$

where $P(x)$ represents the PDF, x is non-dimensional instantaneous fluctuation velocity. It can be shown how x is obtained as,

$$U = \overline{U} + u = \overline{U}\left(1 + \frac{u}{u'}\frac{u'}{\overline{U}}\right) = \overline{U}(1 + xI) = \overline{U}y, \tag{2.5}$$

where U is instantaneous velocity, y is non-dimensional instantaneous velocity, $\overline{U}$ is mean velocity and I is turbulence intensity. Also, x, y and I can be simply written as,

$$x = \frac{u}{u'}, \tag{2.6}$$

$$y = 1 + xI = \frac{U}{\overline{U}}, \tag{2.7}$$

$$I = \frac{u'}{\overline{U}}. \tag{2.8}$$

Eqn. 2.4 is represented in Fig. 2.2 and Fig. 2.3. The left-hand-side (LHS) of Eqn. 2.4 is shown in Fig. 2.2 where $P(x)$ curve shows the probability of the existence of each non-dimensional velocity x and $P(x)u^2$ represents the kinetic energy contribution of these velocities.

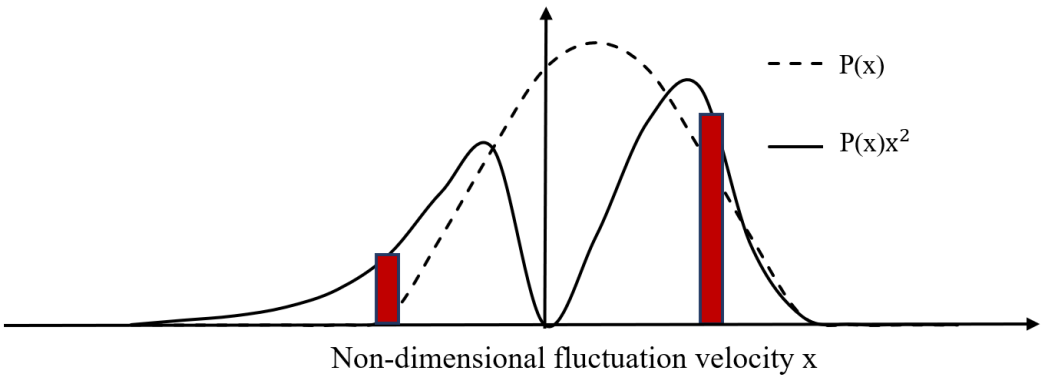

Figure 2.2: The representation of LHS of Eqn. 2.4 reproduced from LHS of Figure 6 in [72]

PDF is a chosen skewed function in the present study, and its details are explained later. Besides, due to its skewness, the positive and negative velocity intervals have

different probabilities. Nevertheless, these velocity intervals contribute to the kinetic energy of the same frequency interval together, as shown in Fig. 2.3.

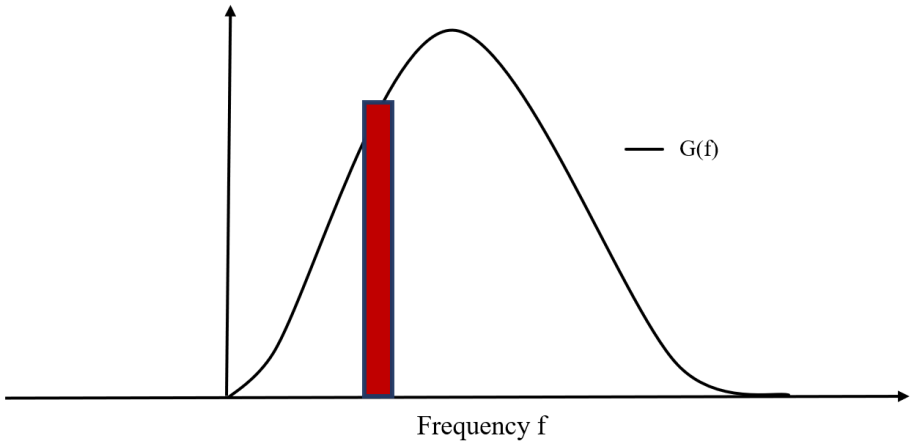

Figure 2.3: The representation of RHS of Eqn. 2.4 reproduced from RHS of Figure 6 in [72]

Therefore, the integral part at LHS of Eqn. 2.4 should be splitted,

$$\int_{-x_{i+1}}^{-x_i} P(x)u^2\,dx + \int_{x_i}^{x_{i+1}} P(x)u^2\,dx = u'^2 \int_{f_i}^{f_{i+1}} G(f)\,df. \tag{2.9}$$

In summary, two main equations need to be solved to calculate wavenumbers using the QBT approach. First of all, using Eqn. 2.4, the relationship between fluctuation velocities and frequency must be obtained; that is, $u(f)$ must be found. Then, using Eqn. 2.1, the wavenumbers should be calculated.

2.3 The Mathematical Procedure of the Study

As mentioned in the previous section, the basis of QBT consists of solving two main equations (Eqns. 2.4 and 2.1). However, before solving these two equations, it is necessary to find the energy spectrum in frequency domain, which has an important contribution to this theory. First of all, two methods for finding this spectrum are discussed in this section. These are Discrete Fourier Transform (DFT) and Fast Fourier Transform (FFT). Next, it is explained how the spectrum can be derived from DFT or FFT results which are the Fourier coefficients.

Once the frequency-dependent energy spectrum is obtained, the mathematical procedure of QBT is passed. With this calculation method, first, the fluctuation velocities depending on the frequency are found. Then, the calculation steps of wavenumbers are shown.

2.3.1 Spectral Study

In this part of the chapter, the spectral approach in turbulent flows are discussed. With this approach, kinetic energy contributions for each frequency are obtained, and thus, the energy spectrum can be plotted in terms of frequency.

As the first step of this approach, it is assumed that the instantaneous velocity fluctuations of turbulence are formed by overlapping an infinite number of sinusoidal waves. This definition is expressed mathematically for homogeneous turbulence with the Fourier integral as shown below [43]. Here, $u(t)$ is assumed as the instantaneous fluctuation velocity in the x-direction,

$$u(t) = 2\pi \int_0^\infty [a(\eta)cos(2\pi\eta t) + b(\eta)sin(2\pi\eta t)]\, d\eta \ , \tag{2.10}$$

where η is the frequency, t is time and Fourier coefficients are

$$a(\eta) = \frac{1}{\pi} \int_{-\infty}^{\infty} u(t)cos(2\pi\eta t)\, dt \ , \tag{2.11a}$$

$$b(\eta) = \frac{1}{\pi} \int_{-\infty}^{\infty} u(t)sin(2\pi\eta t)\, dt \ . \tag{2.11b}$$

But, these equations are valid for the condition,

$$\int_{-\infty}^{\infty} |u(t)|\ dt = finite \ . \tag{2.12}$$

Considering the nature of turbulence, this condition is not possible since instantaneous velocity fluctuations are different from zero. To solve this problem, the boundaries of the integral are limited as $-T$ and $+T$ where T is period. Apart from this time, instantaneous fluctuation velocities are assumed to be zero, and this is a physically correct assumption. Thus, it is ensured that the integral is finite. These expres-

sions with assuming $u(t) = 0$ when $t > T$ and $t < -T$ are as follows,

$$a(\eta) = \frac{1}{\pi} \int_{-T}^{T} u(t) cos(2\pi\eta t)\, dt \ , \tag{2.13a}$$

$$b(\eta) = \frac{1}{\pi} \int_{-T}^{T} u(t) sin(2\pi\eta t)\, dt \ . \tag{2.13b}$$

In the next section, two methods for finding these coefficients with Fourier transform are examined. After that, obtaining the energy spectrum in terms of frequency from these coefficients are discussed.

2.3.1.1 Fourier Transforms

The purpose of the Fourier transform is to transfer the signal measured in the time domain to the frequency domain. As mentioned in the previous section, this transform is the expression of the signal with the Fourier series, that is, finding the Fourier coefficients. If the signal is periodic and discrete, the Fourier integral in Eqn. 2.10 does not need to be written in continuous form. This signal can be written in a discrete form which is the Discrete Fourier Transform (DFT) representation. In this study, discretely sampled data is interested, and thus, there is no requirement for the continuous form and solution for it.

In the analysis of a signal by Fourier Transform, one of the most important parameters is the frequency limit which is decided by the Sampling Theorem. Let sampling interval be Δ and f_c be a special frequency that is also called Nyquist critical frequency [65], the relation of these two is,

$$f_c = \frac{1}{2\Delta} \ . \tag{2.14}$$

For instance, for experimental data measured at 10 kHz as a sampling rate, the sampling interval is 10^{-4} s. Therefore, Nyquist critical frequency is found as 5 kHz. Another important parameter of the discrete data u_t is the sampling rate that is the number of samples measured per second. Knowing this parameter allows finding the time interval Δ between two samples recorded as one divided by the sampling rate [65].

Additionally, Eqn. 2.14 is defined for a continuous function. However, if there are enough samples to represent a continuous equation, this relation can be applied to

discrete sample data represented by u_t. Before that, it should be checked whether the Fourier Transform approaches zero at the negative and positive frequency limits. If it is not, the frequency limit should be expanded.

In this study, the Fourier coefficients are needed to be found, and DFT is first used to obtain these coefficients. Due to the long measurement times and the high sampling rate, the number of instantaneous velocities measured by the experiment, namely the number of samples, N, is very high. However, DFT requires operations in the order of $O(N^2)$ to calculate the Fourier coefficients of N numbers of samples. It means that a substantial computational effort is required for high N numbers. Therefore, algorithms that reduce the number of operations are needed, and one of these algorithms, Fast Fourier Transform, is chosen.

Fast Fourier Transform is an efficient algorithm introduced by Cooley and Tukey in 1965 and provides computing the DFT [19]. Instead of NxN arithmetic operations, it can compute DFT with $Nx \log_2 N$ operations. This simplification makes the FFT one of the widely used methods for calculating Fourier Transform [41].

Using FFT, an equation in the physical time domain is transformed into a different representation of the same equation in the mathematical frequency domain. Although, in reality, there is no possibility of existing negative frequency physically, the negative frequencies exist in the frequency domain mathematically. Their energy contributions are transferred to the positive frequencies corresponding to them. In this way, a one-sided energy spectrum is obtained.

Table 2.1: Comparison of CPU for DFT and FFT [65]

# of Samples	CPU of FFT	CPU of DFT
10^6	30 seconds	2 weeks

This operation difference may be understood by comparing the CPU time of the application of two methods. Press et al. give an example for 10^6 samples and roughly estimate the CPU time as 30 seconds for FFT and 2 weeks for DFT on a microsecond cycle time computer as can be seen from Table 2.1. Therefore, FFT is chosen to find

Fourier coefficients in the present study.

As it can be understood from what has been explained so far, the DFT includes many repetitive terms in the calculations. In the FFT, unnecessary process repetition is prevented by realizing these terms, and the DFT is solved more efficiently. As a result of this transform, Fourier coefficients can be obtained.

Consequently, in this study, Fourier coefficients are found by FFT, and the "fft" command in Matlab is used for this process. The calculation procedure for DFT and FFT is added to the thesis as Appendix A.1 and A.2.

2.3.1.2 The Derivation of the Energy Spectrum in Frequency Domain

Until this part, how to obtain Fourier coefficients by Fourier Transform has been explained. Now, it is explained how to find the frequency-dependent energy spectrum from these coefficients. Thus, the contribution of frequency ranges to kinetic energy is found and used to obtain wavenumbers.

Assume that u is the x-component of the fluctuation velocity at a fixed point in the flow field, which is statistically homogeneous with respect to time. In this case, the mean value of the square of this velocity component can be considered as the sum of the energy contributions at all frequencies [43].This definition can be mathematically expressed as:

$$\int_0^\infty E(\eta)d\eta = \overline{u^2} \ , \tag{2.15}$$

where η is frequency and $E(\eta)d\eta$ is the kinetic energy contribution of the frequencies between η and $\eta + d\eta$. This is Taylor's 1-D spectrum as shown in Fig. 2.4 [16].

The largest eddies create velocity fluctuations of low frequencies, while the smallest eddies create velocity fluctuations of high frequencies. When there is a frequency range in the spectrum where the energy density $E(\eta)$ is high, the kinetic energy contribution of both ends of the spectrum is low. For very low frequencies, the energy is caused by the change of mean flow with respect to time. For very high frequencies, the noise generated by the measurement system is the cause of energy production. Therefore, lowpass and highpass filters are used. These regions, which are fewer fre-

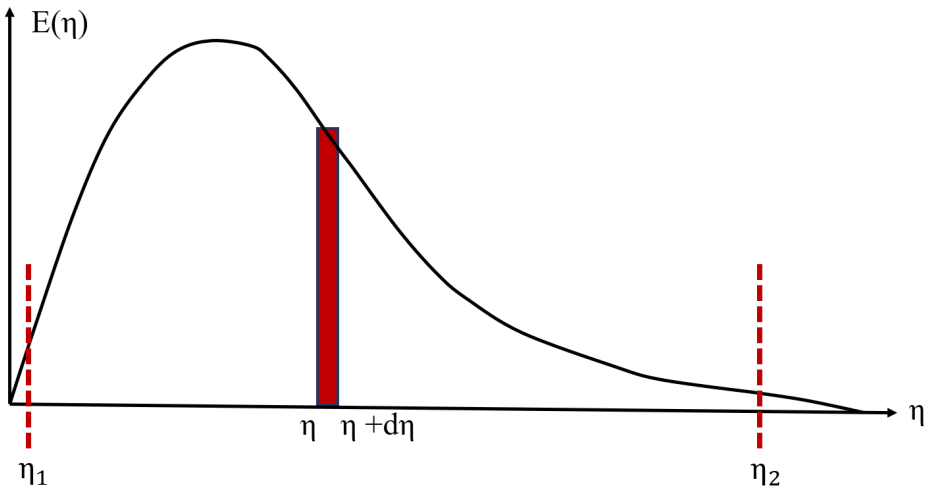

Figure 2.4: Taylor's 1-D energy spectrum reproduced from Figure XII. 12 in [16]

quencies than the η_1 and higher frequencies than the η_2, are not taken into account and considered unmeaningful [16].

At this point, the required step is to express the energy spectrum function in terms of Fourier coefficients. For this, the correlation function can be used because instantaneous fluctuation velocities are expressed in Fourier coefficients. Since the correlation function also consists of the fluctuation velocities, this function can be expressed in Fourier coefficients. G. I. Taylor is the first person to establish a relationship between these two functions and express them mathematically. However, in this study, Hinze's work, which is different from Taylor's, is used [43].

The correlation function, which measures the association of velocities in time at a fixed point in space, is expressed as follows at the end of long derivation steps in Hinze's book [43]:

$$Q_E(t) = \frac{4\pi^2}{2T+t}\int_0^\infty \frac{a^2(\eta)+b^2(\eta)}{2} cos(2\pi\eta t)d\eta \ , \tag{2.16}$$

where Q_E is the correlation function [16]. Then, $t = 0$ is chosen and Eqn. 2.16 becomes,

$$\overline{u^2(0)} = \pi^2 \int_0^\infty \frac{a^2(\eta)+b^2(\eta)}{T} d\eta \ . \tag{2.17}$$

The LHS of the Eqn. 2.17 shows the kinetic energy contribution of the fluctuation velocity in x-direction. Therefore, $\overline{u^2(0)} = \overline{u^2}$ can be written and Eqn. 2.17 becomes:

$$\overline{u^2} = \pi^2 \int_0^\infty \frac{a^2(\eta) + b^2(\eta)}{T} d\eta = \int_0^\infty E(\eta) d\eta \ . \tag{2.18}$$

As a result, the frequency-dependent spectrum from the Fourier coefficients is found in this way. Thus, it is possible to start calculating the wavenumbers by using the mathematical procedure of QBT.

2.3.2 The Energy Spectrum in Wavenumber through QBT

In this section, the details of the mathematical procedure of QBT are introduced. The first main equation is the dispersion relation that relates the wavenumber and frequency as given in Eqn. 2.1. The second main equation is used for the previous step of the 2.1. To find the corresponding wavenumber, each fluctuation velocity and frequency are required. The frequencies are obtained by the spectral analysis, and corresponding fluctuation velocities can be found by the relation in Eqn. 2.4. In the calculation of wavenumber, the characteristic information of the flow is required, and this information is obtained by the spectral characteristics of the spectrum in equation 2.4.

2.3.2.1 Basic Definitions and Properties of PDF

In this section, some properties of PDF are introduced. Then, these properties are used in the following steps [72],

$$\int_{-\infty}^{\infty} P(y)\, dy = 1 \ , \tag{2.19a}$$

$$\int_{-\infty}^{\infty} P(x)\, dx = \frac{1}{I} \ , \tag{2.19b}$$

$$\int_{-\infty}^{\infty} P(y) U\, dy = \overline{U} \ , \tag{2.19c}$$

$$\int_{-\infty}^{\infty} P(y) y\, dy = 1 \ . \tag{2.19d}$$

One of the critical parameters of the PDF is the moment, and its mathematical definition is as follows:

$$\mu^\kappa = \frac{1}{\overline{U}^\kappa} \int_{-\infty}^{\infty} P(y) U^\kappa dy \ . \tag{2.20}$$

In this definition, μ^κ is the moment of degree κ of U. The first-order moment of U in

Eqn. 2.19c can be obtained by Eqn. 2.20:

$$\int_{-\infty}^{\infty} P(y)U\,dy = \int_{-\infty}^{\infty} P(y)(\overline{U}+u)\,dy = \overline{U}\int_{-\infty}^{\infty} P(y)\,dy + \int_{-\infty}^{\infty} P(y)u\,dy = \overline{U}\ .$$

This moment is equal to the average value, and also called as the expectation value in statistics [90]. By using Eqn. 2.19c, a new property of PDF can be obtained as:

$$\overline{U} + \int_{-\infty}^{\infty} P(y)u\,dy = \overline{U} \quad \rightarrow \quad \int_{-\infty}^{\infty} P(y)u\,dy = 0\ . \tag{2.21}$$

The quadratic moment of U is the variance. In another saying, it is a measure of how much the data deviates from the mean value and how diverse it is. This moment is also manipulated with the properties of the PDF:

$$\int_{-\infty}^{\infty} P(y)U^2\,dy = \int_{-\infty}^{\infty} P(y)(\overline{U}+u)^2\,dy = \overline{U}^2\int_{-\infty}^{\infty} P(y)\,dy + \int_{-\infty}^{\infty} P(y)u^2\,dy = \overline{U}^2 + u'^2,$$

As a result, the quadratic moment is obtained in terms of turbulence intensity as follows:

$$\mu^2 = 1 + I^2\ . \tag{2.22}$$

2.3.2.2 The Implementation of Properties of PDF

In this section, PDF is defined, and the parameters required for this function are introduced.

PDF is the function showing the distribution of instantly measured fluctuation velocities. The fact that this function expresses the experimental data realistically is important in getting accurate results from QBT. For this purpose, an extended form of Maxwell's PDF is adapted by Çıray [69]. This modified equation is as follows:

$$P(y) = P(1)y^n exp\left[A^n\left(1-y^n\right)\right]\ . \tag{2.23}$$

Also, it is adapted for $y > 0$. In this equation, A and $P(1)$, which are unique to each data case, are constants that depend on parameter n. This parameter n is also a constant for each case and obtained by the relation between turbulence intensity and quadratic moment given in Eqn. 2.22. Therefore, Eqn. 2.23 can be expressed again as a function of y with constant values as:

$$P(y) = Cy^n exp\left(-A^n y^n\right) = C\varphi(y)\ , \tag{2.24}$$

where

$$C = P(1)exp(A^n)\ , \qquad (2.25a) \qquad \varphi(y) = y^n exp\left(-A^n y^n\right)\ . \qquad (2.25b)$$

The derivations of all these parameters, which PDF depends on, are displayed sequentially.

2.3.2.3 Determination of *P(1)*

How to obtain the constant $P(1)$ in the PDF equation is explained in this part. At first, using the condition 2.19a, constant C can be written as:

$$C = \frac{1}{\int_{-\infty}^{\infty}\varphi(y)\,dy}\ . \qquad (2.26)$$

If this transformation, $y^n = q$, is applied and the derivative of both sides of the equation is:

$$dy = \frac{1}{n}\frac{q^{\frac{1}{n}}}{q}dq\ . \qquad (2.27)$$

Then, φ(y) function is implemented by this transformation,

$$\int_{-\infty}^{\infty}\varphi(y)\,dy = \int_{-\infty}^{\infty} y^n exp\left(-A^n y^n\right)\ dy = \int_{-\infty}^{\infty} qexp\left(-A^n q\right)\ \frac{1}{n}\frac{q^{\frac{1}{n}}}{q}dq\ .$$

Finally, it becomes:

$$\int_{-\infty}^{\infty}\varphi(y)\,dy = \frac{1}{n}\int_{-\infty}^{\infty} q^{\frac{1}{n}} exp\left(-A^n q\right)\ dq\ . \qquad (2.28)$$

In the QBT approach, the similarity of this equation with the Gamma function in Abramowitz's book [2] is noticed [69]. As a result of this, the parameters in Eqn. 2.28 are associated with the variables in the Gamma function [72],

$$\Gamma(z) = k^z \int_0^{\infty} t^{z-1} exp\left(-kt\right)\ dt\ . \qquad (2.29)$$

The lower limits of the integrals of Eqn. 2.28 ve 2.29 are not the same. But PDF is defined for $y \geq 0$. Therefore, Eqn. 2.28 can be written as:

$$\int_{-\infty}^{\infty}\varphi(y)\,dy = \int_0^{\infty}\varphi(y)\,dy\ . \qquad (2.30)$$

The table below shows which parameters in the Gamma function correspond to the variables in Eqn. 2.28.

Table 2.2: Transformation to find $P(1)$

Eqn. 2.29		Eqn. 2.28
t	$\rightarrow$	q
k	$\rightarrow$	A^n
$z-1$	$\rightarrow$	$\frac{1}{n}$
z	$\rightarrow$	$\frac{n+1}{n}$

At the end of this transformation, Eqn. 2.28 is expressed in terms of the gamma function,

$$\int_{-\infty}^{\infty} \varphi(y)\, dy = \frac{1}{n} A^{-(n+1)} \Gamma\left(\frac{n+1}{n}\right) \ . \tag{2.31}$$

Finally, C and $P(1)$ are obtained by combining Eqn. 2.26 and Eqn. 2.25a:

$$C = \frac{nA^{n+1}}{\Gamma\left(\frac{n+1}{n}\right)} \ , \tag{2.32}$$

$$P(1) = \frac{nA^{n+1}}{\Gamma\left(\frac{n+1}{n}\right) exp(A^n)} \ . \tag{2.33}$$

By substituting C and $P(1)$ in the PDF, it can be written as:

$$P(y) = \frac{nA^{n+1}}{\Gamma\left(\frac{n+1}{n}\right)} y^n exp(-A^n y^n) \ . \tag{2.34}$$

Additionally, PDF can be expressed as a function of x:

$$P(x) = I \frac{nA^{n+1}}{\Gamma\left(\frac{n+1}{n}\right)} (1+xI)^n exp\left[-A^n (1+xI)^n\right] \ , \tag{2.35}$$

where $y = 1 + Ix \ ,$ $IP(y) = P(x) \ .$

2.3.2.4 Determination of *A*

Constant A can be obtained by substituting Eqn. 2.24 into condition in Eqn. 2.19d:

$$C \int_{-\infty}^{\infty} \varphi(y) y\, dy = C \int_{-\infty}^{\infty} y^{n+1} exp\left(-A^n y^n\right)\, dy = 1 \ . \tag{2.36}$$

Then, the same transformation, which is $y^n = q$, is applied as shown in Table 2.3,

$$C\int_{-\infty}^{\infty} q^{\frac{n+1}{n}} exp\left(-A^n q\right) \frac{1}{n}\frac{q^{\frac{1}{n}}}{q}\, dq = \frac{C}{n}\int_{-\infty}^{\infty} q^{\frac{2}{n}} exp\left(-A^n q\right)\, dq = 1\ . \tag{2.37}$$

Table 2.3: Transformation to find A

Eqn. 2.29		Eqn. 2.37
t	$\rightarrow$	q
k	$\rightarrow$	A^n
$z-1$	$\rightarrow$	$\frac{2}{n}$
z	$\rightarrow$	$\frac{n+2}{n}$

By substituting C constant found in Eqn. 2.32, Eqn. 2.37 becomes as follows,

$$C\frac{1}{n}\Gamma\left(\frac{n+2}{n}\right)\frac{1}{A^{n+2}} = \frac{nA^{n+1}}{\Gamma\left(\frac{n+1}{n}\right)}\frac{1}{n}\Gamma\left(\frac{n+2}{n}\right)\frac{1}{A^{n+2}} = 1\ . \tag{2.38}$$

Finally, A can be defined in terms of the Gamma function,

$$A = \frac{\Gamma\left(\frac{n+2}{n}\right)}{\Gamma\left(\frac{n+1}{n}\right)}\ . \tag{2.39}$$

2.3.2.5 Determination of μ^κ

PDF in Eqn. 2.24 is used in the moment definition given in Eqn. 2.20,

$$\mu^\kappa = \frac{1}{\overline{U}^\kappa}\int_{-\infty}^{\infty} P(y)U^\kappa\, dy = \int_{-\infty}^{\infty} P(y)y^\kappa\, dy = C\int_{-\infty}^{\infty} y^n exp\left(-A^n y^n\right) y^\kappa\, dy\ .$$

Again, transforming $y^n = q$ and other parameters as shown in Table Eqn. 2.4, it becomes:

$$\mu^\kappa = C\int_{-\infty}^{\infty} y^{n+\kappa} exp\left(-A^n y^n\right)\, dy = \frac{C}{n}\int_{-\infty}^{\infty} q^{\frac{1+\kappa}{n}} exp\left(-A^n q\right)\, dq\ . \tag{2.40}$$

Table 2.4: Transformation to find the moments

Eqn. 2.29		Eqn. 2.40
t	$\rightarrow$	q
k	$\rightarrow$	A^n
$z-1$	$\rightarrow$	$\frac{1+\kappa}{n}$
z	$\rightarrow$	$\frac{n+\kappa+1}{n}$

Writing the equation in terms of the Gamma function, the moment from the degree κ can be written as:

$$\mu^{\kappa} = \frac{C}{n} A^{-(n+\kappa+1)} \Gamma\left(\frac{n+\kappa+1}{n}\right) . \tag{2.41}$$

Inserting A and C into this equation, μ^{κ} is obtained as only depending on n,

$$\mu^{\kappa} = \frac{\left[\Gamma\left(\frac{n+1}{n}\right)\right]^{\kappa-1} \Gamma\left(\frac{n+\kappa+1}{n}\right)}{\left[\Gamma\left(\frac{n+2}{n}\right)\right]^{\kappa}} . \tag{2.42}$$

In addition to all this, the second-order moment allows finding the number n. In this case, the relation of this moment with turbulence intensity in Eqn. 2.22 as shown below should be remembered,

$$\mu^2 = 1 + I^2 = \frac{\Gamma\left(\frac{n+1}{n}\right) \Gamma\left(\frac{n+3}{n}\right)}{\left[\Gamma\left(\frac{n+2}{n}\right)\right]^2} . \tag{2.43}$$

Since the turbulence intensity is known by experimental data, the value of the second-order moment is found. After that, Eqn. 2.42 is written for $\kappa = 2$, and the number n that satisfies this moment value is obtained.

2.3.2.6 Discrete Form of Working Equations

Until here, it is shown how to obtain the PDF and the parameters it depends on. It is also described how to find the energy spectrum function depending on the frequency from the spectral study. Now, the calculation procedure from the governing equations of QBT is explained.

First of all, the relation between frequency and fluctuation velocities is found by the first main equation of QBT as shown below,

$$\int_{-\infty}^{\infty} P(x)u^2\,dy = u^{'2}\int_0^{\infty} G(f)\,df. \tag{2.44}$$

Dividing the equation by u'^2 and remembering the relation $x = u/u'$, it becomes,

$$\int_{-\infty}^{\infty} P(x)x^2\,dx = \int_0^{\infty} G(f)\,df\ . \tag{2.45}$$

As mentioned before, the probability of positive and negative velocities occurring in flow is different. Therefore, the PDF is chosen to be skewed to suit the physics of the situation. Therefore, LHS in Eqn. 2.45 should be written as:

$$\int_{-x_{i+1}}^{-x_i} P_L(\xi)\xi^2\,d\xi + \int_{x_i}^{x_{i+1}} P_R(\xi)\xi^2\,d\xi = \int_{f_i}^{f_{i+1}} G(\eta)\,d\eta\ . \tag{2.46}$$

This representation shows the kinetic energy contribution to the specific frequency band, which is between f_i and f_{i+1}. This contribution is transferred from the positive and negative state of the same velocity interval to the same frequency range as a contribution. Discrete form of this equation is as follows:

$$\left[P_L(-x_{i+1})(-x_{i+1})^2 + P_L(-x_i)(-x_i)^2\right]\frac{-x_{i+1}-(-x_i)}{2} + \left[P_R(x_{i+1})(x_{i+1})^2 + P_R(x_i)(x_i)^2\right]\frac{x_{i+1}-x_i}{2} = \Delta G(f_i; f_{i+1})\ . \tag{2.47}$$

After that, $P_R(x_{i+1})$ and $P_L(-x_{i+1})$ are expanded by the first-order Taylor Series expansion,

$$x_{i+1} = x_i + \Delta x_{i+1} \quad \rightarrow \quad P_R(x_{i+1}) = P_R(x_i) + \frac{dP_R(x_i)}{dx}\Delta x_{i+1}\ , \tag{2.48}$$

$$-x_{i+1} = -x_i - \Delta x_{i+1} \quad \rightarrow \quad P_L(-x_{i+1}) = P_L(-x_i) - \frac{dP_L(-x_i)}{dx}\Delta x_{i+1}\ . \tag{2.49}$$

Substituting the expanded forms of $P_R(x_{i+1})$ and $P_L(-x_{i+1})$ into Eqn. 2.47, the obtained equation is:

$$\left\{\left[P_L(-x_i) - \frac{dP_L(-x_i)}{dx}\Delta x_{i+1}\right](-x_i - \Delta x_{i+1})^2 + P_L(-x_i)(-x_i)^2\right\}\frac{\Delta x_{i+1}}{2} + \left\{\left[P_R(x_i) + \frac{dP_R(x_i)}{dx}\Delta x_{i+1}\right](x_i + \Delta x_{i+1})^2 + P_R(x_i)(x_i)^2\right\}\frac{\Delta x_{i+1}}{2} = \Delta G(f_i; f_{i+1}). \tag{2.50}$$

When the higher-order terms than the second degree are neglected, a quadratic equation is found as:

$$C_1 \Delta x_{i+1}^2 + C_2 \Delta x_{i+1} = \Delta G(f_i; f_{i+1}) \ , \tag{2.51}$$

where

$$C_1 = x_i \left[P_L(-x_i) + P_R(x_i) \right] + \frac{1}{2} x_i^2 \left[\left. \frac{dP_L}{dx} \right|_{-x_i} + \left. \frac{dP_R}{dx} \right|_{x_i} \right] \ , \tag{2.52}$$

$$C_2 = x_i^2 \left[P_L(-x_i) + P_R(x_i) \right] \ . \tag{2.53}$$

In other words, C_1 and C_2 values depending on the PDF itself and its derivatives, are obtained in each calculation step. Afterward, Δx value, which is the root of the second-order equation, is found, and the frequency-dependent x value is obtained.

Finally, the only thing required to find frequency-dependent nondimensional fluctuation velocities x is to start these calculations, i.e., their initial conditions. After explaining how the calculations started, all the steps of finding these velocities are explained. Then, the calculation of wavenumbers from these velocities is mentioned.

2.3.2.7 Initiation of Calculation of Working Equations

The initial conditions are:

$$x_0 = 0 \rightarrow P_L(x = 0) = P_R(x = 0) = P(y = 1) \ .$$

To find x_1, Eqn. 2.46 is written as:

$$\int_0^{x_1} 2P(1)x^2 \, dx = \Delta G(0; 1) \ , \tag{2.54}$$

where ΔG and $P(1)$ are constant. It can also be represented like,

$$x_1 = \left(\frac{3}{2} \frac{\Delta G(0; 1)}{P(1)} \right)^{\frac{1}{3}} \ . \tag{2.55}$$

The results are in a form:

$$x = x(f) \ .$$

All x values are obtained by starting the equation with these initial conditions mentioned and following the steps in the previous title. Now, the step of finding wavenumbers can proceed. To find k_1, the first main equation of QBT is used,

$$u = \frac{d\omega}{dk} \, .$$

The circular frequency can be written in terms of frequency such as $\omega = 2\pi f$ and the definition of nondimensional fluctuation velocity $x = u/u'$ is recalled. The integration of dispersion relation becomes:

$$k = \int_0^{\omega} \frac{d\omega}{u} = \frac{2\pi}{u'} \int_0^{f} \frac{df}{x} \, . \tag{2.56}$$

In ΔG calculation, the first frequency interval is taken between 0 and 1 Hz. Therefore, the first wavenumber can be splitted from the integral as shown below,

$$k(f) = \frac{2\pi}{u'} \left(\int_0^{1} \frac{df}{x} + \int_1^{f} \frac{df}{x} \right) = k(1) + \frac{2\pi}{u'} \int_1^{f} \frac{df}{x} \, . \tag{2.57}$$

To find $k(1)$, it can be written as,

$$x = x_b \left(\frac{f}{f_b} \right)^B \, , \tag{2.58}$$

where B, x_b and f_b are defined by the first three combinations of x and f. Thus, using the equation below, $k(1)$ is calculated,

$$k(1) = \frac{2\pi}{u'} \frac{f_b^B}{x_b} \int_0^{f_1} \frac{df}{f^B} = \frac{2\pi}{u'} \left(\frac{f_b}{f_1} \right)^B \frac{f_1}{1-B} \, . \tag{2.59}$$

Finally, by substituting $k(1)$ in Eqn. 2.57, the final form of the equation to be used to find the wavenumber is obtained,

$$k(f_i) = \frac{2\pi}{u'} \left(\frac{f_b}{f_1} \right)^B \frac{f_1}{1-B} + \frac{4\pi}{u'} \sum_{j=2}^{i} \frac{f_j - f_{j-1}}{x_j + x_{j-1}} \, . \tag{2.60}$$

This equation can be expressed in a simpler representation,

$$k(f_i) = \frac{2\pi}{u'} \left[\left(\frac{f_b}{f_1} \right)^B \frac{f_1}{1-B} + 2 \sum_{j=2}^{i} \frac{f_j - f_{j-1}}{x_j + x_{j-1}} \right] \, . \tag{2.61}$$

The wavelength, L, and the phase velocity, c, can be calculated as,

$$L = \frac{1}{k} \,, \tag{2.62}$$

$$c = \frac{\omega}{k} \,. \tag{2.63}$$

In addition, the lifespan of eddies, t_L, can be obtained by using:

$$t_L = \frac{L}{u} = \frac{L}{xu'} \,. \tag{2.64}$$

CHAPTER 3

THE DEVELOPED COMPUTER CODE

3.1 Introduction

In this section, the code which is the implementation of QBT is described. The code is written in Matlab. Firstly, the algorithm of the code is explained and shown by the flow chart. Then, inputs and subroutines are mentioned. The parameters which the defined functions need as the input and gives as the outputs are clarified. After that, the code outcomes are provided, and finally, it is explained how the calculation procedure of the code is verified.

3.2 Flow Chart

The code implemented in this study first obtains the spectrum in frequency domain by spectral analysis from the instantaneous velocities measured by the experiment. Then, it obtains the wavenumbers of the frequency ranges determined by the QBT approach. By using wavenumbers, wavelengths, so eddy sizes, and phase velocities are calculated.

The flow chart briefly shows the algorithm of the prepared code in Fig. 3.1. Firstly, the instantaneous velocities measured by the experiments, U, the sampling rate, SR, and duration of the experiment, T, are defined as the inputs. The code estimates the instantaneous fluctuation velocities, u, rms of the fluctuations, u', mean velocity, U_m, turbulence intensity, I_{act}, and 2^{nd} order moment, μ^2_{act}.

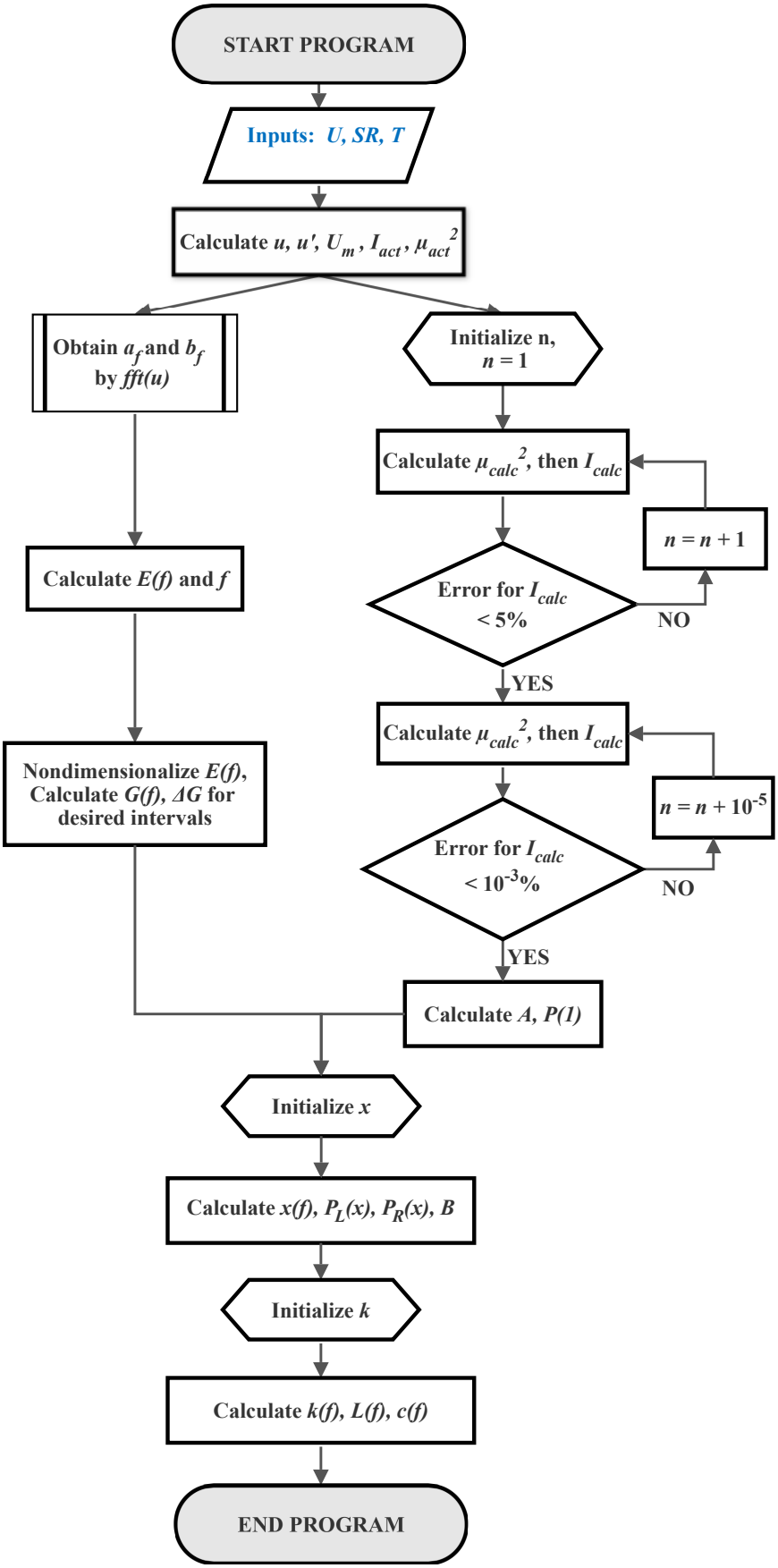

Figure 3.1: Flow chart of the code

As the next step, the fluctuation velocities are represented as the sum of the sine and cosine functions. The coefficients of sine and cosine functions, that is, Fourier coefficients, a_f and b_f where f represents each frequency, are calculated by the "fft" command of Matlab. These coefficients provide the frequency-dependent energy spectrum, $E(f)$. The non-dimensional form of this spectrum function is represented by $G(f)$, which can be found by dividing the square of rms of fluctuation velocities, u'. Also, by finding the area under the $G(f)$ curve, the kinetic energy contribution of each frequency interval out of one, ΔG, is obtained.

With the knowledge of the kinetic energy contribution of the frequency intervals, ΔG, rms of the fluctuations, u', turbulence intensity, I_{act}, and 2^{nd} order moment, μ^2_{act}, QBT can be applied to the test case. First of all, the number n should be determined to specify PDF. In the process of finding this number, turbulence intensity, I_{act}, or 2^{nd} order moment, μ^2_{act} is used. By defining tolerance limits in two steps to reduce the number of operations and make the code efficient, the number n, which satisfies the I_{calc} accurately, is estimated. After that, other properties of PDF like A, $P(1)$ are calculated.

Until this point, frequency-dependent energy spectrum is found by the spectral study, and PDF is specified by using turbulence intensity, I_{act}. Therefore, Eqn. 2.45 can be solved for $x(f)$. The solving process is started with Eqn. 2.55. The positive root of the quadratic equation, Δx_{i+1} in Eqn. 2.51 is calculated and the next x and corresponding $P_L(x)$ and $P_R(x)$ are found. After that, the parameter B is calculated using the first three combinations of x and f. It means that all values of these parameters are obtained. Thus, it is passed to the next step, that is, the estimation of the wavenumbers. Eqn. 2.59 is used for the initialization of wavenumber calculation. Then, other wavenumbers can be estimated by Eqn. 2.57. Finally, Eqn. 2.62 and 2.63 are used for calculating wavelength, L and phase velocity, c.

3.3 The Details of the Code

In this section, the detail of the code is given. Primarily, the inputs of the code are introduced. Then, subroutines are explained, such as functions, inputs, and outputs.

After that, the desired results of the code are shown, and finally, it is explained how the code is validated.

3.3.1 Inputs of the Code

The code is shown in Fig. 3.1 in a general form. But according to inputs, the running parts of the code can be different. For instance, the instantaneous velocities, U, or instantaneous fluctuation velocities, u, measured by the experiment can be defined as the first input type. For this type, other required parameters are the sampling rate, SR, and period, T. Another type is the non-dimensional frequency-dependent energy spectrum, $G(f)$ as an input. Some measurement systems can also obtain this spectrum. If this spectrum is used as the input, the part of the code consisting of the QBT procedure is used without the need for the spectral study. In addition, the turbulence intensity, I_{act}, and rms of the fluctuation velocities, u', are necessary to define for the calculations.

Moreover, the code can be improved by adding the voltage transformation part to the instantaneous velocity as the first step of the code. Therefore, measured voltage can be input, and except for finding the instantaneous velocities, the entire procedure of the calculations of the code remains the same.

3.3.2 Subroutines

In this part of the chapter, subroutines are clarified. After calling the inputs and calculating the instantaneous fluctuation velocities, u, rms of the fluctuations, u', mean velocity, U_m, turbulence intensity, I_{act}, and 2^{nd} order moment, μ_{act}^2, the code continues with the spectral study.

3.3.2.1 Subroutine *dftfunction.m* and *fftfunction.m*

This function finds the Fourier coefficients, a_f, and b_f and only requires the instantaneous fluctuation velocities as the input. In the previous chapters, two methods for

obtaining these coefficients are mentioned that are DFT and FFT. In this study, FFT is decided for use. Here, the reason for this decision is explained first.

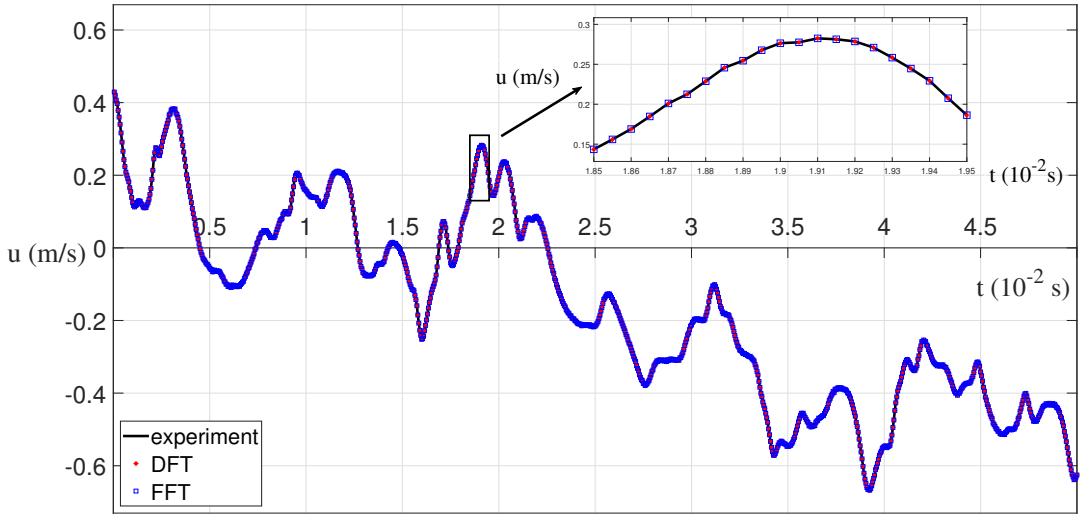

Figure 3.2: DFT and FFT representations of the fluctuation velocities for 1000 samples

These methods represent the fluctuation velocities very accurately, as shown in Fig. 3.2. However, their required computational efforts are so different. Table 3.1 shows the CPU times of the prepared DFT and FFT subroutines and how accurate these subroutines calculate the Fourier coefficients. As can be seen, both methods give very accurate results.

Table 3.1: Comparison of CPU for DFT and FFT

	FFT		DFT	
# of Samples	CPU (s)	Error (%)	CPU (s)	Error (%)
10	1.010	0	1.013	$4x10^{-14}$
100	1.012	$3x10^{-14}$	1.020	$2x10^{-12}$
1000	1.014	$1x10^{-13}$	1.842	$9x10^{-11}$
10000	1.015	$1x10^{-13}$	799.9	$5x10^{-10}$

Nevertheless, the CPU time of DFT has increased significantly, with the N number being 10^4. Therefore, the subroutine written for FFT is decided to be used for the analyses.

Now, it is proceeded to how to calculate the Fourier coefficients of these two subroutines. Firstly, the DFT subroutine calculates the F_N matrix which is composed of power of W_N given in Eqn. A.4. Then, the Fourier coefficients, a_f and b_f, are obtained by multiplying by the instantaneous fluctuation velocity matrix, u_t, as shown in Eqn. A.5. The real part of solution matrix is a_f, and the imaginary part is b_f. For FFT, a_f and b_f are calculated directly with the "fft" command without the need for these. Moreover, the code calculates instantaneous fluctuation velocities with inverse transform. Thus, the error values in the Fourier representation are calculated as given in Table 3.1.

3.3.2.2 Subroutine *freqdspectrum.m*

In this subroutine, the spectrum in the frequency domain is obtained from the Fourier coefficients. First of all, Matlab's "fft" command does not provide frequencies, and the ordering of the Fourier coefficients is also different. The Fourier coefficients found with this command also include negative frequencies. Since negative frequencies are not physically possible to exist, the energies of negative frequencies are transferred to the positive frequencies with the same absolute number. This is because some of the physically existing energy contributions are expressed mathematically in negative frequencies. Thus, a one-sided spectrum is obtained from the two-sided spectrum.

The frequencies at which the resulting Fourier coefficients coincide are primarily from 0 to f_c in hertz. Then, it goes from $-f_c$ to 0. Frequencies are also found as follows:

$$f = \frac{i}{T}, \quad i = 0, ..., \frac{N}{2} \ , \tag{3.1}$$

where T is period and frequency interval is between 0 to f_c which is defined as Nyquist critical frequency in Eqn. 2.14. The Fourier coefficients obtained from Matlab are different from those previously defined. Hence, the frequency-dependent

energy density equation is obtained as follows:

$$E(f) = \frac{1}{N}\frac{a_f^2 + b_f^2}{SR}, \quad f = 0\ , \qquad E(f) = \frac{1}{N}\frac{2(a_f^2 + b_f^2)}{SR}, \quad 0 < f \leq f_c\ . \tag{3.2a}$$

(3.2b)

In this way, the energy contributions of negative frequencies are transferred to positive frequencies. Since the energy contributions of the negative and positive values of the same frequency are found to be the same, Eqn. 3.2b is only multiplied by 2. So, the condition given in Eqn. 2.18 is satisfied as follows:

$$\overline{u^2} = \int_0^{f_c} E(f)df\ . \tag{3.3}$$

It is checked whether this condition is met in the current subroutine. As it can be noticed, the frequencies obtained depending on the sampling rate may not be integers. In the current subroutine, these frequencies are generated as integers, and the energy contributions of integer frequencies are transferred to integer frequencies. In other words, the frequencies are expressed as integers, conserving the total energy for ease of calculation.

3.3.2.3 Subroutine *nondimfreqdspectrum.m*

After obtaining the frequencies and the energy contributions of these frequencies in the previous subroutine, the dimensionless form of the energy contributions must be calculated to be used in the QBT approach. So, the energy density, $E(f)$, is divided by the square of rms of velocity fluctuations, u'^2. As a result, the values of $G(f)$, which has the inverse unit of frequency but is called dimensionless, are calculated. Multiplying $G(f)$ by df gives ΔG, which expresses the dimensionless energy contributions of the frequency ranges. The sum of the ΔG values of all frequency ranges is 1. In other words, the ΔG value of any frequency range shows the contribution of that frequency range to the turbulent kinetic energy over one.

Another task of the current subroutine is to arrange the ΔG and $G(f)$ values according to the frequency ranges determined in the QBT. The mentioned intervals are

among the following frequencies in hertz units: 0, 1, 2, 5, 10, 20, 50, 100, 200, 500, 1000, 2000, 5000, 10000. In the QBT studies of Çıray, who introduced the QBT approach, the intervals are determined in this way, as shown in [69, 70, 72]. These ranges are thought to be sufficient to give an accurate idea of the energy distributions of the eddies. Of course, it is also possible to get different ranges by making a small change in the code. As a result, this subroutine provides dimensionless kinetic energy contributions of specified frequency ranges.

3.3.2.4 Subroutine *ncalculation.m*

In this part of the code, the unique number n is defined for each specific instantaneous velocity data case. The first step in finding this number is to calculate the 2^{nd} order moment, μ_{act}^2, from the actual turbulence intensity, I_{act}, calculated from the data, as shown in Eqn. 2.22. The relationship of this moment with the Gamma function depending on the number n is shown in Eqn. 2.43. Therefore, it is necessary to find a value of n that allows this moment and hence the turbulence intensity to be calculated as accurately as possible.

For this purpose, a loop that controls the margin of error using the number n from 1 to 250 is created. The maximum n number of 250 is determined by considering the values obtained in the applications of this method. The number n is already inversely proportional to the turbulence intensity. It means that the number n greater than 250 corresponds to very low turbulence intensity. The first loop contains the integer n with less than a 5% margin of error that satisfies this case. Next, the fractional value with a margin of error of less than 0.001% is found with a lower stepsize. Creating two loops aims to reach n more efficiently by reducing the number of operations. So, n is calculated. Turbulence intensity and second-order moment are also found using calculated n.

3.3.2.5 Subroutine *pdfxfcalculation.m*

With the knowledge of the number of n, it is possible to find the properties of the PDF. First of all, the number A is calculated by Eqn. 2.39; after finding A, $P(1)$ is

estimated by using Eqn. 2.33. As can be seen from Eqn. 2.35, by specifying these parameters, the PDF becomes a function that depends only on the unknown x. Now, x needs to be initialized before the calculation procedure of the PDF and x can begin. Eqn. 2.55 is used for this process. As x_1 also knows, the parameters C_1 and C_2 are calculated. For this purpose, the values of the right and left sides of PDF and their derivatives and x are used, as shown in Eqn. 2.52 and 2.53. Thus, Eqn. 2.51 becomes a quadratic equation with one unknown, Δx. By finding the positive root of this equation, the Δx is found. This stepsize is added to the current x, and the calculation procedure is repeated in the same way for the entire determined frequencies. Thus, x, P_R, and P_L corresponding to all determined frequencies are calculated. Finally, using Eqn. 2.58, from the first three combinations of f and x, the number B is also defined.

3.3.2.6 Subroutine *wavenumbercalculation.m*

In this subroutine, the numbers x_b and f_b specified in Eqn. 2.58 are defined using the first three combinations of f and x. Thus, wavenumber calculations can be started. The k_1 value is obtained using Eqn. 2.59 and, knowing the wavenumber, the wavelength and phase velocity are calculated via Eqn. 2.62 and 2.63. In the continuation of the calculations, by substituting x and f in Eqn. 2.61, wavenumbers corresponding to entire frequencies are found in order.

3.3.3 Outputs of the Code

Until this part, the content of the code is explained, necessary inputs, calculation steps, and subroutines are introduced. Although the outputs of the code are mentioned, it is useful to say it collectively:

- The energy contributions of the frequency ranges are obtained by applying the spectral approach from the code.
- The dimensionless fluctuation velocities, x, depending on the frequencies and the PDF values of these velocities, are calculated. Since the selected PDF is known to be skewed, its right and left sides, P_R and P_L, are calculated sepa-

rately.

- By obtaining the relation between frequency and fluctuation velocities, wavenumbers, wavelengths, and phase velocities are found for each selected frequency.

In Chapter 5, these outputs are shown.

3.3.4 Verification of the Calculation Procedure of the Code

As can be seen from the previous sections, this code contains many calculation steps. These calculations are verified by comparing them with the calculations of 10 different turbulent flow cases mentioned in Çıray's first study on QBT [69]. Minor differences are observed in the results, and this difference is attributed to the calculation conditions between then and now.

CHAPTER 4

SETUP OF TWO EXPERIMENTS SELECTED FROM LITERATURE

4.1 Introduction

In this chapter, the properties of the experimental data to be analyzed by the developed code are introduced. All required information, such as specific test sections of experiments and the conditions under which the experiments are carried out, are given. The first data set that is analyzed belongs to the study of Dogan et al. [27] and consists of several different boundary layer flow cases. The second data set used is the atmospheric boundary layer data of Abdulrahim et al., and the analysis results are explained in Chapter 5.

4.2 Experimental Setup and Detailed Information of Boundary Layer Data of Dogan et al.

Dogan et al. performed experiments for 20 different freestream turbulence (FST) cases generated by active grids and 1 case for no active grid used with zero pressure gradient [27].
In this study, three of those cases are analyzed. Therefore, the details of these flow cases are given. The cases are named differently from the referenced article, and these names are given in Table 4.1. In addition, all cases of their experiments and more detailed information can be found in this article.

Experimental measurements are conducted in a suction-type wind tunnel at the University of Southampton by Dogan et al. [27]. This wind tunnel has a 0.9 m wide x 0.6 m high x 4.5 m long size test section. Over a 4.2 m long flat plate which is

Table 4.1: The names of the different flow cases in this study, the corresponding names in Dogan et al.'s study and the active grid type used

Present study	Dogan et al. [27]	Active grid
Case 0	No-FST Case	No active grid
Case 1	FST-Case A	Cut-out Wings
Case 2	FST-Case C	Solid Wings

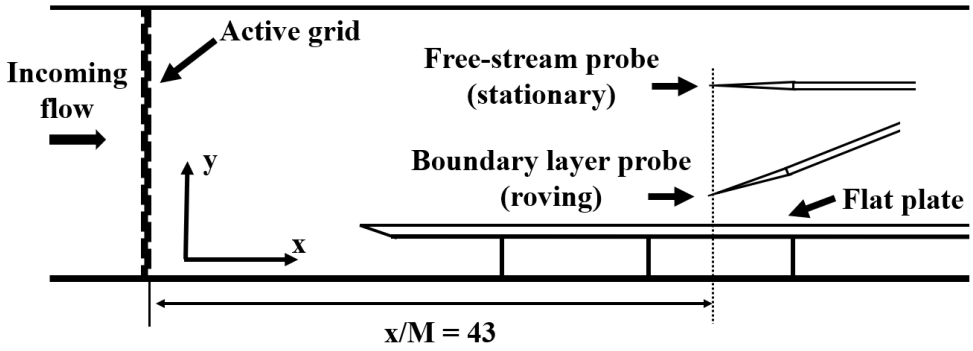

Figure 4.1: Schematic of test section of boundary layer experiment of Dogan et al. [27] reproduced from their Fig. 1

0.135 m above the ground of the test section, the turbulent boundary layer is generated as shown in Fig. 4.1. The leading edge of the used flat plate is placed at 0.3 m downstream of the test section entrance.

While there is no active grid used in Case 0 measurements, two different active grids in Fig. 4.2 and 4.3 are used to generate turbulence for Case 1 and 2. The solid wings used in Case 2 have higher solidity than cut-out wings used in Case 1. Therefore, they create a higher turbulence intensity level. The length of the square mesh of both active grids is 81 mm (M).

Two hotwires are used for instantaneous velocity measurements. It is $43M$ away from the entrance of the test section, where measurements are done. One of these hotwires is fixed at 27 cm above the flat plate, and measures the instantaneous velocity in

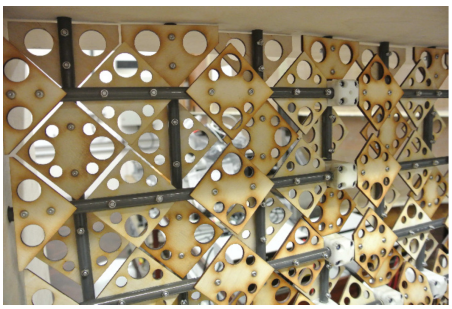

Figure 4.2: Cut-out wings used as active grid in Case 1 [27]

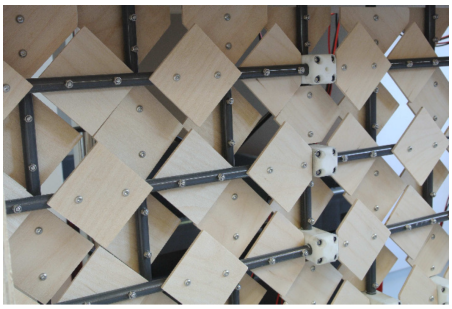

Figure 4.3: Solid wings used as active grid in Case 2 [27]

the freestream. Using the other hotwire, instantaneous velocities are measured at 28 different distances from the wall in the boundary layer. Measurement points are more frequent near the wall and sparse for far from the wall.

Table 4.2: Some fluid and mean flow properties of cases

Case	Fluid	Density ρ	Dynamic viscosity, μ	Mean velocity, $\overline{U}$	Reynolds number, Re_x
-	-	[kg/m^3]	[kg/(m.s)]	[m/s]	-
Case 0	air	1.1654	1.8158x10^{-5}	10.11	2.2x10^6
Case 1	air	1.1810	1.8249x10^{-5}	6.11	1.5x10^6
Case 2	air	1.1970	1.8319x10^{-5}	7.96	1.8x10^6

The airflow is measured in the experiments, and the fluid properties and mean velocity of freestream for each case are given in Table 4.2.

The atmospheric pressure, p_{atm}, measured during the experiments are between 101-103 kPa and the ambient temperature, T_a, is between 20-24°C. The sampling rate, duration, and turbulence intensity levels for the three flow cases mentioned are given in Table 4.3.

Table 4.3: The sampling rates, durations of experiments, and turbulent intensity levels of FST specific to each case

Case	Sampling Rate, SR	Duration, T	Turbulence intensity, I
-	[kHz]	[s]	[%]
Case 0	80	140	0.7
Case 1	20	360	7.4
Case 2	20	360	12.2

4.3 Experimental Setup and Detailed Information of Atmospheric Boundary Layer Data of Abdulrahim et al.

Abdulrahim et al. conducted experiments to create an atmospheric boundary layer (ABL) in the wind tunnel. While some of these experiments are included in their paper [1], unpublished two cases are used in this study. In one of these cases, ABL is generated using spires. These spires are triangular plates replaced at the entrance of the test section. They provide to generate the windspeed profile of the boundary layer [61].

Table 4.4: The names and characteristics of cases of Abdulrahim et al.

Present study	Characteristic of case
Case 3	Boundary layer of empty test section
Case 4	Atmospheric boundary layer generated by spires

Abdulrahim et al. conducted these experiments in the open-return suction type wind tunnel at Middle East Technical University Center for Wind Energy Research (METU-RÜZGEM). The size of this wind tunnel is 1 m wide x 1 m high x 8 m long. The height of spires is 0.67 m. The boundary layer is generated at the bottom of the test section. Instantaneous velocities are measured 7 m downstream from the test section entrance and at 175 different heights. These positions are at 2 mm intervals from the bottom of

the test section at the height range of 0-25 cm and 5 mm intervals at the height range of 25-50 cm.

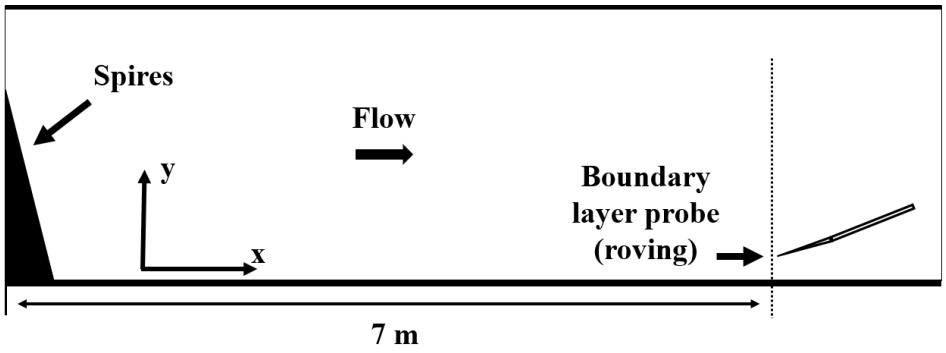

Figure 4.4: Schematic of test section of atmospheric boundary layer experiment of Abdulrahim et al. [1] reproduced from their Fig. 3 with minor modifications

Table 4.5: Some fluid and mean flow properties of cases

Case	Fluid	Density ρ	Dynamic viscosity, μ	Mean velocity, $\overline{U}$	Reynolds number, Re_x
-	-	[kg/m^3]	[kg/(m.s)]	[m/s]	-
Case 3	air	1.0633	1.9374x10^{-5}	10.93	4.2x10^6
Case 4	air	1.0633	1.9374x10^{-5}	10.93	4.2x10^6

Some fluid and freestream flow properties of cases of Abdulrahim et al. are given in Table 4.5.

Table 4.6: The sampling rates, durations of experiments, and turbulent intensity levels of FST specific to each case

Case	Sampling Rate, SR	Duration, T	Turbulence intensity, I
-	[kHz]	[s]	[%]
Case 3	10	60	0.5
Case 4	10	60	2.1

The ambient temperature, T_a, measured during the experiments are between 21-22^{o}C. Other important parameters such as sampling rate, duration, and turbulence intensity levels of the two cases are shown in Table 4.6.

In Chapter 5, the velocity profile specific to the boundary layer test cases, the selected points for analysis, and the analysis results are discussed.

CHAPTER 5

EVALUATION OF EXPERIMENTS WITH QBT APPROACH

5.1 Introduction

In this chapter, calculations either in tabular form or as figures are presented. The calculations are made entirely with respect to QBT and associated mathematics. For the calculations, raw data coming from measurements of the researchers are used. The raw data is basically time series of measured instantaneous velocities. These data are from Dogan et al. [27] and Abdulrahim et al. [1] and their contribution are as raw data in figures and tables.

5.2 Results of Boundary Layer Data of Dogan et al.

In this study, three boundary layer data cases of Dogan et al. are analyzed. Detailed information about these cases is explained in Chapter 4. As mentioned before, instantaneous velocities are measured both at the boundary layer and freestream in these experiments. In this study, by QBT, the point where freestream velocity is reached in the boundary layer is analyzed. It is observed that there is no significant difference between this point and freestream. Therefore, it is decided that there is no need to analyze the freestream, and analyzing mentioned points in boundary layer (D points to be detailed later) are sufficient to obtain the results of the freestream.

In this section, selected points for analysis in the boundary layer and the velocity profiles of the cases are introduced. The PDF of the selected points and the compatibility of the PDF to the data are evaluated. Afterwards, frequency-dependent spectrum, spectrum in the wavenumber domain are shown and discussed. Finally, the eddy

sizes and lifespans of all measurement points for three cases are compared.

5.2.1 Velocity Profiles and Measurement Points of Cases of Dogan et al.

The velocity profiles of Dogan et al.'s three cases in the boundary layer are shown in Fig. 5.1. For analysis, four different points are selected on each profile. The selected points can be classified as:

- A points are close to the wall and have high u'.
- B points are before the curved parts of the velocity profiles.
- C points are after the curved parts of the velocity profiles.
- D points are points where the velocities reach the freestream velocities.

In addition, the points selected for each case are chosen to reach approximately the same percentage of their velocity profile. For example, points A have their freestream velocity at the same percentage. It is decided in this way so that the comparison of these points is meaningful.

In Table 5.1, 5.2, and 5.3, some information about the selected points such as measurement location, y, mean velocity, U_m, root mean square of velocity fluctuations, u', actual and calculated turbulence intensity, I_{act}, I_{calc}, and the determined number, n is given for Case 0, 1, and 2, respectively. As previously stated in Chapter 3, in the QBT approach, actual turbulence intensity is used to find the determined number n for each case. Calculated turbulence intensity is found by using the number n. Both parameters for each point are shown in the given tables. As seen from the tables, the number n corresponds to smaller numbers for high turbulence intensities and higher numbers for low turbulence intensities. When the actual and calculated turbulence intensities are compared, it can be seen that the calculated turbulence intensity is obtained correctly using the determined number n for each case.

An important point to remember is how turbulence is generated in these cases. Since the active grid is not used in Case 0, turbulence intensities are lower than in other cases, as shown in Table 5.1. Even at the freestream point (Point 0D), the turbulence

intensity is 0.7%. In Case 1, cutout wings with lower solidity than solid wings are used as an active grid. Therefore, intensities in Table 5.2 are higher than Case 0. In Table 5.3, the highest intensities are observed in Case 2, where solid wings are used.

Table 5.1: Information about the selected measurement points of Case 0 (from raw data of Dogan et al. [27])

Point	y [cm]	U_m [m/s]	u' [cm/s]	I_{act} [%]	I_{calc} [%]	n [-]
Point 0A	0.10	4.69	103	21.9	21.9	4.63
Point 0B	0.87	7.16	73.7	10.3	10.3	11.1
Point 0C	3.55	9.46	42.4	4.48	4.48	27.2
Point 0D	10.9	10.1	7.11	0.70	0.70	181

Table 5.2: Information about the selected measurement points of Case 1 (from raw data of Dogan et al. [27])

Point	y [cm]	U_m [m/s]	u' [cm/s]	I_{act} [%]	I_{calc} [%]	n [-]
Point 1A	0.10	2.83	77.7	27.4	27.4	3.50
Point 1B	0.47	4.29	61.8	14.4	14.4	7.60
Point 1C	3.98	5.71	52.9	9.26	9.26	12.5
Point 1D	17.2	6.13	45.0	7.35	7.35	16.1

Table 5.3: Information about the selected measurement points of Case 2 (from raw data of Dogan et al. [27])

Point	y [cm]	U_m [m/s]	u' [cm/s]	I_{act} [%]	I_{calc} [%]	n [-]
Point 2A	0.08	3.83	110	28.7	28.7	3.31
Point 2B	0.36	5.54	98.0	17.7	17.7	5.97
Point 2C	3.83	7.35	101	13.8	13.8	7.98
Point 2D	24.5	7.98	94.7	11.9	11.9	9.47

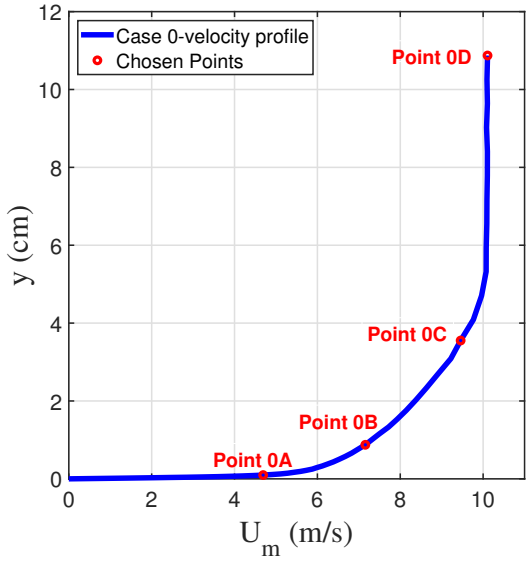

(a) Velocity profile and measurement points of Case 0

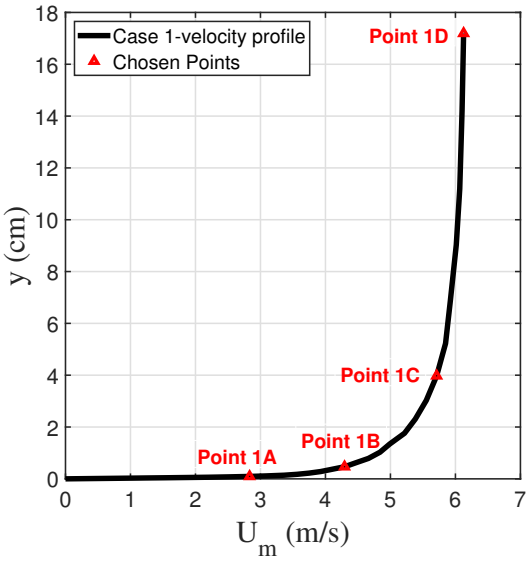

(b) Velocity profile and measurement points of Case 1

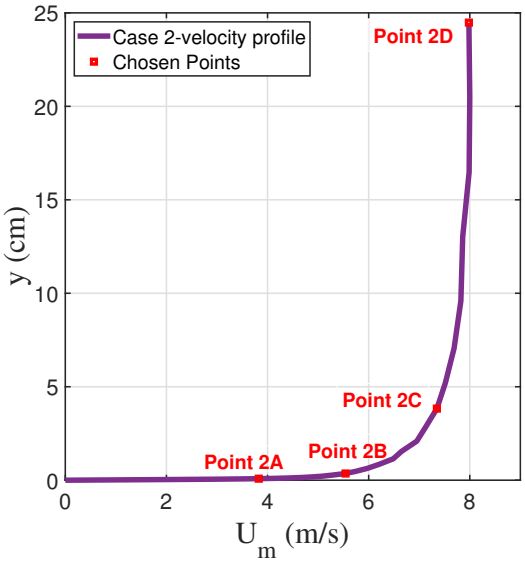

(c) Velocity profile and measurement points of Case 2

Figure 5.1: Velocity profiles generated by Dogan et al.'s raw data and measurement points (from raw data of Dogan et al. [27])

5.2.2 PDFs of Measurement Points of Cases of Dogan et al.

In the QBT approach, PDF is required to find wavenumbers corresponding to frequencies. Chosen PDF depends on the number n. Therefore, with the knowledge n,

it is obtained uniquely for each case. This section consists of PDFs of chosen points. PDFs are plotted with the histograms to evaluate how accurately PDFs represent the data of chosen points. For this purpose, histogram is plotted by dividing the number of samples, N, to be able to compare with the chosen PDF. Also, stepsize of chosen intervals of histogram columns is also taken into consideration.

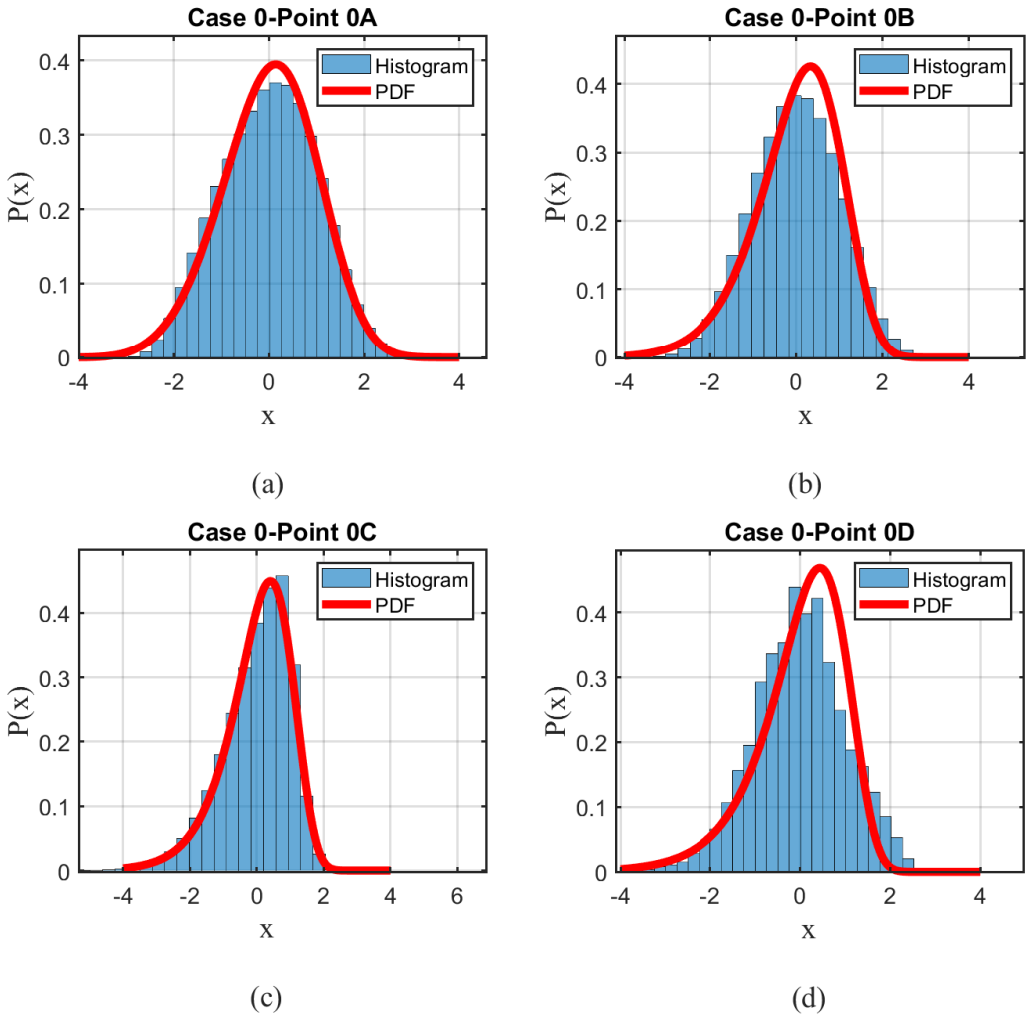

Figure 5.2: Histogram vs PDF of measurement points of Case 0 (from raw data of Dogan et al. [27])

By definition, PDF shows the possibilities of dimensionless fluctuation velocity ranges. Therefore, the area under the PDF curve is one. On the other hand, the histogram shows in columns how many samples are included in the velocity ranges determined in the experimental data. For each selected point, the histogram values are divided by

N. Thus, it is aimed to evaluate how accurately the PDF modified by Çıray represents the experimental data.

The histogram and PDF of each point are given in Figs. 5.2, 5.3, and 5.4 for Case 0, 1, and 2, respectively. From these figures, it can be observed that the histogram is wide when the points are closer to the wall. When the point gets closer to the freestream, the histogram becomes narrow. For all points, the distribution of velocity fluctuations changes smoothly in given histograms. However, Point 0D has some irregularities. The reason may be related to measurement mistakes or problems about reducing this data from measurements of cross wire.

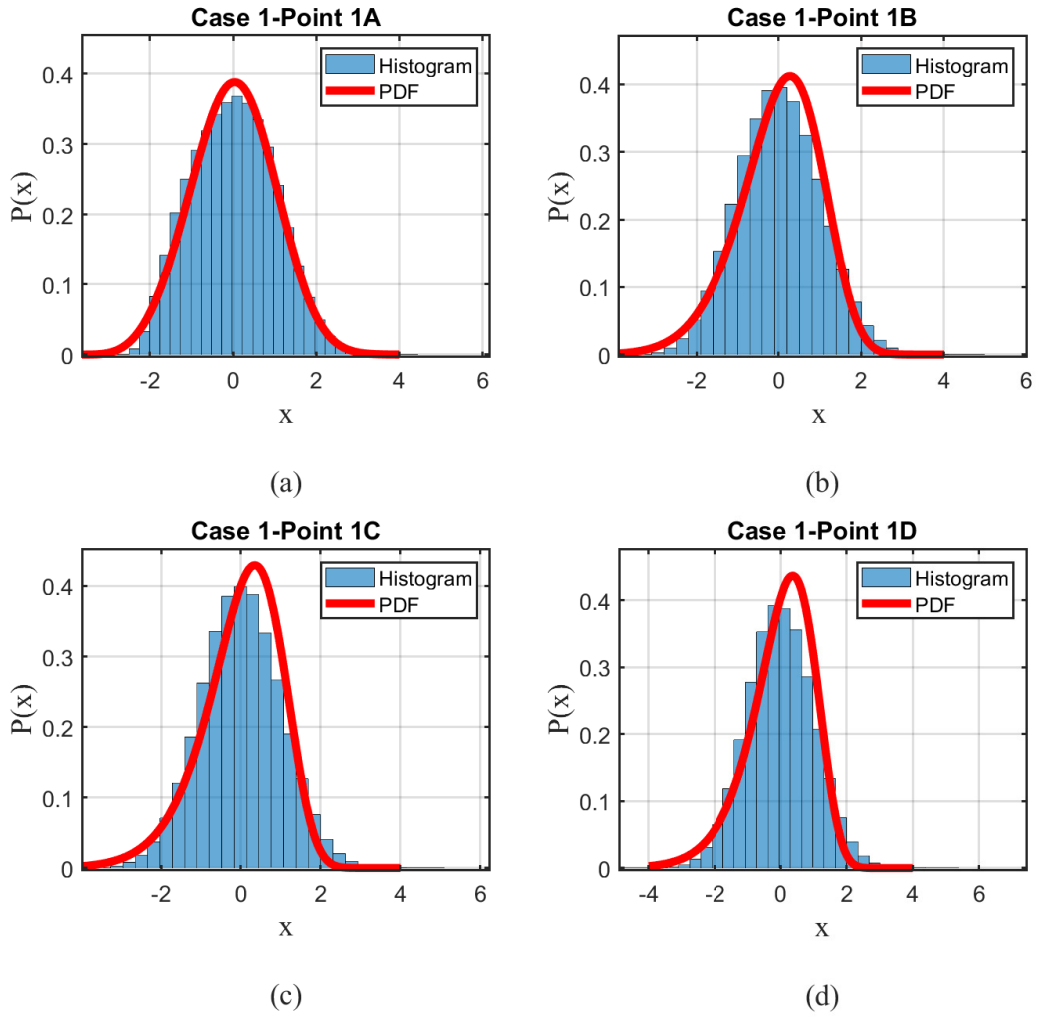

Figure 5.3: Histogram vs PDF of measurement points of Case 1 (from raw data of Dogan et al. [27])

As can be seen from Figs. 5.2, 5.3, and 5.4, and Tables B.1 to B.12 at Appendix B, the non-dimensional fluctuation velocities, x, increase when the eddy sizes and PDF values reduce. Then, they become fixed at some frequencies. In other words, the probability of the existence of these velocity fluctuations decreases at higher frequencies. This is true for positive and negative fluctuations. Even though, the probabilities of positive and negative velocity fluctuations are different due to the skewness of PDF; their behavior is the same. Another observation is that PDF is almost symmetric and wide for high-intensity points while it becomes more right-skewed for lower intensity points.

When the compatibility of the experimental data with the PDF created with QBT is compared, it is observed that they are quite compatible. For Case 0, at Points 0A and 0C, the PDF represents the data quite accurately. At Point 0B, there is a slight mismatch. PDF of Point 0D is inconsistent with its histogram, and there is an irregularity in the distribution of the experimental data that is not seen in other data. This mismatch and irregular distribution may be due to errors in experimental measurements.

In Cases 1 and 2, the PDF and histogram of Points 1A and 2A are obtained consistently. As the point gets closer to the freestream, the inconsistent part occurs and becomes more apparent. However, the level of incompatibility mentioned is still acceptable. So, the representation of the experimental data of the PDFs is still quite adequate.

Moreover, a comparison of PDFs of similar points of each case is shown in Fig. 5.5. The change of PDF is different for points A, B, C, and D. For instance, points A have more similar PDFs than points B, C, and D. This is an expected result because A points have high turbulence intensity in every case. PDF is the function of the number n obtained based on the turbulence intensity. As the A points have n numbers close to each other (Tables 5.1 to 5.3), their PDFs are also similar.

For points B, C, and D, the similarities of the PDFs decrease as the points are far from the wall due to different turbulence intensities. Another observation is that the skewness of the PDF increases as the intensity decreases. Also, the peak of the PDF rises with decreasing intensity. The probability density is concentrated at and around the peak.

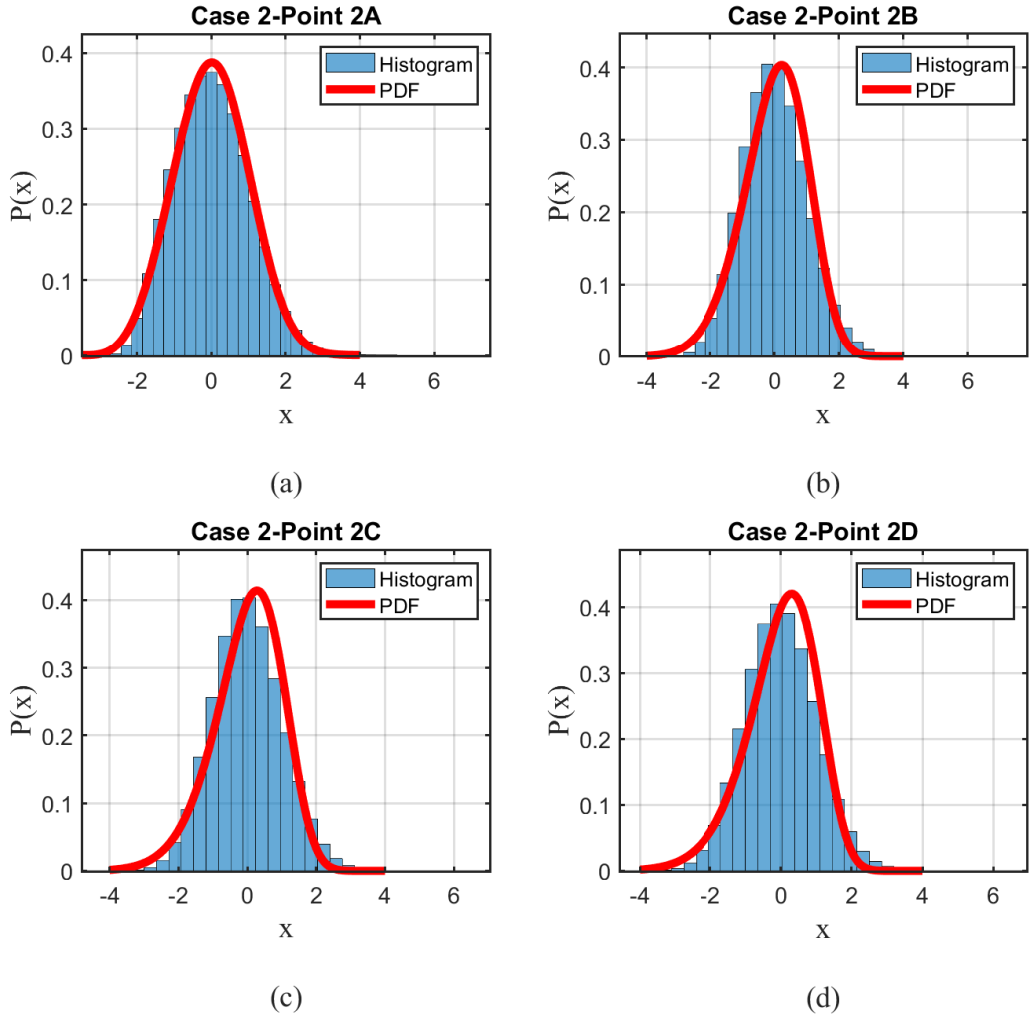

Figure 5.4: Histogram vs PDF of measurement points of Case 2 (from raw data of Dogan et al. [27])

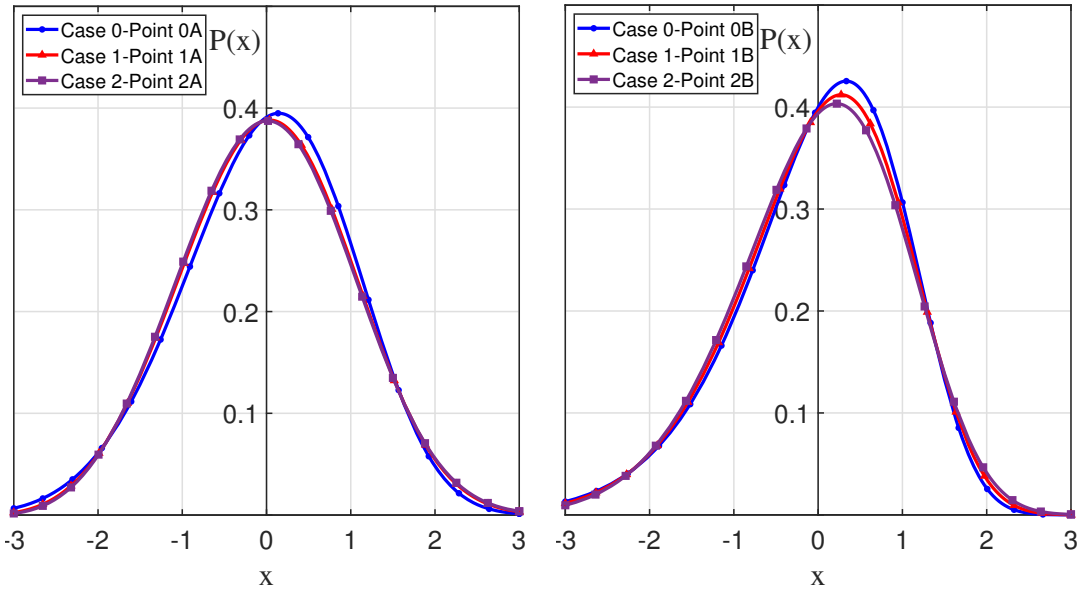

(a) A points

(b) B points

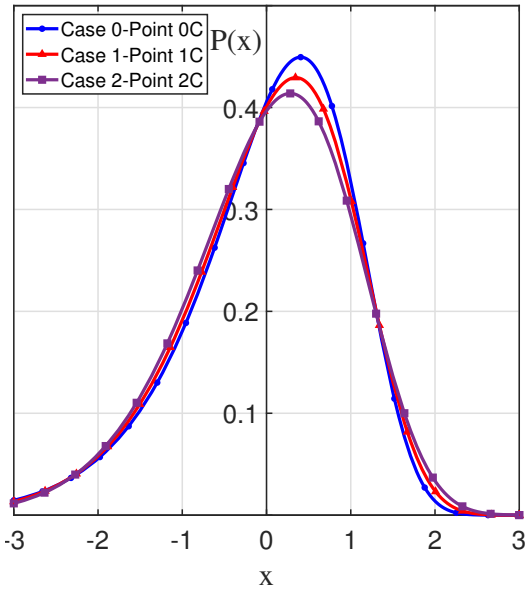

(c) C points

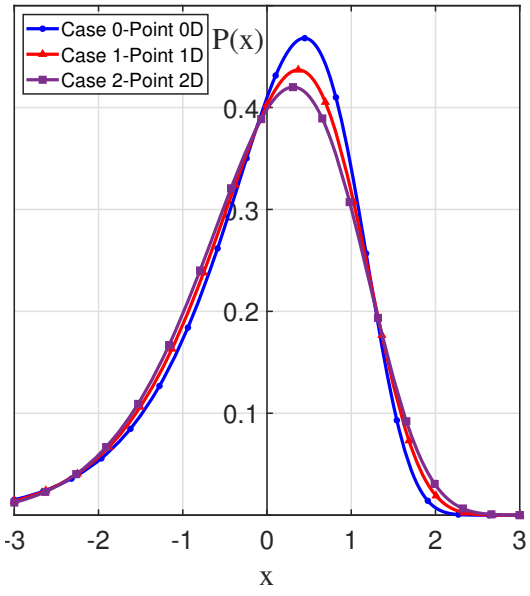

(d) D points

Figure 5.5: PDFs of measurement points (from raw data of Dogan et al. [27])

5.2.3 Energy Spectrums in Frequency Domain of Measurement Points of Cases of Dogan et al.

This section includes the frequency-dependent energy spectrums obtained by the spectral approach. For all points, spectrums are shown in Fig. 5.6. In these plots,

$G_f(f)$ is the non-dimensionalized energy density function with respect to frequency.

According to the sampling theorem, Nyquist critical frequency (maximum frequency at energy spectrum) is found using Eqn. 2.14. This frequency is half of the sampling rate and corresponds to 40 kHz for Case 0 and 10 kHz for Case 1 and 2. As a result of spectral analysis of Case 0, it is observed that the energy contribution of frequencies higher than 10 kHz is less than 0.0001% of total kinetic energy. Therefore, the energy contributions at a maximum of 10 kHz are considered. These contributions for all chosen points are shown in Tables B.1 to B.12 at Appendix B.

Considering the energy contributions of the frequency intervals, it is observed that about 90-95% of the energy is in 0-200 Hz range. As a result of this observation, it is possible to say that large and energetic eddies are in the frequency range up to 200 Hz. In the frequency-dependent spectrum of the selected points in Fig. 5.6, the spectrum function approaches zero from 200 Hz. It continues in the same way at high frequencies.

At A, B and C points of Case 0, the energy levels are lower than those of Case 1 and 2. Since the active grid is not used in Case 0, the low energy level of turbulence is consistent with the physics of the flows. However, this situation is different at Point 0D. Energy is concentrated at low frequencies, and it is very low at other frequencies. The energy density of Case 2 is highest at points A and B. At C points, the energy density of Case 1 is higher, while at points D, it is the same for Case 1 and 2.

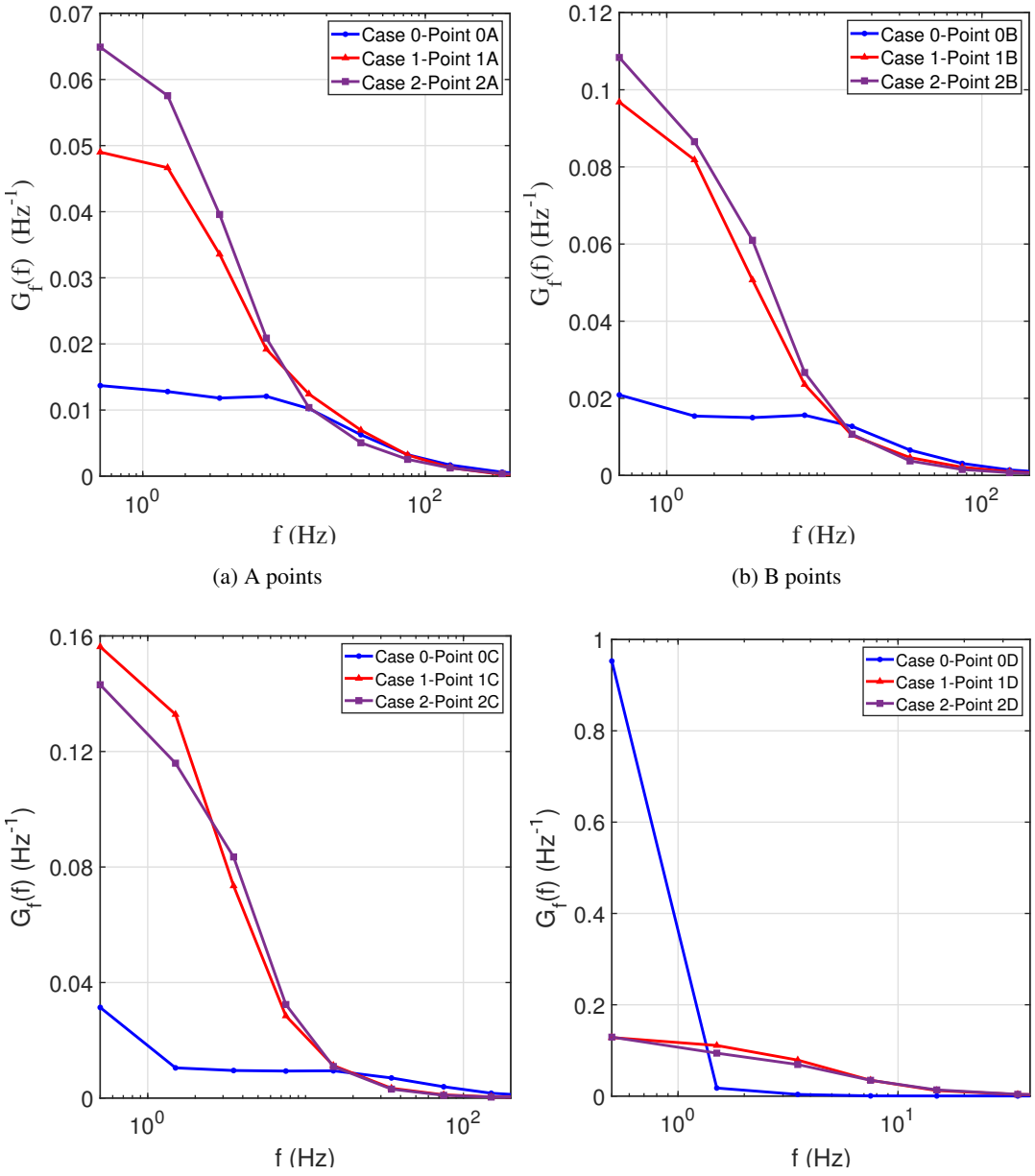

(a) A points

(b) B points

(c) C points

(d) D points

Figure 5.6: The energy spectra in the frequency domain of measurement points (from raw data of Dogan et al. [27])

5.2.4 Energy Spectrums in Wavenumber Domain of Measurement Points of Cases of Dogan et al.

In this section, the energy spectrums in the wavenumber domain obtained by QBT are examined. In turbulent flow studies about eddy sizes, the wavelengths (correspond to wavenumbers) are associated with eddy sizes. Therefore, the energy contribution in the frequency domain transforms to the wavenumber domain by the QBT approach. Calculated wavenumbers represent the different ranges of eddy sizes. Large eddies are strongly affected by the boundary conditions of flow, and they correspond to the smaller wavenumbers. Fig. 5.7 consists of the spectrums in the wavenumber domain of chosen points, and these spectrums have different characteristics in the region of smaller wavenumber. In the inertial subrange, the slope of the spectrum is consistent with the previous related studies in the literature. When the point gets closer to the freestream, -5/3 slope region becomes broader and more apparent. The frequency range of this region is observed at approximately between 50 and 500 Hz. As a reference line for this range, the 200 Hz line is shown in each plot of Fig. 5.7. After the inertial subrange, the region of dissipating eddies appears. In this range, the slope of the curve changes, and energy is dissipated very rapidly. The behaviors of inertial subrange and dissipating eddies range are compatible with the studies in the literature.

For all cases, when the point gets closer to the freestream, its spectrum curve approaches the spectrum of its freestream. Considering the spectrums of Case 2, it is observed that the spectrum curves start from lower wavenumbers; that is, they contain eddies of larger sizes. This is a correct conclusion because there is a more effective source for turbulence generation in this case. In addition, this case has a higher energy density for small wavenumbers, so, large eddies. In Case 2, high wavenumbers correspond to lower energy levels than Cases 0 and 1. This situation differs in freestream points. At Point 0D, the freestream point of Case 0 in Fig. 5.7d, most energy accumulates in the large eddies. This is consistent with the frequency-dependent energy distribution of this point. Likewise, this point has a relatively high energy contribution in the 2000-10000 Hz frequency range compared to the previous ranges. This contribution shows itself with a slight increase in the last part of the curve. The spectrum of Point 0D is different from the others. The reason may be the irregularity in

the distribution of data, as seen in its histogram in Fig. 5.4d.

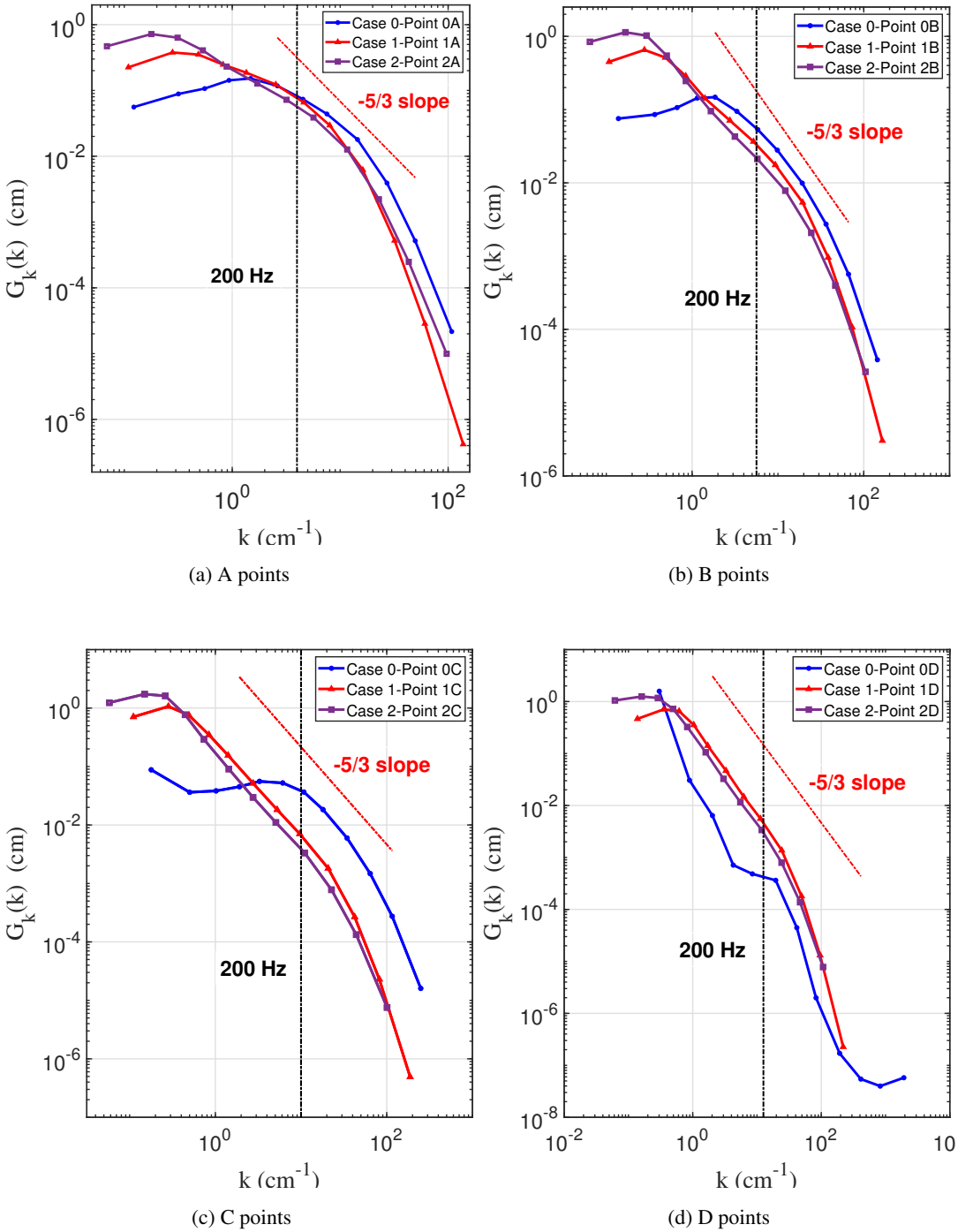

(a) A points (b) B points

(c) C points (d) D points

Figure 5.7: The wavenumber-dependent energy spectra of measurement points (red dashed line: $-5/3$ slope, black dashed line: approximately 200 Hz for three cases) (from raw data of Dogan et al. [27])

5.2.5 Sizes and Lifespans of Measurement Points of Cases of Dogan et al.

In this section, the size and lifespans of eddies of the chosen points are discussed. In Tables 5.4 to 5.7, sizes and lifespans of the largest eddies at 1 Hz and the smallest eddies at 10000 Hz are given for all cases. As can be seen from the results, the sizes of the largest eddies do not exceed the physical boundaries of the flow domain. Therefore, obtained results are considered realistic.

Table 5.4: The size and lifespan of the largest and smallest eddies of A points (from raw data of Dogan et al. [27])

Measurement Point -	Size of the Largest Eddy (at 1 Hz)	Size of the Smallest Eddy (at 10^4 Hz)	Lifespan of the Largest Eddy (at 1 Hz)	Lifespan of the Smallest Eddy (at 10^4 Hz)
POINT 0A	4.080 cm	33.60 μm	0.106 s	15.59 μs
POINT 1A	4.583 cm	25.77 μm	0.103 s	15.79 μs
POINT 2A	7.239 cm	36.88 μm	0.105 s	15.74 μs

Table 5.5: The size and lifespan of the largest and smallest eddies of B points (from raw data of Dogan et al. [27])

Measurement Point -	Size of the Largest Eddy (at 1 Hz)	Size of the Smallest Eddy (at 10^4 Hz)	Lifespan of the Largest Eddy (at 1 Hz)	Lifespan of the Smallest Eddy (at 10^4 Hz)
POINT 0B	3.610 cm	25.34 μm	0.114 s	15.53 μs
POINT 1B	4.640 cm	21.67 μm	0.105 s	15.75 μs
POINT 2B	7.764 cm	34.12 μm	0.106 s	15.73 μs

The sizes of the largest eddies are in the order of cm, and they are the highest for Case 2 and the lowest for Case 0. Also, it should be pointed out that those of Case 2 are also comparable values with the length of the square mesh of the active grid (M = 8.1 cm). Another observation is that the largest eddies are near the wall except

Table 5.6: The size and lifespan of the largest and smallest eddies of C points (from raw data of Dogan et al. [27])

Measurement Point -	Size of the Largest Eddy (at 1 Hz)	Size of the Smallest Eddy (at 10^4 Hz)	Lifespan of the Largest Eddy (at 1 Hz)	Lifespan of the Smallest Eddy (at 10^4 Hz)
POINT 0C	2.800 cm	14.69 μm	0.136 s	15.49 μs
POINT 1C	4.522 cm	18.84 μm	0.102 s	15.83 μs
POINT 2C	8.626 cm	35.04 μm	0.104 s	15.82 μs

Table 5.7: The size and lifespan of the largest and smallest eddies of D points (from raw data of Dogan et al. [27])

Measurement Point -	Size of the Largest Eddy (at 1 Hz)	Size of the Smallest Eddy (at 10^4 Hz)	Lifespan of the Largest Eddy (at 1 Hz)	Lifespan of the Smallest Eddy (at 10^4 Hz)
POINT 0D	1.658 cm	1.817 μm	0.154 s	15.91 μs
POINT 1D	3.627 cm	16.10 μm	0.103 s	15.83 μs
POINT 2D	8.130 cm	33.19 μm	0.109 s	15.81 μs

for Case 2 because velocity gradients are at the significant values there. Since solid wings are used for turbulence generation in Case 2, the largest eddies are observed in freestream. But still, the largest eddies near the wall in Case 2 have quite close sizes with freestream sizes. Depending on the efficiency of the source for turbulence generation, the sizes of eddies change. For instance, the sizes of Case 0 are the smallest because there is no active grid used. The sizes are obtained larger for higher solidity wings, Case 2 than Case 1. Even so, the sizes of the largest eddies for all cases are comparable with the mesh size. The sizes of the smallest eddies are found in the order of ten micrometers and similar to each other. However, the most apparent difference is observed between Point 0D and others.

Lifespans of the largest eddies are in the order of one-tenth of a second. Those of the smallest eddies are in the order of ten microseconds. It is observed that lifespans of both the largest eddies and smallest eddies are similar among themselves for all cases.

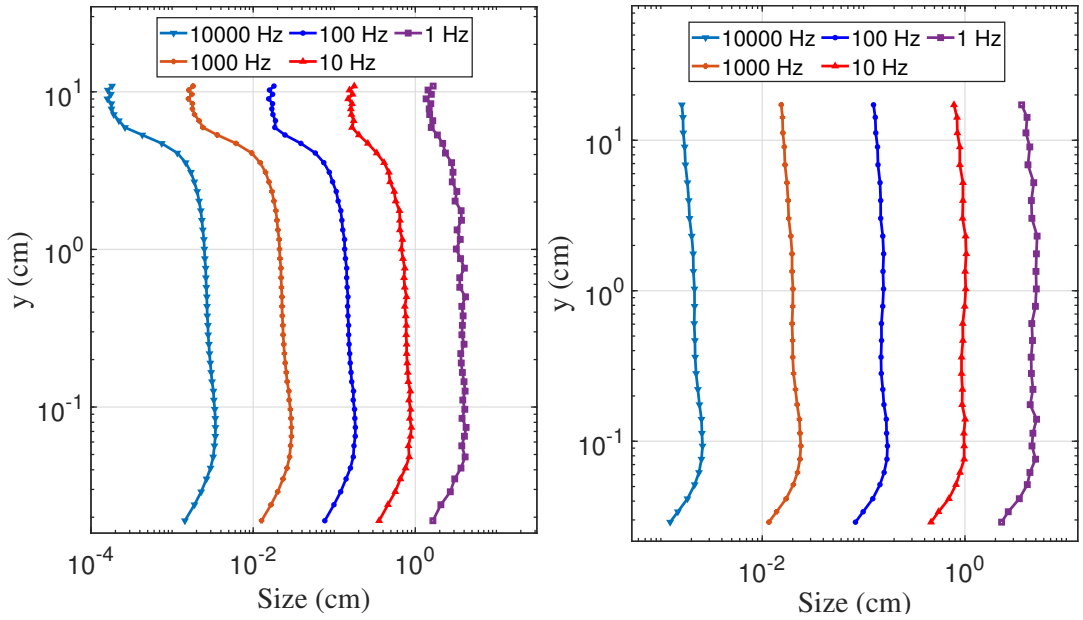

(a) Case 0

(b) Case 1

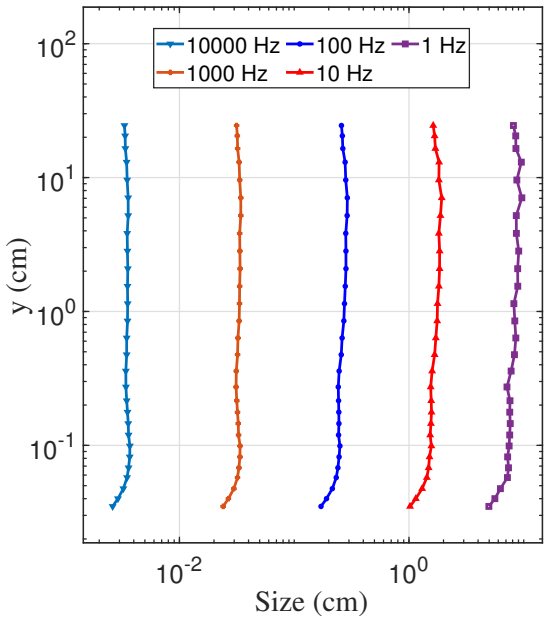

(c) Case 2

Figure 5.8: The size variation of eddies at different frequencies along the boundary layer for all cases (from raw data of Dogan et al. [27])

The change of size along boundary layer at different frequencies is shown in Fig. 5.8. At small frequencies, large eddies are observed, and sizes are significant. Behaviors of small frequency curves change irregularly. This is an expected result due to the character of large eddies since they are highly influenced by boundary and initial conditions. In this logarithmic scale, each frequency curve behaves similarly, but they become smoother for higher frequencies. This statement is valid for each case in itself. This smoother behavior confirms the universality of small eddies at higher frequencies.

If three cases are compared, it is possible to say that the size curves have the same behavior near the wall. In the region between the wall and freestream, the behaviors are also similar for all three cases. However, at points close to the freestream, the effect of the source of the freestream turbulence is noticeable. For example, in Case 0, in which no active grid is used, sizes in the freestream are considerably reduced compared to those near the wall. This result is consistent with the low turbulence intensity values around the freestream. The source in Case 1 is more effective than in Case 0. In Case 1, sizes of the eddies close to freestream decrease a little, although not as much as Case 0. This decrease is least in Case 2 because turbulence is generated with solid wings. The turbulence intensities in the freestream are highest compared to other cases. Therefore, larger eddies exist in the freestream of Case 2 than Case 0 and 1.

Lifespan curves in Fig. 5.9 can be evaluated similarly to size curves. It is irregular at low frequencies for all cases and becomes smoother and universal as the frequency increases. The effect of the source of turbulence generation is observed around the freestream. Also, it is possible to say that the lifespan values at the same frequency are of the same order.

The eddy sizes of the three cases at the same frequencies are shown in Fig. 5.10 for a clear comparison. The irregularity of large eddies at 1 Hz is also more noticeable, and as the frequency increases, they become smoother. For each frequency, the effect of the freestream is also apparent specific to the cases.

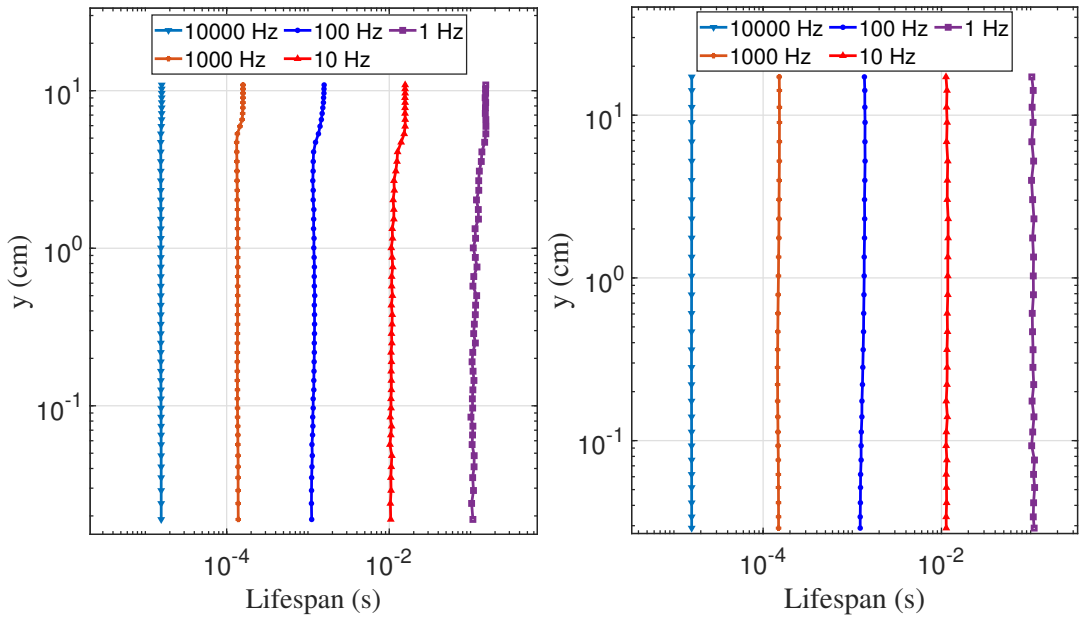

(a) Case 0

(b) Case 1

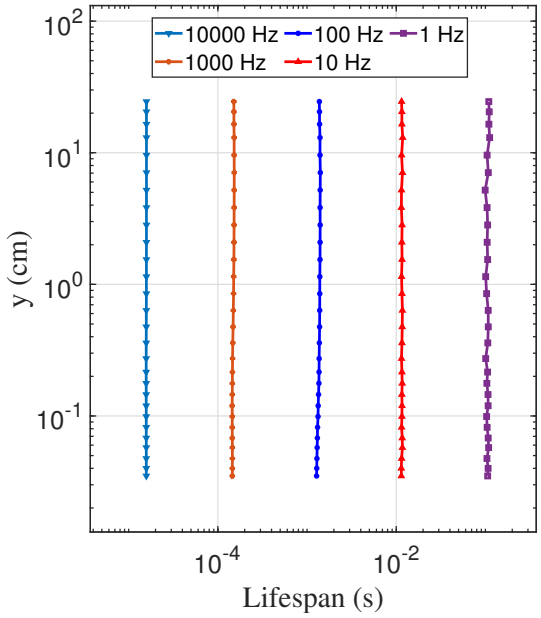

(c) Case 2

Figure 5.9: The lifespan variation of eddies at different frequencies along the boundary layer for all cases; (from raw data of Dogan et al. [27])

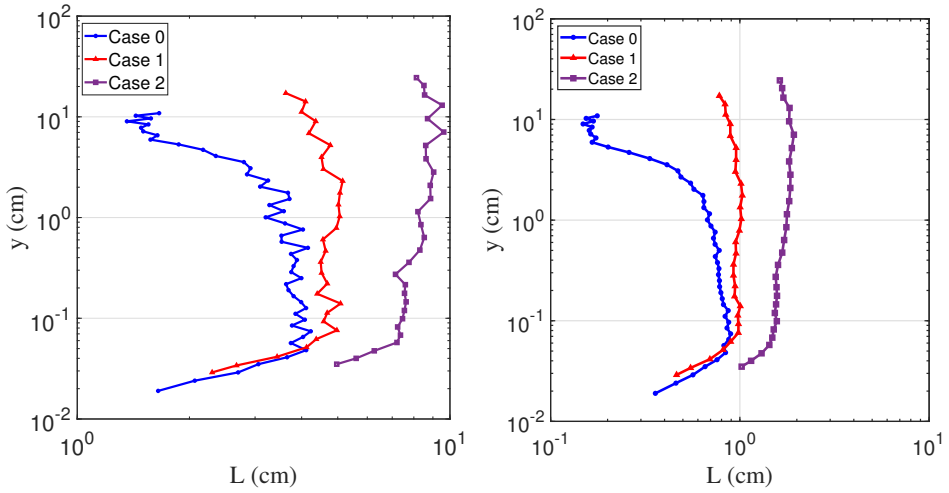

(a) at 1 Hz

(b) at 10 Hz

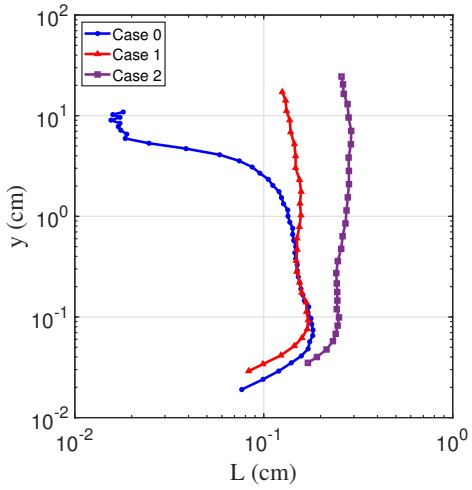

(c) at 100 Hz

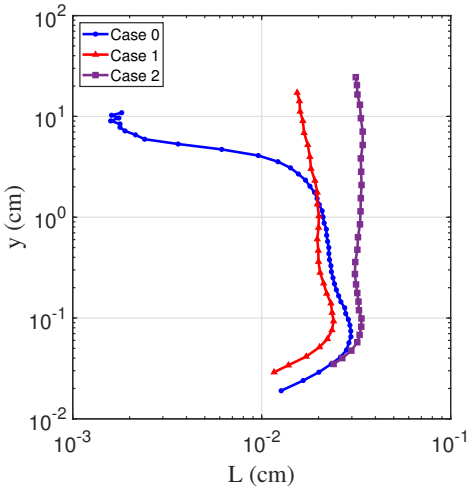

(d) at 1000 Hz

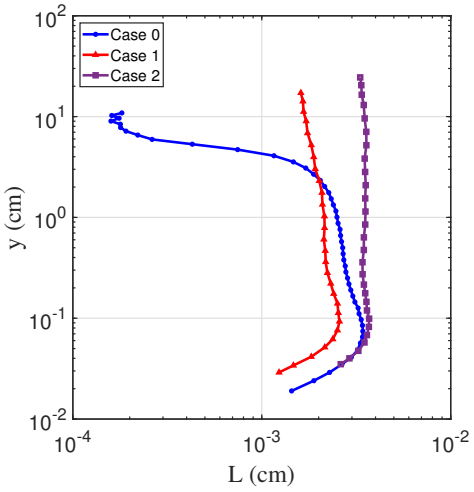

(e) at 10000 Hz

Figure 5.10: Comparison of the size variation of eddies of all cases at different frequencies along the boundary layer; (from raw data of Dogan et al. [27])

Finally, there are Tables B.1 to B.12 at Appendix B from the results obtained from the data of Dogan et al. These tables are specific to each of the selected points. Each table first contains the mean velocity, $\overline{U}$, rms of velocity fluctuations, u', actual and calculated turbulent intensities, I_{act} and I_{calc}, and determined number n of the measured point. Also, the probability at $x = 0$ obtained by Eqn. 2.33, $P(1)$, determined number B from frequency-fluctuation velocity relation in Eqn. 2.58 and PDF constant A calculated using Eqn. 2.39 are added to these tables. Other results are given with their corresponding frequencies. The non-dimensional kinetic energy contribution of the selected frequency interval, ΔG, a value out of one is shown. Next columns consists of the non-dimensional fluctuation velocities, x, wavenumbers, k, wavelengths, L, probabilities of positive and negative fluctuations, $P_R(x)$ and $P_L(x)$ of chosen frequencies.

5.3 Results of Boundary Layer Data of Abdulrahim et al.

In this section, the analysis results of two cases of the atmospheric boundary layer data of Abdulrahim et al. are shown.

5.3.1 Velocity Profiles and Measurement Points of Cases of Abdulrahim et al.

The chosen points are decided in the same way as those of Dogan et al. data. However, in these velocity profiles, the measurement point closest to the wall has a higher percentage of their freestream mean velocity than those of Dogan et al.'s cases. Therefore, the points are not precisely at the same nondimensional location in the velocity profile as in previous cases.

While Case 4 consists of atmospheric boundary layer measurements generated by spires in the wind tunnel, Case 3 is the empty test section version of the same conditions without spires, as mentioned in Chapter 4. Similar to those of Dogan et al.'s cases in Tables 5.1 to 5.3, some information about chosen points is given in Table 5.8 and 5.9 for Case 3 and 4, respectively. Also, selected points are shown on their velocity profiles in Fig. 5.11.

Table 5.8: Information about measurement points of Abdulrahim et al.-Case 3 (from raw data of Abdulrahim et al. [1])

Point	y [cm]	U_m [m/s]	u' [cm/s]	I_{act} [%]	I_{calc} [%]	n [-]
Point 3A	0.20	7.17	94.6	13.2	13.2	8.39
Point 3B	4.00	9.56	66.6	6.97	6.97	17.0
Point 3C	20.0	11.0	6.11	0.55	0.55	230
Point 3D	50.0	10.9	5.69	0.52	0.52	245

Table 5.9: Information about measurement points of Abdulrahim et al.-Case 4 (from raw data of Abdulrahim et al. [1])

Point	y [cm]	U_m [m/s]	u' [cm/s]	I_{act} [%]	I_{calc} [%]	n [-]
Point 4A	0.20	6.78	94.0	13.9	13.9	7.93
Point 4B	4.00	8.42	80.7	9.59	9.59	12.0
Point 4C	20.0	9.67	68.1	7.11	7.11	16.6
Point 4D	50.0	10.9	23.1	2.11	2.11	59.4

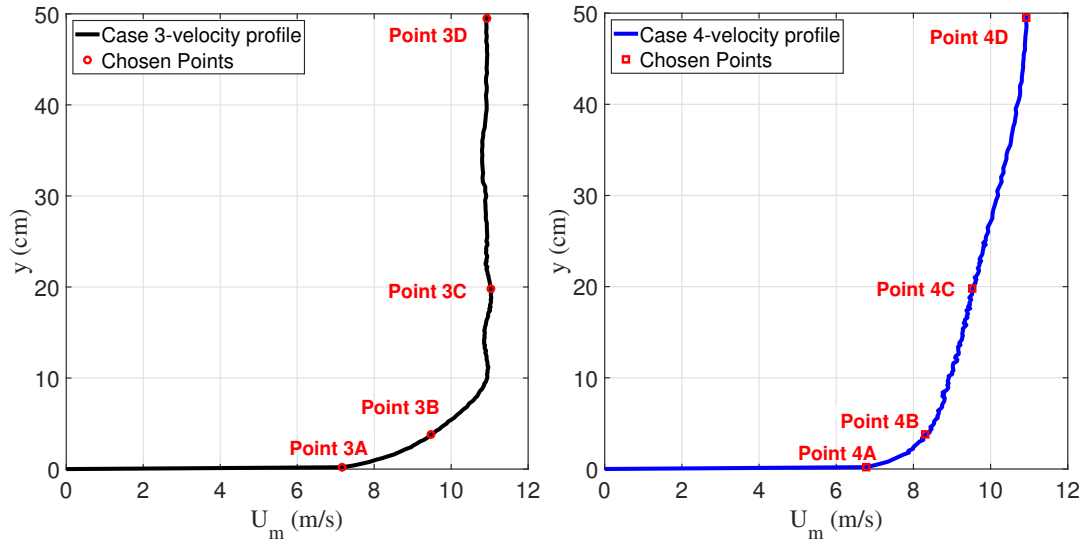

(a) Velocity profile and measurement points of Case 3 (b) Velocity profile and measurement points of Case 4

Figure 5.11: Velocity profiles generated by Abdulrahim et al.'s row data and measurement points (from raw data of Abdulrahim et al. [1])

5.3.2 PDFs of Measurement Points of Cases of Abdulrahim et al.

In this section, the compatibility of histograms and scaled PDFs of Case 3 and 4 is examined. Also, the variation of the PDF is discussed.

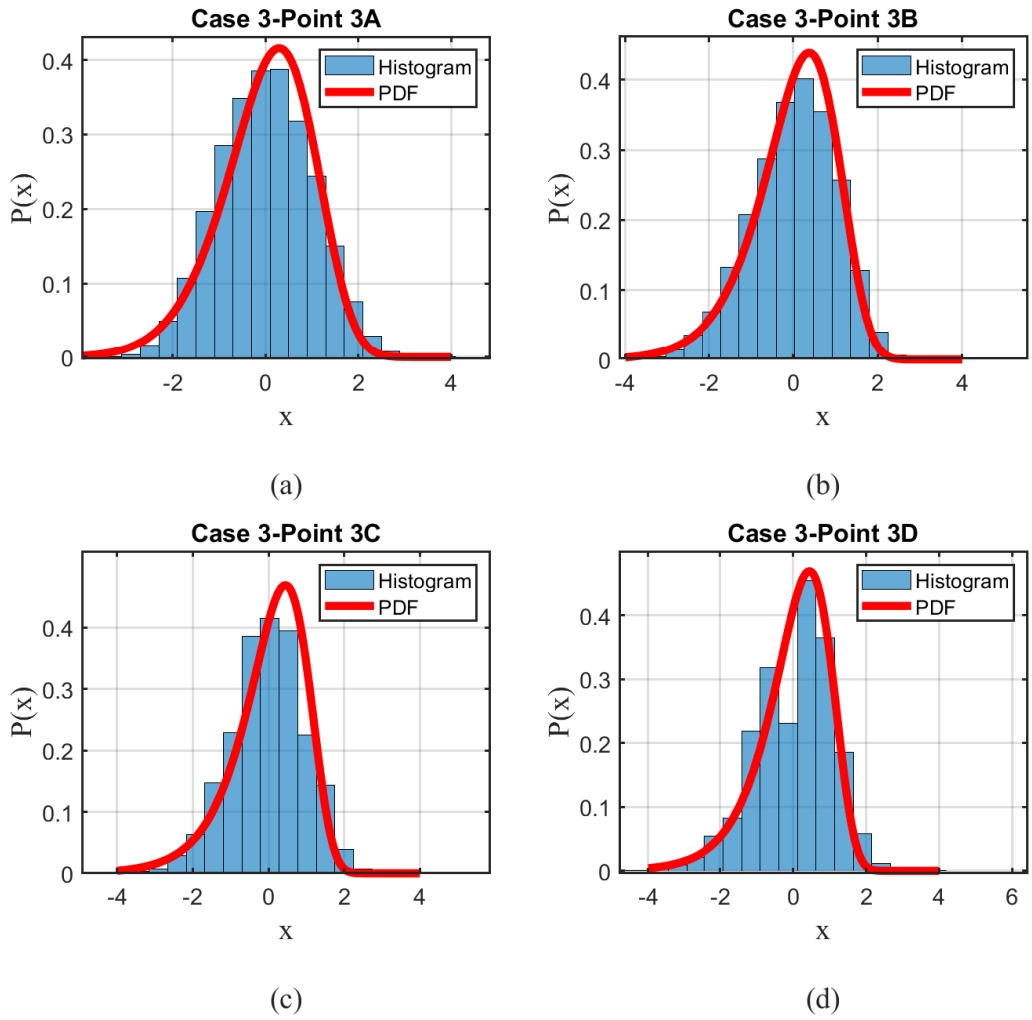

Figure 5.12: Histogram vs PDF of measurement points of Case 3 (from raw data of Abdulrahim et al. [1])

First of all, the histograms of the selected points are examined. Then, the general behavior of the distributions of Case 3 and 4 is found similar to those of Dogan et al.'s cases. However, when this general distribution is analyzed closely, the irregularities become noticeable. The reason for this may be related to the difference in sampling

rates and durations of experiments. Cases of Abdulrahim et al. are measured at a lower sampling rate and in a shorter time. Therefore, histograms of Abdulrahim et al.'s cases are less fulfilled.

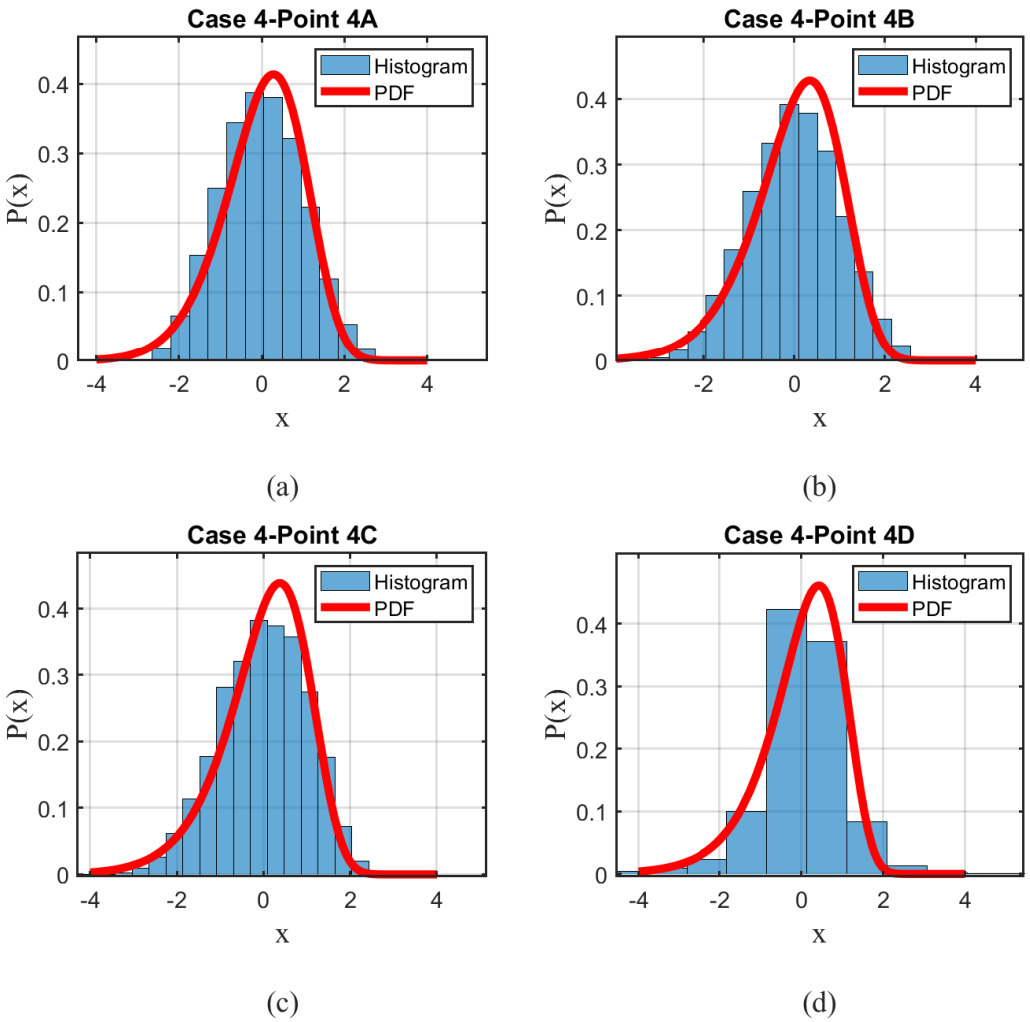

Figure 5.13: Histogram vs PDF of measurement points of Case 4 (from raw data of Abdulrahim et al. [1])

The width of histograms of Case 3 and 4 is larger at closer points to the wall, as shown in Fig. 5.12 and 5.13. From A points to D points, they become narrower and more right-skewed. Again, the compatibility of PDFs and histograms changes from A points to D points. The gap in negative fluctuation velocities becomes more significant at C and D points than at A and B points. It is seen that this inconsistency is more for Case 4 than for Case 3. But, it is still possible to interpret that the PDFs

accurately represent the distributions of fluctuation velocities for all points of the two cases. In addition, the histogram of Point 4D is generated at wider intervals, as the data becomes discrete when the same intervals as other points are taken.

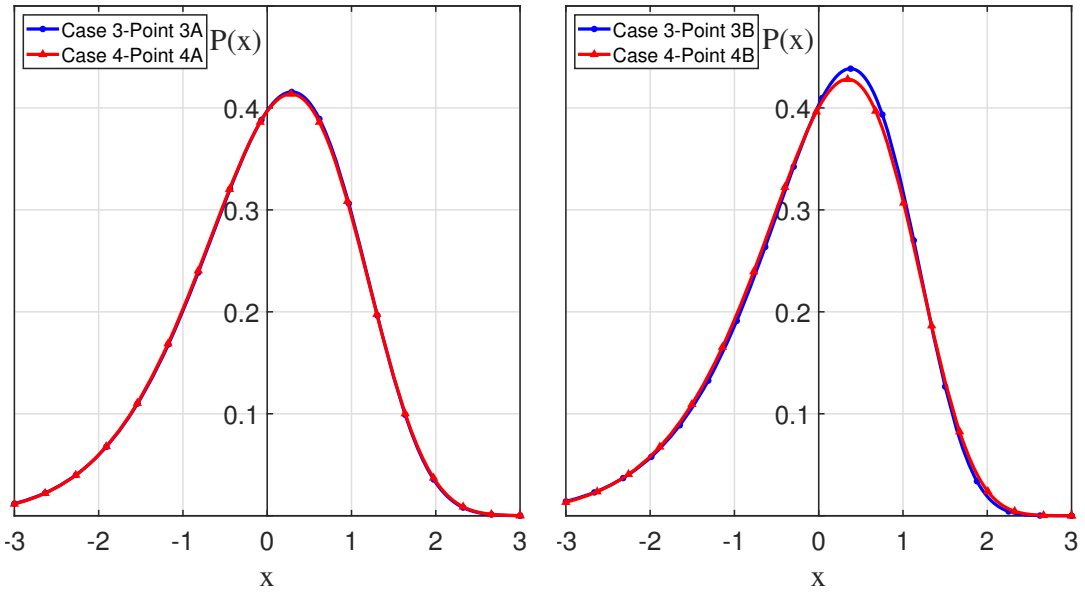

(a) A points

(b) B points

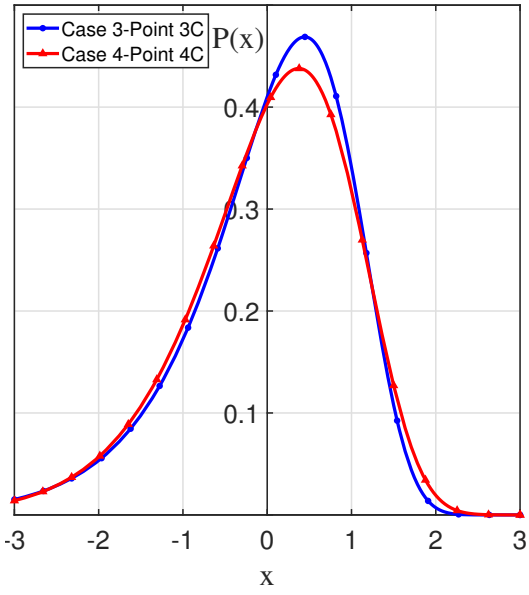

(c) C points

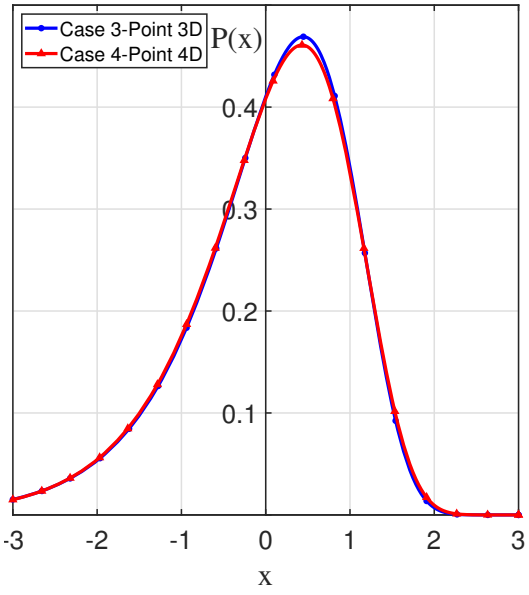

(d) D points

Figure 5.14: PDFs of measurement points (from raw data of Abdulrahim et al. [1])

In Fig. 5.14, the PDFs of similar points are compared. A points have almost the

same turbulence intensity levels. So, their n numbers are close, and PDFs are almost identical as in Fig. 5.14a. The gap becomes more significant when the difference is more apparent on n numbers, as seen in Fig. 5.14b and 5.14c. Although, the number n is so different in D points; PDFs look similar in Fig. 5.14d. When the number n increases too much, its effect on the change of the PDF decreases. So, although the n difference is substantial for the D points, the PDF curves are pretty close to each other. It is also seen that as the intensity decreases, the peak point of the curve rises, and the curve becomes more right-skewed than higher intensity points.

5.3.3 Energy Spectrums in Frequency Domain of Measurement Points of Cases of Abdulrahim et al.

For Case 3 and 4, the maximum frequency in the energy spectrum is found 5 kHz due to a sampling rate of 10 kHz. At higher frequencies than 200 Hz, the energy contribution is so small. Therefore, the range of spectrums in the frequency domain is limited to approximately 0-200 Hz, as shown in Fig. 5.15. The area under this curve is non-dimensional energy contribution, ΔG, and shown for selected frequency intervals in Tables Tables C.1 to C.8 at Appendix C.

In the same way as Doğan et al.'s cases, the energy is concentrated between 0-200 Hz. Around 200 Hz, the curves get pretty close to zero. Therefore, large and energetic eddies can be considered to be in this frequency range.

The frequency-dependent energy spectrums of similar points of Case 3 and 4 are also given in Fig. 5.15. When the A points are examined, it is seen that the energy contribution of Case 4 is quite intense at very low frequencies. Case 4 has spires for the creation of the atmospheric boundary layer. Therefore, the largest eddies contain more energy than those of Case 3. This is valid for points A, B, and C, as seen from Fig. 5.15a, 5.15b and 5.15c. The situation differs only at D points in Fig. 5.15d. The experiments of Case 3 are performed in the empty test section. The energy contribution of its large eddies at the freestream point is considerably higher than in Case 4. This result is similar in comparison to Dogan et al.'s D points. In the canonical case, Case 0, energy is accumulated at very small frequencies, as observed in Fig. 5.6d.

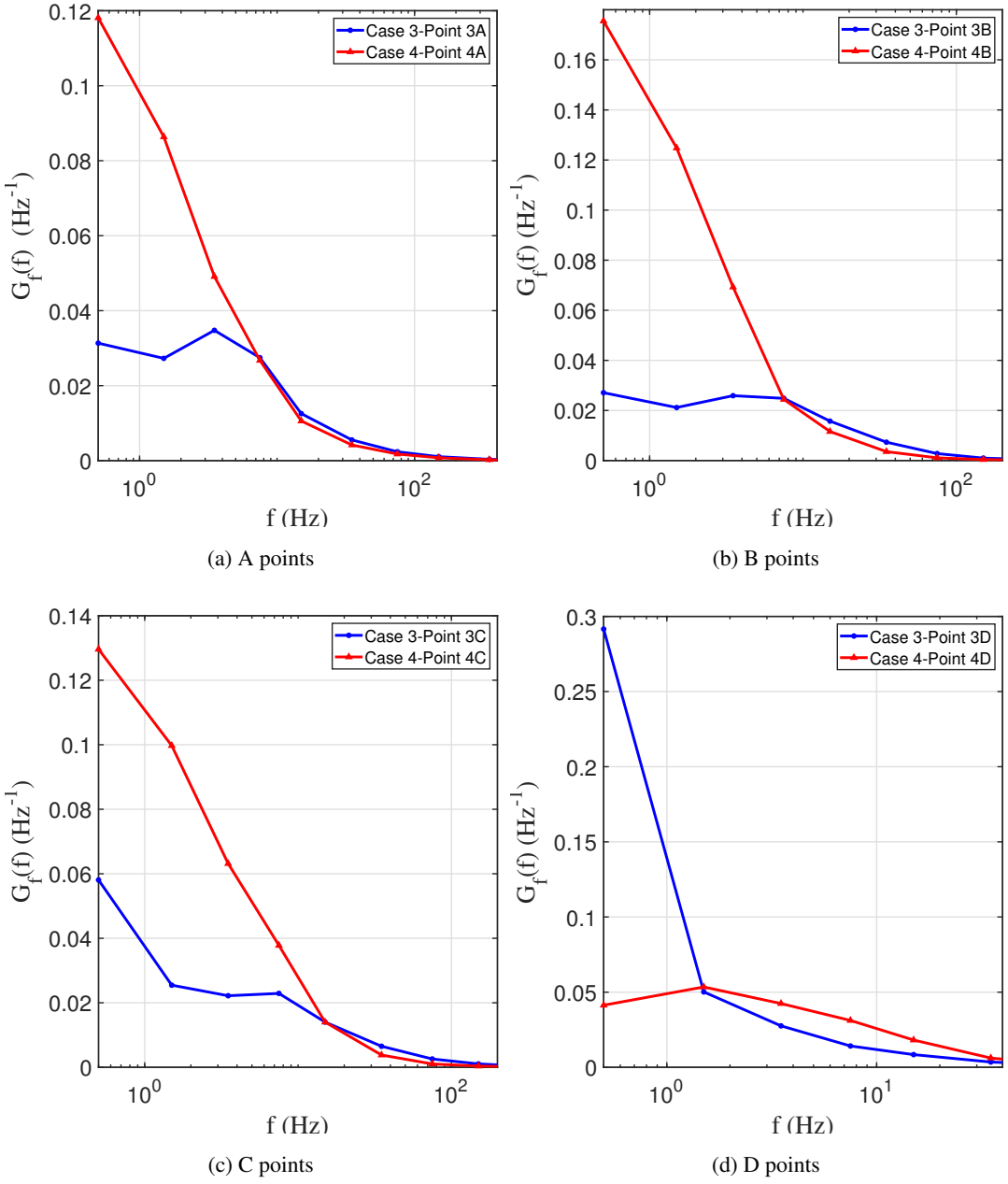

(a) A points

(b) B points

(c) C points

(d) D points

Figure 5.15: The energy spectra in the frequency domain of measurement points (from raw data of Abdulrahim et al. [1])

5.3.4 Energy Spectrums in Wavenumber Domain of Measurement Points of Cases of Abdulrahim et al.

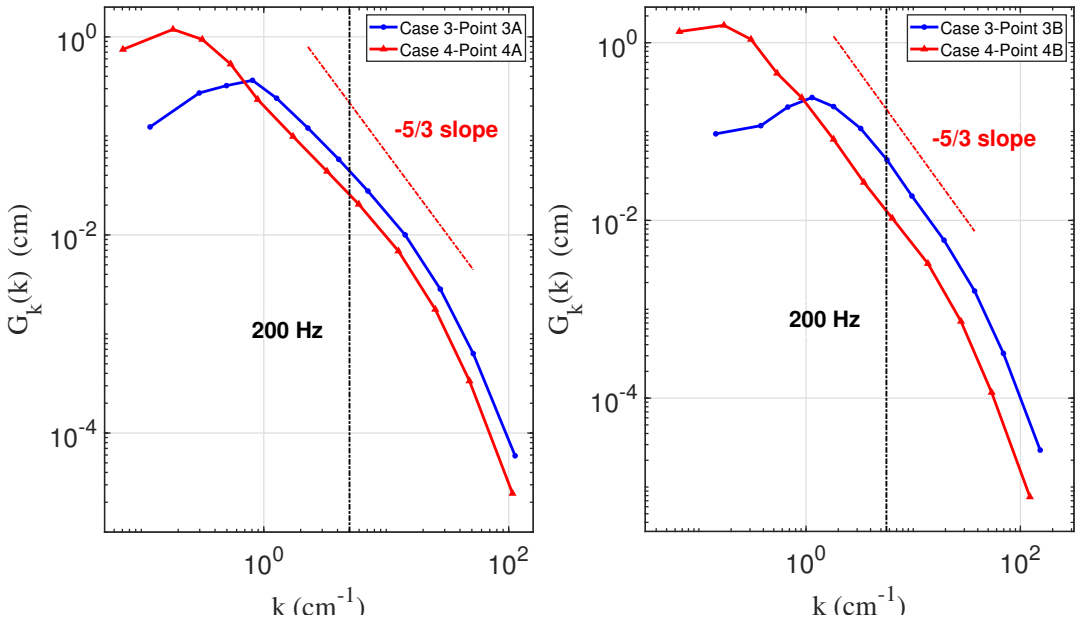

(a) A points

(b) B points

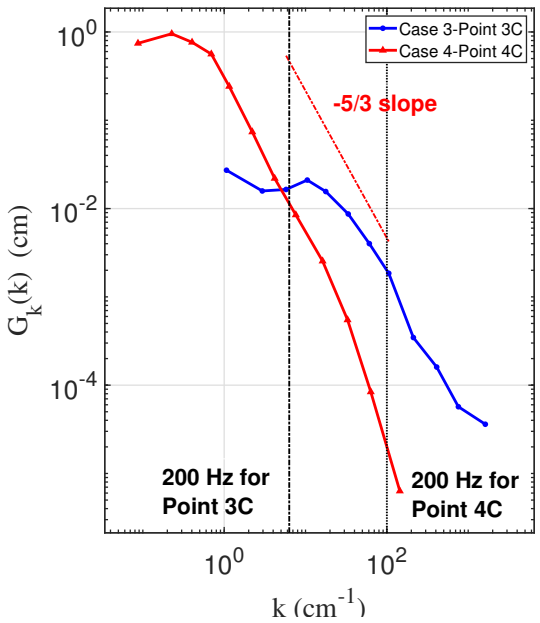

(c) C points

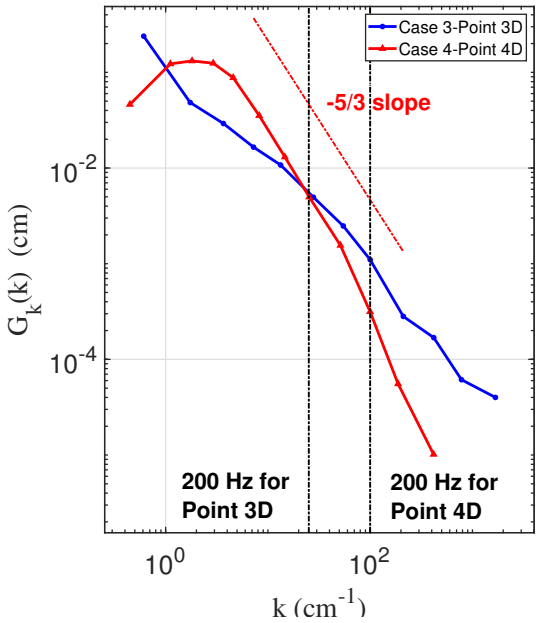

(d) D points

Figure 5.16: The wavenumber-dependent energy spectra of measurement points (red dashed line: $-5/3$ slope, black dashed line: approximately 200 Hz for specified cases) (from raw data of Abdulrahim et al. [1])

Fig. 5.16 shows the wavenumber-dependent energy spectrum of each selected point. In the same way as the previous figures, similar points are formed together so that they can be compared.

Small wavenumbers correspond to large eddies. In these wavenumbers, the difference of flow conditions shows their characteristics, and energy spectrums curves behave differently. The energy density is higher at closer points to the wall for both cases. It decreases from A points to D points. The variation of large eddies part of the spectrum is different for Case 3. The turbulence intensity in Point 4D is very small, 0.52% as shown in Table 5.8. Therefore, the spectrum loses curvy part and becomes almost a straight line, as seen from Fig. 5.16d.

For all points, -5/3 slope in inertial subrange is obtained. This subrange is approximately observed between 50 and 500 Hz. In all points of previous cases and A and B points in these cases, the corresponding wavenumbers to 200 Hz are found close. But in C and D points, they are different. In these points of Case 3, the -5/3 slope ends at 200 Hz, as shown in Fig. 5.16c and 5.16d. After the inertial subrange, the range of dissipating eddies starts. However, the behavior of this range varies in Points 3C and 3D. Even so, these parts of their spectrum curves change with different slopes; dissipation happens quickly as other curves.

5.3.5 Sizes and Lifespans of Measurement Points of Cases of Abdulrahim et al.

The sizes and lifespans of eddies are the focus of this section. Firstly, the sizes and lifespans of the largest and smallest eddies are given in Tables Tables 5.10 to 5.13.

The sizes of the largest eddies do not exceed the physical boundaries of the flow domain for all cases. The sizes of the largest eddies are in the order of cm. They are found highest near the wall due to significant velocity gradients. They decrease away from the wall. Case 4 has larger eddies than Case 3 because it has an effective source for generating large eddies, that is, spires. In addition, the size of the smallest eddies is obtained in the order of a micrometer.

Table 5.10: The size and lifespan of the largest and smallest eddies of A points (from raw data of Abdulrahim et al. [1])

Measurement Point -	Size of the Largest Eddy (at 1 Hz)	Size of the Smallest Eddy (at 5x10^3 Hz)	Lifespan of the Largest Eddy (at 1 Hz)	Lifespan of the Smallest Eddy (at 5x10^3 Hz)
POINT 3A	4.998 cm	64.67 μm	0.108 s	30.54 μs
POINT 4A	7.859 cm	65.76 μm	0.109 s	31.00 μs

Table 5.11: The size and lifespan of the largest and smallest eddies of B points (from raw data of Abdulrahim et al. [1])

Measurement Point -	Size of the Largest Eddy (at 1 Hz)	Size of the Smallest Eddy (at 5x10^3 Hz)	Lifespan of the Largest Eddy (at 1 Hz)	Lifespan of the Smallest Eddy (at 5x10^3 Hz)
POINT 3B	3.476 cm	46.43 μm	0.112 s	30.64 μs
POINT 4B	7.596 cm	57.37 μm	0.108 s	31.37 μs

Table 5.12: The size and lifespan of the largest and smallest eddies of C points (from raw data of Abdulrahim et al. [1])

Measurement Point -	Size of the Largest Eddy (at 1 Hz)	Size of the Smallest Eddy (at 5x10^3 Hz)	Lifespan of the Largest Eddy (at 1 Hz)	Lifespan of the Smallest Eddy (at 5x10^3 Hz)
POINT 3C	0.468 cm	5.110 μm	0.128 s	28.80 μs
POINT 4C	5.738 cm	48.79 μm	0.108 s	31.35 μs

Lifespans of the largest eddies are found in the order of one-tenth of a second. This result is similar to those of Dogan et al.'s cases. The smallest eddies have a lifespan in the order of ten microseconds.

The variation of eddy sizes along the boundary layer is presented at different frequencies for two cases in Fig. 5.17. Since large eddies correspond to small frequencies, the curves change apparently at 1 Hz. By increasing frequency, the change decreases,

Table 5.13: The size and lifespan of the largest and smallest eddies of D points (from raw data of Abdulrahim et al. [1])

Measurement Point -	Size of the Largest Eddy (at 1 Hz)	Size of the Smallest Eddy (at 5x10^3 Hz)	Lifespan of the Largest Eddy (at 1 Hz)	Lifespan of the Smallest Eddy (at 5x10^3 Hz)
POINT 3D	0.819 cm	4.274 μm	0.141 s	28.66 μs
POINT 4D	1.118 cm	16.97 μm	0.091 s	30.85 μs

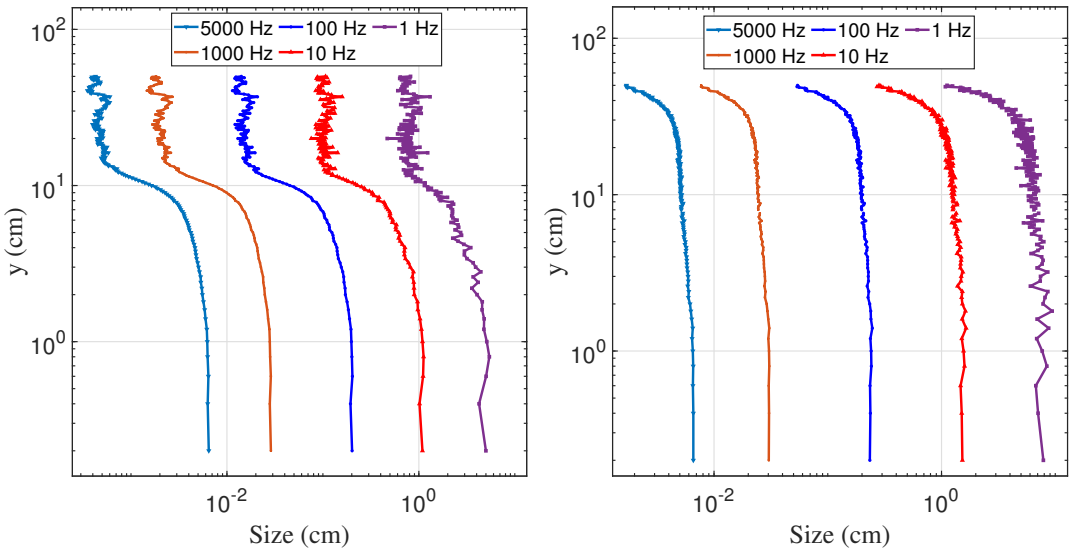

(a) Case 3

(b) Case 4

Figure 5.17: The size variation of eddies at different frequencies along the boundary layer (from raw data of Abdulrahim et al. [1])

and the curve becomes smoother than those of smaller frequencies. Considering the size curves of Case 3 and 4, it is possible to say that the curves of the same frequencies are at similar size levels. It can be observed that as the frequency decreases, the order difference increases. This observation is consistent with the physics of large eddies.

Size curves for Case 3 and 4 begin to behave differently as approaching freestream in Fig. 5.17. In Case 3, measured at the empty test section, the intensities reach

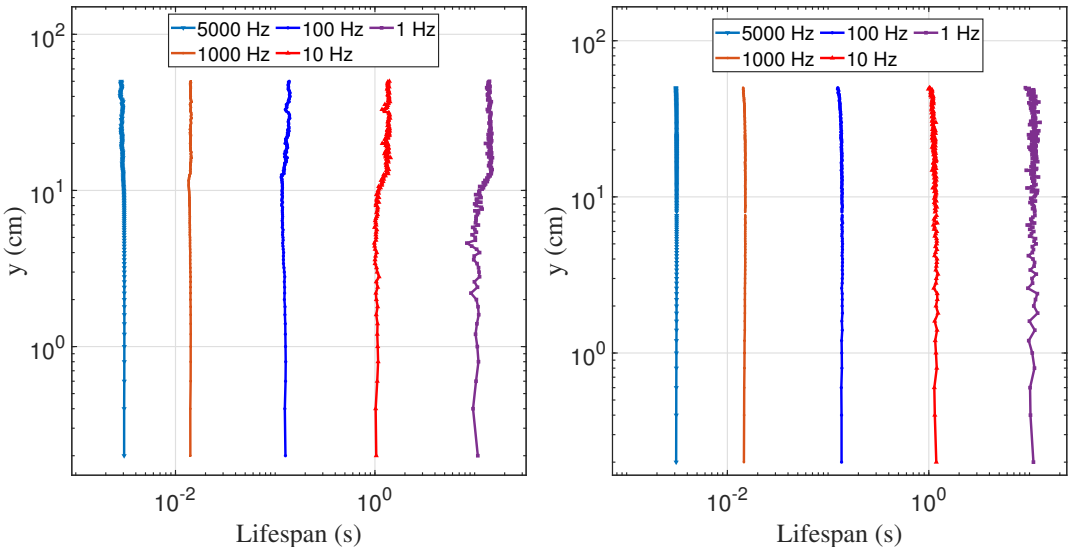

(a) Case 3

(b) Case 4

Figure 5.18: The size variation of eddies at different frequencies along the boundary layer (from raw data of Abdulrahim et al. [1])

very low values at lower y-locations than Case 4. Therefore, the size of the eddies decreases in these parts and continues in this way. In Case 4, the situation is different. Intensities are higher than in Case 3. So, a tendency to decreasing is observed towards freestream. The different behavior that occurs depending on the character of the flow in the size curves in the freestream region is also noticeable in Dogan et al.'s cases. However, there is a curved part near the wall in these curves, as shown in Fig. 5.8. This part is not observed in the results of Abdulrahim et al. Since measurements are not performed at locations very close to the wall in their case, comparing with Dogan et al.'s cases. It is estimated that the size curves of the eddies of Abdulrahim et al.'s cases near the wall are curved like those of Dogan et al. Because the parts of the curves up to the freestream are similar.

Lifespan variation along with the boundary layer for both cases is shown in Fig. 5.18. Like the size graphs, the change in the curves is more apparent for lower frequencies. With increasing frequency, curves become smoother. The order of lifespans is similar at the same frequency for both cases. In addition, the difference at the freestream region is observed. For Case 3, the lifespans of those regions decrease. This fall is more noticeable for large eddies than smaller ones.

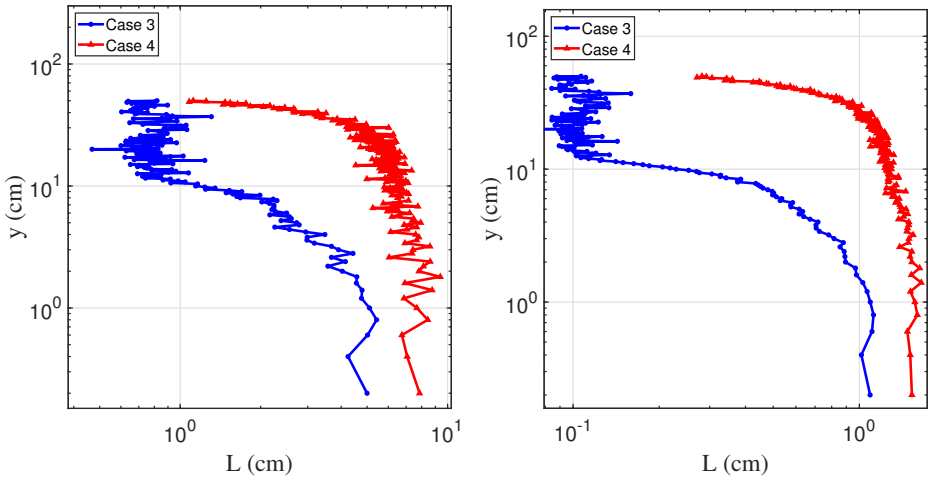

(a) at 1 Hz

(b) at 10 Hz

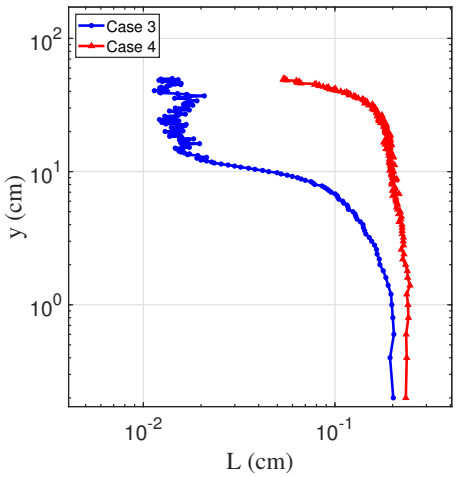

(c) at 100 Hz

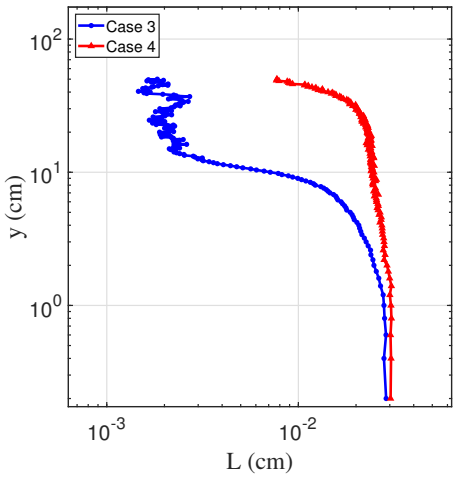

(d) at 1000 Hz

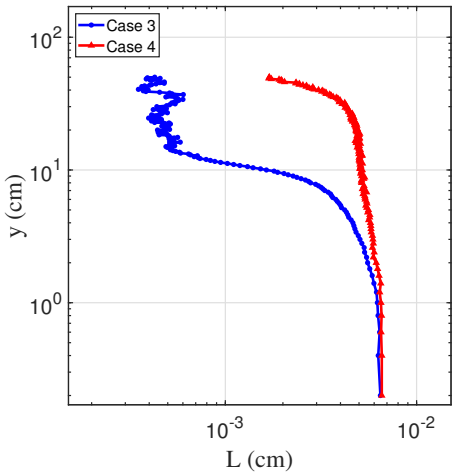

(e) at 5000 Hz

Figure 5.19: Comparison of the size variation of eddies of cases at different frequencies along the boundary layer (from raw data of Abdulrahim et al. [1])

For a clear comparison, eddy sizes of two cases are plotted depending on y-location at some frequencies in Fig. 5.19 The variation of sizes at low frequencies is quite evident. It is clearer from this figure that curves become smoother as the frequency increases. Additionally, closer to the freestream, the differentiation of sizes for these cases is observed clearly.

Furthermore, the results of chosen points of Abdulrahim et al. are included in Tables C.1 to C.8 at Appendix C.

CHAPTER 6

CONCLUSIONS

Today, turbulent flow problems are generally solved using turbulence models to find Reynolds stress terms in RANS equations. There is no single model that can be applied to every turbulent flow problem, and several models are used for similar flow cases by correcting some constants. This correction is needed because turbulence physics, especially large eddies, which are heavily influenced by initial and boundary conditions, are not sufficiently known. In this way, the lack of knowledge is tried to be eliminated. Therefore, knowledge about eddies such as energy contents, sizes, and lifespans is required for improving turbulent flow solutions.

In turbulent flow studies, the wavenumber is associated with the eddy sizes. The definition of wavenumber based on Taylor's frozen turbulence hypothesis is frequently used in literature. However, many studies find out the circumstances that this hypothesis is not applicable. These circumstances may be exampled with the cases with high turbulent intensity or where it is not appropriate to use a single convective velocity such as wall-bounded flows or applied to a large-scale turbulent structure. The reason is that only mean velocity is considered in this approach. The physical conditions such as flow type, dimension or region, and spectral information of the flow are not included in this calculation. It gives the same result for all flows with the same mean velocity. This approach is not a proper understanding of the physics of turbulence. Therefore, an alternative approach is required.

Çıray proposed QBT as an alternative method to Taylor's hypothesis in 1980 [69]. In his dispersion relation, fluctuation velocity is defined as energy transport velocity (group velocity) of discrete material package [70]. The definition is based on the quantum theory approach that the group velocity of the wave packet is the same as

the translational velocity of the particle. In addition, this theory is defined for 1-D flow and incompressible fluid [71].

In the present study, the QBT approach is implemented to a Matlab code. In order to calculate wavenumbers with the QBT approach, the frequency-dependent energy distribution of the flow is needed. This distribution is obtained by the spectral approach. In the generated code, FFT is applied using the function of Matlab. After the spectral approach, the code is generated by following the mathematical procedure of QBT. Implementation of method is tested and verified using the data of test cases published in 1980 [69]. After completing the code, different turbulent flow cases are analyzed using it.

Firstly, the three cases of Dogan et al.'s boundary layer data are analyzed. These cases can be classified with the usage and types of the active grid as no active grid (Case 0), cut-out wings (Case 1), and solid wings (Case 2) [27]. In their experiments, the instantaneous velocities are measured using hotwires at different points on the boundary layer and a fixed point on the freestream. For each case, the analysis results of the freestream points and the farthest points from the wall in the boundary layer (Points D) are compared, and no difference is observed. Therefore, the results of Points D are considered sufficient to obtain information about freestream. Then, four points for each profile are chosen considering critical regions on the profile and paying attention to similar regions for all cases. The PDFs of the selected points are discussed. In these PDFs, it is observed that higher fluctuation velocities are related to higher wavenumbers, and at some point, fluctuation velocity becomes a fixed value. It means that the probability of the existence of these high frequencies and high amplitude is very low. In addition, PDF and distribution of experimental data are compared. For A points, both are very compatible for three cases. However, for other points, some inconsistency is noticed. The reason may be that the flow did not reach a fully developed condition yet; that is, it did not lose its unsteady character. Therefore, it may be useful to repeat and compare experiments on a section further away from the measurement section. Another solution may be to choose different PDFs for boundary layer flows to represent data more accurately. However, the selected PDF is considered to adequately represent the experimental data.

The energy spectrum in the frequency domain obtained by the spectral approach is analyzed. For all points of all cases, 90-95% of kinetic energy contribution exists in the frequency interval from 0 to 200 Hz. After 200 Hz, energy contribution decreases, and at high frequencies, it reaches almost zero. Then, the wavenumber-dependent energy spectrum for each chosen point is discussed. Entire regions of this spectrum can be obtained by using QBT, especially regions of large eddies. The slope of -5/3 in the inertial subrange is observed in the spectrums of all points, as can be seen in Figs. 5.7 and 5.16. This slope is proof that the obtained spectrums are quite compatible with the literature. In dissipating eddies, the slope changes, and energy dissipates very quickly conforming to previous related studies.

The sizes and lifespans of eddies are included. As a result, it is observed that the largest wavelengths do not exceed the boundaries of the physical domain. That conforms with the physics of the flow. Except for Case 2, the largest eddies are found near the wall due to more significant velocity gradients. In Case 2, there is a strong source for turbulence generation. Therefore, the largest eddies are obtained in freestream. But sizes of eddies are still found to be quite large near the wall. It should be pointed out that sizes of the largest eddies are found to be quite close with the mesh size of the active grids as 8.1 cm, in Case 2. For Case 0 and 1, these sizes are smaller than those in Case 2, as the source of turbulence generation is less effective in Case 0 and 1. But sizes are still comparable with mesh size. The smallest eddies have sizes in the order of ten micrometers. Also, the lifespans of the largest eddies are in the order of 0.11 seconds. Those of the smallest eddies are found in the order of 16 microseconds. All mentioned results are included in this study in Tables B.1 to B.12 at Appendix B.

Secondly, two cases of atmospheric boundary layer data of Abdulrahim et al. are examined. The instantaneous velocities are measured at the empty test section (Case 3) and test section with spires (Case 4). The points are chosen at the same heights for both cases. The PDF and histogram of each point are found quite compatible. But their unconformity is observed in negative velocity fluctuations for all points. Therefore, choosing a PDF with a fuller left side may provide almost perfect compatibility for two cases.

In the frequency-dependent energy spectrum of these points, the energy is accumu-

lated between 0 and 200 Hz. Case 4 has a higher energy contribution in large eddies for points A, B, and C; it is smaller for points D. This behavior is similar to Dogan et al.'s cases. The reference case has a significant energy contribution at freestream for very small frequencies.

The spectrums in the wavenumber domain are also shown in the results. In the large eddies region, flow-dependent behavior is observed. -5/3 slope is consistently found in the inertial subrange. After this region, dissipating eddies occur with a rapid dissipation at high wavenumbers.

The sizes and lifespans of eddies are also added. The largest eddies are found with size in centimeter order and lifespan in one-tenth of a second. The smallest eddies are in the microlevel of these orders. On a logarithmic scale, the sizes and lifespans for different frequencies are discussed. The difference in flow conditions is noticed in the freestream region. But in the previous regions, behavior is found similar. The curvy parts near the wall of size plots of Dogan et al.'s cases do not exist in Abdulrahim et al.'s cases. Because the measurements of this region are not included in their data. Also, the irregularity of size and lifespan curves at low frequencies and becoming smoother at higher frequencies are consistent with the physics of eddies.

To sum up, this study tries to obtain information about eddies using spectral analysis and QBT for different flow conditions. The frequency-dependent energy spectrum is obtained in accordance with the work of Gabry et al. [29]. Experimental data are represented quite accurately by PDF defined in QBT and included in the calculations. The energy spectrum in the wavenumber domain is consistent with the spectrums of different experiments given in Fig. 1.2 and the physics of turbulence. But eddy sizes are smaller than those calculated by some of the integral scale definitions and Taylor's microscale and Kolmogorov scale calculated based on Taylor's hypothesis, as can be seen in Dogan et al.'s study [27]. However, the obtained sizes are consistent with the definition of Roach [76], as shown in Gabry et al.'s NASA report [29]. With the results mentioned, this study aims to understand turbulent flow problems in a more appropriate way to physics.

REFERENCES

[1] A. Abdulrahim, M. T. Akpolat, A. Hassanein, M. Perçin, and O. Uzol. Effects of inflow boundary layer on the wake of a radially non-uniform porous disk. *Journal of Renewable and Sustainable Energy*, 13(3):033302, 2021.

[2] M. Abramowitz. *Handbook of Mathematical Functions, edited by M. Abramowitz and I. Stegun*. Dover Publications, New York, 1964.

[3] R. Antonia, A. Chambers, C. Friehe, and C. Van Atta. Temperature ramps in the atmospheric surface layer. *Journal of Atmospheric Sciences*, 36(1):99–108, 1979.

[4] R. Antonia, J. Kim, and L. Browne. Some characteristics of small-scale turbulence in a turbulent duct flow. *Journal of Fluid Mechanics*, 233:369–388, 1991.

[5] W. Baars, N. Hutchins, and I. Marusic. Reynolds number trend of hierarchies and scale interactions in turbulent boundary layers. *Philosophical Transactions of the Royal Society A: Mathematical, Physical and Engineering Sciences*, 375(2089):20160077, 2017.

[6] L. V. Baldwin and T. J. Walsh. Turbulent diffusion in the core of fully developed pipe flow. *AIChE Journal*, 7(1):53–61, 1961.

[7] R. Batt. Turbulent mixing of passive and chemically reacting species in a low-speed shear layer. *Journal of Fluid Mechanics*, 82(1):53–95, 1977.

[8] R. Blackwelder. On the role of phase information in conditional sampling. *The Physics of Fluids*, 20(10):S232–S242, 1977.

[9] J. Boussinesq. Theory del'eroulement tourbi llant. *Mem. Pre Par. Div. Sav. XXI, Paris*, 1877.

[10] P. Bradshaw, D. Ferriss, and N. Atwell. Calculation of boundary-layer development using the turbulent energy equation. *Journal of Fluid Mechanics*, 28(3):593–616, 1967.

[11] H. Bruun. A time-domain analysis of the large-scale flow structure in a circular jet. part 1. moderate reynolds number. *Journal of fluid Mechanics*, 83(4):641–671, 1977.

[12] M. Bull. Wall-pressure fluctuations associated with subsonic turbulent boundary layer flow. *Journal of Fluid Mechanics*, 28(4):719–754, 1967.

[13] F. Champagne, V. Harris, and S. Corrsin. Experiments on nearly homogeneous turbulent shear flow. *Journal of Fluid Mechanics*, 41(1):81–139, 1970.

[14] R. Chanaud and R. Hayden. Edge noise caused by two turbulent wall jets. *The Journal of the Acoustical Society of America*, 48(1A):125–125, 1970.

[15] H. Choi and P. Moin. Grid-point requirements for large eddy simulation: Chapman's estimates revisited. *Physics of fluids*, 24(1):011702, 2012.

[16] C. Çıray. *Akışkanlar mekaniğine giriş: muhendislik yaklaşımı: turbulans ve bazı turbulanslı akımlar uçuncu kitap*. ODTU Yayıncılık, 2013.

[17] M. Coantic and A. Favre. Activities in, and preliminary results of, air-sea interactions research at imst. In *Advances in Geophysics*, volume 18, pages 391–405. Elsevier, 1975.

[18] G. Comte-Bellot and S. Corrsin. Simple eulerian time correlation of full-and narrow-band velocity signals in grid-generated,'isotropic'turbulence. *Journal of fluid mechanics*, 48(2):273–337, 1971.

[19] J. W. Cooley and J. W. Tukey. An algorithm for the machine calculation of complex fourier series. *Mathematics of computation*, 19(90):297–301, 1965.

[20] G. Corcos. *Pressure fluctuations in shear flows*. University of California, Institute of Engineering Research, 1962.

[21] P. Davies, M. Fisher, and M. Barratt. The characteristics of the turbulence in the mixing region of a round jet. *Journal of Fluid Mechanics*, 15(3):337–367, 1963.

[22] M. Davis. Intensity, scale and convection of turbulent density fluctuations. *Journal of Fluid Mechanics*, 70(3):463–479, 1975.

[23] S. Davoust and L. Jacquin. Taylor's hypothesis convection velocities from mass conservation equation. *Physics of Fluids*, 23(5):051701, 2011.

[24] R. de Kat and B. Ganapathisubramani. Frequency–wavenumber mapping in turbulent shear flows. *Journal of Fluid Mechanics*, 783:166–190, 2015.

[25] J. C. Del Álamo and J. Jiménez. Estimation of turbulent convection velocities and corrections to taylor's approximation. *Journal of Fluid Mechanics*, 640:5, 2009.

[26] A. Demetriades. Turbulence correlations in a compressible wake. *Journal of Fluid Mechanics*, 74(2):251–267, 1976.

[27] E. Dogan, R. Hanson, and B. Ganapathisubramani. Interactions of large-scale free-stream turbulence with turbulent boundary layers. *Journal of Fluid Mechanics*, pages 1–29, 2016.

[28] A. Dróżdż and W. Elsner. Amplitude modulation and its relation to streamwise convection velocity. *International Journal of Heat and Fluid Flow*, 63:67–74, 2017.

[29] L. A. El-Gabry, D. R. Thurman, and P. E. Poinsatte. *Procedure for determining turbulence length scales using hotwire anemometry*. National Aeronautics and Space Administration, Glenn Research Center, 2014.

[30] A. Favre. Review on space-time correlations in turbulent fluids. 1965.

[31] A. Favre, J. Gaviglio, and R. Dumas. Structure of velocity space-time correlations in a boundary layer. *The Physics of Fluids*, 10(9):S138–S145, 1967.

[32] M. Fisher and P. Davies. Correlation measurements in a non-frozen pattern of turbulence. *Journal of fluid mechanics*, 18(1):97–116, 1964.

[33] F. N. Frenkiel and P. S. Klebanoff. Space-time correlations in turbulence. *Dynamics of fluids and plasmas*, page 257, 1966.

[34] B. Ganapathisubramani, K. Lakshminarasimhan, and N. Clemens. Determination of complete velocity gradient tensor by using cinematographic stereoscopic piv in a turbulent jet. *Experiments in fluids*, 42(6):923–939, 2007.

[35] C. Geng, G. He, Y. Wang, C. Xu, A. Lozano-Durán, and J. M. Wallace. Taylor's hypothesis in turbulent channel flow considered using a transport equation analysis. *Physics of Fluids*, 27(2):025111, 2015.

[36] M. Gibson. Spectra of turbulence in a round jet. *Journal of Fluid Mechanics*, 15(2):161–173, 1963.

[37] V. Goldschmidt, M. Young, and E. Ott. Turbulent convective velocities (broadband and wavenumber dependent) in a plane jet. *Journal of Fluid Mechanics*, 105:327–345, 1981.

[38] H. Grant, R. Stewart, and A. Moilliet. Turbulence spectra from a tidal channel. *Journal of Fluid Mechanics*, 12(2):241–268, 1962.

[39] G.-W. He and J.-B. Zhang. Elliptic model for space-time correlations in turbulent shear flows. *Physical Review E*, 73(5):055303, 2006.

[40] T. Hedrick, R. Azad, and S. Banerjee. Phase velocities and angle of inclination for frequency components in fully developed turbulent flow through pipes. 1971.

[41] M. T. Heideman, D. H. Johnson, and C. S. Burrus. Gauss and the history of the fast fourier transform. *Archive for history of exact sciences*, 34(3):265–277, 1985.

[42] G. Heskestad. A generalized taylor hypothesis with application for high reynolds number turbulent shear flows. 1965.

[43] J. O. Hinze. *Turbulence: An Introduction to Its Mechanism and Theory*. McGraw-Hill series in mechanical engineering. McGraw-Hill, 1959.

[44] A. Kistler and T. Vrebalovich. Grid turbulence at large reynolds numbers. *Journal of Fluid Mechanics*, 26(1):37–47, 1966.

[45] N. Ko and P. Davies. The near field within the potential cone of subsonic cold jets. *Journal of Fluid Mechanics*, 50(1):49–78, 1971.

[46] A. N. Kolmogorov. The local structure of turbulence in incompressible viscous fluid for very large reynolds numbers. *Cr Acad. Sci. URSS*, 30:301–305, 1941.

[47] L. Kovasznay, V. Kibens, and R. Blackwelder. Large-scale motion in the intermittent region of a turbulent boundary layer. *Journal of Fluid Mechanics*, 41:283–325, 1970.

[48] L. Landau and E. Lifshitz. Fluid mechanics. pergamon press, oxford. *Section 92, problem*, 2, 1959.

[49] J. Lau and M. Fisher. The vortex-street structure of 'turbulent'jets. part 1. *Journal of Fluid Mechanics*, 67(2):299–337, 1975.

[50] J. Laufer. The structure of turbulence in fully developed pipe flow naca rep. 1174. 1954.

[51] S. Lee, S. K. Lele, and P. Moin. Simulation of spatially evolving turbulence and the applicability of taylor's hypothesis in compressible flow. *Physics of Fluids A: Fluid Dynamics*, 4(7):1521–1530, 1992.

[52] C.-C. Lin. On taylor's hypothesis and the acceleration terms in the navier-stokes equation. *Quarterly of Applied Mathematics*, 10(4):295–306, 1953.

[53] W. D. McComb. The physics of fluid turbulence. *Oxford*, 1990.

[54] P. McConachie. The distribution of convection velocities in turbulent pipe flow. *Journal of Fluid Mechanics*, 103:65–85, 1981.

[55] P. Moin. Revisiting taylor's hypothesis. *Journal of Fluid Mechanics*, 640:1–4, 2009.

[56] D. O. Mora and M. Obligado. Estimating the integral length scale on turbulent flows from the zero crossings of the longitudinal velocity fluctuation. *Experiments in fluids*, 61(9):1–10, 2020.

[57] L. Mydlarski and Z. Warhaft. On the onset of high-reynolds-number grid-generated wind tunnel turbulence. *Journal of Fluid Mechanics*, 320:331–368, 1996.

[58] F. T. Nieuwstadt, B. J. Boersma, and J. Westerweel. Statistical description of turbulence. In *Turbulence*, pages 75–85. Springer, 2016.

[59] L. J. Oswald and V. Kibens. *Turbulent flow in the wake of a disk*. 1971.

[60] U. Piomelli and E. Balaras. Wall-layer models for large-eddy simulations. *Annual review of fluid mechanics*, 34(1):349–374, 2002.

[61] L. B. M. Pires, I. B. d. Paula, G. Fisch, R. Gielow, and R. d. M. Girardi. Simulations of the atmospheric boundary layer in a wind tunnel with short test section. *Journal of Aerospace Technology and Management*, 5:305–314, 2013.

[62] S. B. Pope. *Turbulent flows*. IOP Publishing, 2001.

[63] D. C. Powell and C. Elderkin. An investigation of the application of taylor's hypothesis to atmospheric boundary layer turbulence. *Journal of Atmospheric Sciences*, 31(4):990–1002, 1974.

[64] L. Prandtl. 7. bericht über untersuchungen zur ausgebildeten turbulenz. *ZAMM-Journal of Applied Mathematics and Mechanics/Zeitschrift für Angewandte Mathematik und Mechanik*, 5(2):136–139, 1925.

[65] W. H. Press, B. P. Flannery, S. A. Teukolsky, and W. T. Vetterling. *Numerical Recipes in FORTRAN 77: Volume 1 of Fortran Numerical Recipes: The Art of Scientific Computing*. Cambridge University Press, 1992.

[66] E. Punskaya. *Digital Signal Processing (DSP) Lecture Notes- Chapter 3: Fast Fourier Transform*. Jan. 2009.

[67] S. Rajagopalan and R. Antonia. Interaction between large and small scale motions in a two-dimensional turbulent duct flow. *The Physics of Fluids*, 23(6):1101–1110, 1980.

[68] K. R. Rao, D. N. Kim, and J. J. Hwang. *Fast Fourier transform-algorithms and applications*. Springer Science & Business Media, 2011.

[69] C. Çıray. On wavenumber definition in turbulence. *Metu Journal of Pure and Applied Sciences*, 13(3):431–480, 1980.

[70] C. Çıray. Wavenumber in turbulence and its discrete nature. In *9th Ankara International Aerospace Conference*. METU, Sep. 2017.

[71] C. Çıray. Quantic behavior of turbulence. In *10th Ankara International Aerospace Conference*. METU, Sep. 2019.

[72] C. Çıray. Türbülansın bir problemi ve "türbülansın kuantik davranışı" yaklaşımı ile Çözümü. In *UHUK*, 2020.

[73] O. Reynolds. Xxix. an experimental investigation of the circumstances which determine whether the motion of water shall be direct or sinuous, and of the law of resistance in parallel channels. *Philosophical Transactions of the Royal society of London*, (174):935–982, 1883.

[74] O. Reynolds. Iv. on the dynamical theory of incompressible viscous fluids and the determination of the criterion. *Philosophical transactions of the royal society of london.(a.)*, (186):123–164, 1895.

[75] L. F. Richardson. Weather prediction by numerical process. *London (reprint: Dover, New York 1965)*, 1922.

[76] P. E. Roach. The generation of nearly isotropic turbulence by means of grids. *International Journal of Heat and Fluid Flow*, 8(2):82–92, 1987.

[77] S. Saddoughi and S. Veeravalli. Local isotropy in turbulent boundary layers at high reynolds number. *Journal of Fluid Mechanics*, 268:333–372, 1994.

[78] V. A. Sandborn and R. D. Marshall. *Local isotropy in wind tunnel turbulence: technical report*. PhD thesis, Colorado State University. Libraries, 1965.

[79] F. G. Schmitt. About boussinesq's turbulent viscosity hypothesis: historical remarks and a direct evaluation of its validity. *Comptes Rendus Mécanique*, 335(9-10):617–627, 2007.

[80] I. W. Selesnick and G. Schuller. *The transform and data compression handbook*, chapter The Discrete Fourier Transform, pages 37–39. Boca Raton, FL: CRC Press, 2001.

[81] P. Sepri. Two-point turbulence measurements downstream of a heated grid. *The Physics of Fluids*, 19(12):1876–1884, 1976.

[82] S. Tardu and P. Vezin. On the taylor hypothesis in forced unsteady wall flows. *Experiments in fluids*, 39(5):909–922, 2005.

[83] G. I. Taylor. I. eddy motion in the atmosphere. *Philosophical Transactions of the Royal Society of London. Series A, Containing Papers of a Mathematical or Physical Character*, 215(523-537):1–26, 1915.

[84] G. I. Taylor. The spectrum of turbulence. *Proceedings of the Royal Society of London. Series A-Mathematical and Physical Sciences*, 164(919):476–490, 1938.

[85] H. Tennekes. Eulerian and lagrangian time microscales in isotropic turbulence. *Journal of Fluid Mechanics*, 67(3):561–567, 1975.

[86] H. Tennekes and J. L. Lumley. *A first course in turbulence*. MIT press, 2018.

[87] H. W. Tieleman. *Viscous region of turbulent boundary layer: technical report*. PhD thesis, Colorado State University. Libraries, 1967.

[88] A. Trush, S. POSPÍŠIL, and H. KOZMAR. Comparison of turbulence integral length scale determination methods. *WIT Transactions on Engineering Sciences*, 128:113–123, 2020.

[89] M. S. Uberoi and P. Freymuth. Spectra of turbulence in wakes behind circular cylinders. *The Physics of Fluids*, 12(7):1359–1363, 1969.

[90] C. Walck. Hand-book on statistical distributions for experimentalists. *University of Stockholm*, 10:3–6, 2007.

[91] W. Willmarth and S.-T. Correlations. Spectra of wall-pressure in a turbulent boundary layer. *National Aeronautical and Space Administration, Washington, DC, NASA Memo No*, pages 3–17, 1959.

[92] W. W. Willmarth and C. E. Wooldridge. Measurments of the fluctuating pressure at the wall beneath a thick turbulent boundary layer. Technical report, 1962.

[93] J. Wills. On convection velocities in turbulent shear flows. *Journal of Fluid Mechanics*, 20(3):417–432, 1964.

[94] L. Wilson and R. Damkevala. Statistical properties of turbulent density fluctuations. *Journal of Fluid Mechanics*, 43(2):291–303, 1970.

[95] C. WOOLDRIDGE, D. WOOTEN, and A. AMARO. The structure of jet turbulence producing jet noise. In *10th Aerospace Sciences Meeting*, page 158, 1972.

[96] I. Wygnanski and H. Fiedler. Some measurements in the self-preserving jet. *Journal of Fluid Mechanics*, 38(3):577–612, 1969.

[97] I. Wygnanski and H. E. Fiedler. The two-dimensional mixing region. *Journal of Fluid Mechanics*, 41(2):327–361, 1970.

[98] X. Yang and M. Howland. Implication of taylor's hypothesis on measuring flow modulation. *Journal of Fluid Mechanics*, 836:222, 2018.

[99] K. Zaman and A. Hussain. Taylor hypothesis and large-scale coherent structures. *Journal of Fluid Mechanics*, 112:379–396, 1981.

[100] X. Zhao and G.-W. He. Space-time correlations of fluctuating velocities in turbulent shear flows. *Physical Review E*, 79(4):046316, 2009.

APPENDIX A

FOURIER TRANSFORMS

A.1 Discrete Fourier Transform

Suppose that N is the number of discrete data and U_η is the complex number that includes the Fourier coefficients, a real number a_η and a complex number b_η, defined as $U_\eta = a_\eta + b_\eta$. Then, Fourier coefficients can be shown as [80],

$$U_\eta = \sum_{t=0}^{N-1} u_t W_N^{\eta t} \ , \quad \eta = 0, 1, ..., N-1 \ , \tag{A.1}$$

where

$$f_\eta = \frac{\eta}{N\Delta}, \quad \eta = -\frac{N}{2}, ..., \frac{N}{2} \ , \tag{A.2}$$

$$W_N = e^{-2\pi i/N} = cos\left(\frac{2\pi}{N}\right) - isin\left(\frac{2\pi}{N}\right) \ . \tag{A.3}$$

All coefficients can be written in matrix form,

$$\begin{bmatrix} U_{\eta=0} \\ U_{\eta=1} \\ U_{\eta=2} \\ . \\ . \\ . \\ U_{\eta=N-1} \end{bmatrix} = \begin{bmatrix} 1 & 1 & 1 & ... & 1 \\ 1 & W_N^1 & W_N^2 & ... & W_N^{N-1} \\ 1 & W_N^2 & W_N^4 & ... & W_N^{2(N-1)} \\ . & . & . & ... & . \\ . & . & . & ... & . \\ . & . & . & ... & . \\ 1 & W_N^{N-1} & W_N^{2(N-1)} & ... & W_N^{(N-1)(N-1)} \end{bmatrix} . \begin{bmatrix} u_{t=0} \\ u_{t=1} \\ u_{t=2} \\ . \\ . \\ . \\ u_{t=N-1} \end{bmatrix} \ . \tag{A.4}$$

Also, it can be represented as:

$$U_\eta = F_N.u_t \ , \tag{A.5}$$

where F_N is the NxN DFT matrix that is called a Vandermonde matrix in linear algebra. Solving A.4 provides U_η matrix, and Fourier coefficients can be obtained. However, obtaining this solution by direct matrix multiplication requires $O(N^2)$ arithmetic operations as can be seen from,

$$N.N + N(N-1) = 2N^2 - N \equiv O(N^2) \ . \tag{A.6}$$

A.2 Fast Fourier Transform

Now, the FFT algorithm scheme will be explained [66]. The procedure starts with the DFT formula, which is Eqn. A.1. This equation is split into two parts for even and odd η values,

$$U_\eta = \sum_{t=0}^{\frac{N}{2}-1} u_{2t} W_N^{\eta(2t)} + \sum_{t=0}^{\frac{N}{2}-1} u_{2t+1} W_N^{\eta(2t+1)} \ . \tag{A.7}$$

Then, $W_N = e^{-2\pi i/N}$ is substituted into this equation,

$$U_\eta = \sum_{t=0}^{\frac{N}{2}-1} u_{2t} e^{-\frac{2\pi i}{N}\eta(2t)} + \sum_{t=0}^{\frac{N}{2}-1} u_{2t+1} e^{-\frac{2\pi i}{N}\eta(2t+1)} \ . \tag{A.8}$$

Second term can be written as,

$$U_\eta = \sum_{t=0}^{\frac{N}{2}-1} u_{2t} e^{-\frac{2\pi i}{N/2}\eta t} + e^{-\frac{2\pi i}{N}\eta} \sum_{t=0}^{\frac{N}{2}-1} u_{2t+1} e^{-\frac{2\pi i}{N/2}\eta t} \ . \tag{A.9}$$

Finally, it becomes,

$$U_\eta = A_\eta + W_N^\eta B_\eta \ , \tag{A.10}$$

where A_η and B_η are defined as:

$$A_\eta = \sum_{t=0}^{\frac{N}{2}-1} u_{2t} e^{-\frac{2\pi i}{N/2}\eta t} \,, \qquad \text{(A.11a)} \qquad B_\eta = \sum_{t=0}^{\frac{N}{2}-1} u_{2t+1} e^{-\frac{2\pi i}{N/2}\eta t} \,. \qquad \text{(A.11b)}$$

Here, A_η and B_η are also two different DFT's whose lengths are $N/2$. While A_η includes even η numbers of samples such as $u_{t=0}$, $u_{t=2}$,.., $u_{t=N-2}$, B_η involves odd η numbers of samples which are $u_{t=1}$, $u_{t=3}$,.., $u_{t=N-1}$. Again, DFT is periodic in the frequency domain. Therefore, $N/2$ is period.

Eqn. A.9 is arranged for $\eta + N/2$,

$$U_{\eta+\frac{N}{2}} = \sum_{t=0}^{\frac{N}{2}-1} u_{2t} e^{-\frac{2\pi i}{N/2}\left(\eta+\frac{N}{2}\right)t} + e^{-\frac{2\pi i}{N}\left(\eta+\frac{N}{2}\right)} \sum_{t=0}^{\frac{N}{2}-1} u_{2t+1} e^{-\frac{2\pi i}{N/2}\left(\eta+\frac{N}{2}\right)t} \,. \qquad \text{(A.12)}$$

Due to periodicity, it is possible to use the following relations,

$$e^{-\frac{2\pi i}{N/2}\left(\eta+\frac{N}{2}\right)t} = e^{-\frac{2\pi i}{N/2}\eta t} \,, \qquad \text{(A.13)} \qquad e^{-\frac{2\pi i}{N}\left(\eta+\frac{N}{2}\right)t} = -e^{-\frac{2\pi i}{N}\eta t} \,. \qquad \text{(A.14)}$$

Then, Eqn. A.12 becomes,

$$U_\eta = A_\eta - W_N^\eta B_\eta \,. \qquad \text{(A.15)}$$

Eqn. A.10 and Eq. A.15 can be represented in Fig. A.1. This scheme is called the butterfly structure of the FFT [68].

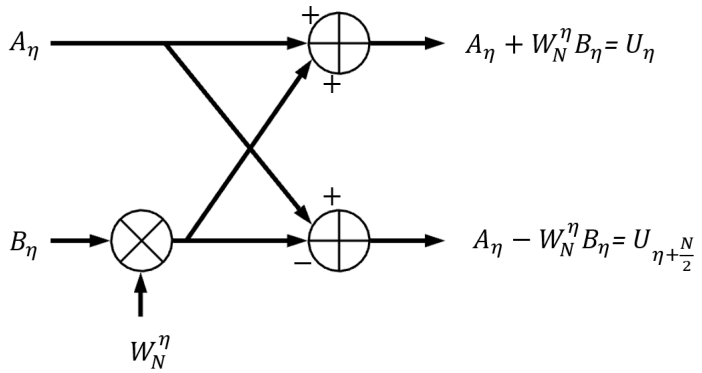

Figure A.1: The butterfly structure of the FFT

In Fig. A.2, the FFT scheme is shown for the case where the sample number is 8. As

shown, DFTs are formed by dividing the data into two continuously. This example is valid when the number of data is a power of 2.

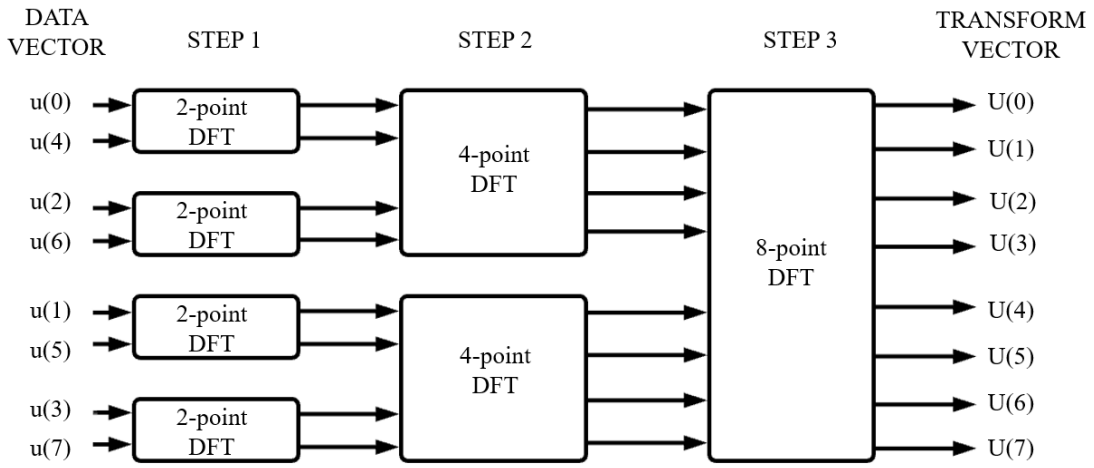

Figure A.2: The scheme of the FFT for $N = 8$

It is also possible to use FFT when the number of samples does not have a power of 2. For example, Fourier transform can be applied for any number of samples with Matlab's *"fft"* command. In this case, the logic of applying the method is the same. However, the contents of the smaller number of DFTs divided are different.

APPENDIX B

RESULT TABLES OF CASES OF DOGAN ET AL.

B.1 Dogan et al.-Case 0

Table B.1: Results of Dogan et al.-Case 0-Point 0A (from raw data of Dogan et al. [27])

$\overline{U}$ =4.691 m/s	I_{act}=0.2188	n=4.625	B=0.3333
u' =102.7 cm/s	I_{calc}=0.2188	$P(1)$=0.3910	A=0.9693

f Hz	ΔG -	x -	k cm^{-1}	L cm	$P_R(x)$ -	$P_L(x)$ -
0		-	-	-	0.3910	0.3910
	0.0137					
1		0.3746	0.2451	4.080	0.3847	0.3493
	0.0128					
2		0.4719	0.3897	2.566	0.3743	0.3327
	0.0354					
5		0.6349	0.7215	1.386	0.3493	0.3016
	0.0604					
10		0.8087	1.146	0.8730	0.3138	0.2656
	0.1022					
20		1.012	1.818	0.5501	0.2640	0.2224
	0.1879					
50		1.282	3.419	0.2925	0.1927	0.1678
	0.1623					
100		1.493	5.625	0.1778	0.1399	0.1297
	0.1678					
200		1.707	9.450	0.1058	0.0941	0.0967
	0.1804					
500		1.948	19.50	0.0513	0.0548	0.0666
	0.0598					
1000		2.059	34.78	0.0288	0.0412	0.0552
	0.0153					
2000		2.094	64.25	0.0156	0.0374	0.0518
	0.0019					
5000		2.099	151.8	0.0066	0.0369	0.0514
	0.00002					
10000		2.099	297.6	0.0034	0.0369	0.0514

Table B.2: Results of Dogan et al.-Case 0-Point 0B (from raw data of Dogan et al. [27])

$\overline{U}$ =7.157 m/s	I_{act}=0.1030	n=11.09	B=0.2812
u' =73.74 cm/s	I_{calc}=0.1030	$P(1)$=0.3998	A=0.9668

f	ΔG	x	k	L	$P_R(x)$	$P_L(x)$
Hz	-	-	cm^{-1}	cm	-	-
0		-	-	-	0.3998	0.3998
	0.0209					
1		0.4280	0.2770	3.610	0.4231	0.3177
	0.0154					
2		0.5200	0.4568	2.189	0.4161	0.2971
	0.0450					
5		0.6906	0.8791	1.138	0.3905	0.2589
	0.0781					
10		0.8795	1.422	0.7033	0.3442	0.2181
	0.1273					
20		1.097	2.284	0.4379	0.2735	0.1751
	0.1970					
50		1.359	4.366	0.2291	0.1797	0.1311
	0.1554					
100		1.564	7.280	0.1374	0.1132	0.1026
	0.1428					
200		1.768	12.39	0.0807	0.0625	0.0793
	0.1347					
500		1.990	26.00	0.0385	0.0272	0.0590
	0.0565					
1000		2.126	46.70	0.0214	0.0147	0.0490
	0.0223					
2000		2.196	86.13	0.0116	0.0104	0.0444
	0.0045					
5000		2.212	202.1	0.0049	0.0095	0.0434
	0.00009					
10000		2.213	394.7	0.0025	0.0095	0.0433

Table B.3: Results of Dogan et al.-Case 0-Point 0C (from raw data of Dogan et al. [27])

$\overline{U}$ =9.457 m/s	I_{act}=0.0448	n=27.21	B=0.1489
u' =42.38 cm/s	I_{calc}=0.0448	$P(1)$=0.4056	A=0.9822

f	ΔG	x	k	L	$P_R(x)$	$P_L(x)$
Hz	-	-	cm^{-1}	cm	-	-
0		-	-	-	0.4056	0.4056
	0.0314					
1		0.4877	0.3572	2.800	0.4472	0.2932
	0.0105					
2		0.5407	0.6455	1.549	0.4433	0.2804
	0.0286					
5		0.6507	1.392	0.7183	0.4288	0.2544
	0.0467					
10		0.7811	2.428	0.4119	0.4002	0.2250
	0.0944					
20		0.9695	4.122	0.2426	0.3393	0.1861
	0.2088					
50		1.260	8.112	0.1233	0.2177	0.1358
	0.1960					
100		1.509	13.47	0.0743	0.1175	0.1017
	0.1672					
200		1.746	22.58	0.0443	0.0501	0.0763
	0.1419					
500		1.999	46.34	0.0216	0.0139	0.0555
	0.0525					
1000		2.151	82.06	0.0122	0.0051	0.0456
	0.0185					
2000		2.223	149.8	0.0067	0.0030	0.0416
	0.0032					
5000		2.237	349.3	0.0029	0.0026	0.0408
	0.00006					
10000		2.238	680.6	0.0015	0.0026	0.0408

Table B.4: Results of Dogan et al.-Case 0-Point 0D (from raw data of Dogan et al. [27])

$\overline{U}$ =10.11 m/s	I_{act}=0.0070	n=180.8	B=0.0340
u' =7.113 cm/s	I_{calc}=0.0070	$P(1)$=0.4099	A=0.9969

f	ΔG	x	k	L	$P_R(x)$	$P_L(x)$
Hz	-	-	cm^{-1}	cm	-	-
0		-	-	-	0.4099	0.4099
	0.9528					
1		1.516	0.6030	1.658	0.1021	0.0959
	0.0176					
2		1.553	1.179	0.8484	0.0892	0.0919
	0.0108					
5		1.576	2.873	0.3481	0.0812	0.0893
	0.0020					
10		1.581	5.670	0.1764	0.0797	0.0888
	0.0027					
20		1.587	11.25	0.0889	0.0777	0.0882
	0.0060					
50		1.601	27.87	0.0359	0.0733	0.0867
	0.0012					
100		1.604	55.42	0.0180	0.0724	0.0864
	0.0001					
200		1.605	110.5	0.0091	0.0723	0.0864
	0.00003					
500		1.605	275.6	0.0036	0.0723	0.0864
	0.00002					
1000		1.605	550.8	0.0018	0.0723	0.0864
	0.00002					
2000		1.605	1101	0.0009	0.0723	0.0864
	0.0001					
5000		1.605	2752	0.0004	0.0722	0.0863
	0.0004					
10000		1.606	5503	0.0002	0.0719	0.0862

B.2 Dogan et al.-Case 1

Table B.5: Results of Dogan et al.-Case 1-Point 1A (from raw data of Dogan et al. [27])

$\overline{U}$ =2.833 m/s	I_{act}=0.2743	n=3.496	B=0.3548
u' =77.71 cm/s	I_{calc}=0.2743	$P(1)$=0.3880	A=0.9900

f	ΔG	x	k	L	$P_R(x)$	$P_L(x)$
Hz	-	-	cm^{-1}	cm	-	-
0		-	-	-	0.3880	0.3880
	0.0490					
1		0.5744	0.2182	4.583	0.3396	0.3292
	0.0467					
2		0.7345	0.3417	2.926	0.3092	0.2989
	0.1007					
5		0.9573	0.6285	1.591	0.2599	0.2518
	0.0960					
10		1.122	1.017	0.9829	0.2210	0.2157
	0.1243					
20		1.302	1.685	0.5936	0.1788	0.1769
	0.2086					
50		1.558	3.381	0.2958	0.1241	0.1265
	0.1601					
100		1.762	5.817	0.1719	0.0876	0.0919
	0.1286					
200		1.945	10.18	0.0982	0.0614	0.0662
	0.0748					
500		2.075	22.25	0.0450	0.0464	0.0510
	0.0101					
1000		2.098	41.63	0.0240	0.0441	0.0486
	0.0011					
2000		2.100	80.15	0.0125	0.0438	0.0483
	0.00005					
5000		2.101	195.6	0.0051	0.0438	0.0483
	0.000001					
10000		2.101	388.1	0.0026	0.0438	0.0483

Table B.6: Results of Dogan et al.-Case 1-Point 1B (from raw data of Dogan et al. [27])

$\overline{U}$ =4.294 m/s	I_{act}=0.1439	n=7.599	B=0.3408
u' =61.80 cm/s	I_{calc}=0.1439	$P(1)$=0.3963	A=0.9621

f	ΔG	x	k	L	$P_R(x)$	$P_L(x)$
Hz	-	-	cm^{-1}	cm	-	-
0		-	-	-	0.3963	0.3963
	0.0968					
1		0.7156	0.2155	4.640	0.3658	0.2639
	0.0818					
2		0.9063	0.3409	2.933	0.3194	0.2232
	0.1521					
5		1.153	0.6371	1.570	0.2446	0.1743
	0.1180					
10		1.323	1.048	0.9544	0.1903	0.1445
	0.1037					
20		1.468	1.776	0.5630	0.1460	0.1216
	0.1388					
50		1.656	3.729	0.2682	0.0963	0.0960
	0.1071					
100		1.818	6.655	0.1503	0.0623	0.0773
	0.0941					
200		1.981	12.01	0.0833	0.0373	0.0615
	0.0799					
500		2.144	26.80	0.0373	0.0204	0.0483
	0.0224					
1000		2.208	50.16	0.0199	0.0157	0.0438
	0.0049					
2000		2.225	96.02	0.0104	0.0146	0.0427
	0.0004					
5000		2.226	233.1	0.0043	0.0145	0.0426
	0.000004					
10000		2.226	461.4	0.0022	0.0145	0.0426

Table B.7: Results of Dogan et al.-Case 1-Point 1C (from raw data of Dogan et al. [27])

$\overline{U}$ =5.711 m/s	I_{act}=0.0926	n=12.49	B=0.3575
u' =52.88 cm/s	I_{calc}=0.0926	$P(1)$=0.4008	A=0.9688

f	ΔG	x	k	L	$P_R(x)$	$P_L(x)$
Hz	-	-	cm^{-1}	cm	-	-
0		-	-	-	0.4008	0.4008
	0.1563					
1		0.8363	0.2211	4.522	0.3612	0.2246
	0.1328					
2		1.071	0.3457	2.893	0.2856	0.1776
	0.2204					
5		1.360	0.6390	1.565	0.1791	0.1292
	0.1423					
10		1.552	1.047	0.9550	0.1150	0.1028
	0.1126					
20		1.720	1.774	0.5638	0.0701	0.0834
	0.1016					
50		1.894	3.747	0.2669	0.0375	0.0666
	0.0554					
100		2.017	6.785	0.1474	0.0221	0.0565
	0.0405					
200		2.124	12.52	0.0798	0.0131	0.0488
	0.0298					
500		2.218	28.94	0.0345	0.0079	0.0429
	0.0071					
1000		2.245	55.57	0.0180	0.0067	0.0413
	0.0012					
2000		2.250	108.5	0.0092	0.0066	0.0410
	0.00008					
5000		2.250	266.9	0.0037	0.0065	0.0410
	0.000004					
10000		2.250	530.9	0.0019	0.0065	0.0410

Table B.8: Results of Dogan et al.-Case 1-Point 1D (from raw data of Dogan et al. [27])

$\overline{U}$ =6.126 m/s	I_{act}=0.0735	n=16.06	B=0.3526
u' =45.03 cm/s	I_{calc}=0.0735	$P(1)$=0.4026	A=0.9734

f	ΔG	x	k	L	$P_R(x)$	$P_L(x)$
Hz	-	-	cm^{-1}	cm	-	-
0		-	-	-	0.4026	0.4026
	0.1282					
1		0.7817	0.2757	3.627	0.3851	0.2316
	0.1109					
2		0.9981	0.4325	2.312	0.3181	0.1871
	0.2265					
5		1.314	0.7946	1.259	0.1958	0.1327
	0.1735					
10		1.539	1.284	0.7790	0.1146	0.1018
	0.1211					
20		1.721	2.140	0.4673	0.0647	0.0815
	0.1077					
50		1.909	4.447	0.2249	0.0304	0.0641
	0.0552					
100		2.034	7.986	0.1252	0.0166	0.0544
	0.0373					
200		2.142	14.67	0.0682	0.0091	0.0471
	0.0262					
500		2.231	33.81	0.0296	0.0052	0.0418
	0.0056					
1000		2.255	64.91	0.0154	0.0045	0.0405
	0.0008					
2000		2.258	126.8	0.0079	0.0044	0.0403
	0.00004					
5000		2.258	312.1	0.0032	0.0044	0.0403
	0.000007					
10000		2.258	621.0	0.0016	0.0044	0.0403

B.3 Dogan et al.-Case 2

Table B.9: Results of Dogan et al.-Case 2-Point 2A (from raw data of Dogan et al. [27])

$\overline{U}$ =3.826 m/s	I_{act}=0.2867	n=3.306	B=0.3430
u' =109.7 cm/s	I_{calc}=0.2867	$P(1)$=0.3874	A=0.9967

f	ΔG	x	k	L	$P_R(x)$	$P_L(x)$
Hz	-	-	cm^{-1}	cm	-	-
0		-	-	-	0.3874	0.3874
	0.0649					
1		0.6310	0.1381	7.239	0.3252	0.3229
	0.0575					
2		0.8004	0.2182	4.584	0.2910	0.2897
	0.1187					
5		1.033	0.4056	2.465	0.2386	0.2393
	0.1044					
10		1.198	0.6624	1.510	0.2003	0.2026
	0.1037					
20		1.347	1.113	0.8989	0.1669	0.1704
	0.1515					
50		1.542	2.302	0.4344	0.1266	0.1310
	0.1270					
100		1.710	4.063	0.2461	0.0965	0.1009
	0.1237					
200		1.882	7.252	0.1379	0.0706	0.0743
	0.1105					
500		2.053	15.98	0.0626	0.0499	0.0524
	0.0305					
1000		2.118	29.71	0.0337	0.0434	0.0453
	0.0067					
2000		2.134	56.65	0.0177	0.0418	0.0436
	0.0008					
5000		2.136	137.1	0.0073	0.0416	0.0434
	0.00001					
10000		2.136	271.2	0.0037	0.0416	0.0434

Table B.10: Results of Dogan et al.-Case 2-Point 2B (from raw data of Dogan et al. [27])

$\overline{U}$ =5.543 m/s	I_{act}=0.1769	n=5.973	B=0.3317
u' =98.03 cm/s	I_{calc}=0.1769	$P(1)$=0.3938	A=0.9626

f	ΔG	x	k	L	$P_R(x)$	$P_L(x)$
Hz	-	-	cm^{-1}	cm	-	-
0		-	-	-	0.3938	0.3938
	0.1084					
1		0.7446	0.1288	7.764	0.3450	0.2667
	0.0865					
2		0.9371	0.2050	4.877	0.2982	0.2259
	0.1829					
5		1.216	0.3836	2.607	0.2183	0.1704
	0.1335					
10		1.400	0.6287	1.591	0.1654	0.1380
	0.1069					
20		1.548	1.064	0.9402	0.1262	0.1149
	0.1127					
50		1.706	2.245	0.4453	0.0900	0.0931
	0.0777					
100		1.829	4.058	0.2464	0.0665	0.0783
	0.0720					
200		1.954	7.447	0.1343	0.0472	0.0651
	0.0742					
500		2.096	16.94	0.0590	0.0305	0.0523
	0.0312					
1000		2.172	31.96	0.0313	0.0236	0.0462
	0.0116					
2000		2.206	61.24	0.0163	0.0210	0.0437
	0.0023					
5000		2.213	148.3	0.0067	0.0204	0.0432
	0.0001					
10000		2.213	293.1	0.0034	0.0204	0.0432

Table B.11: Results of Dogan et al.-Case 2-Point 2C (from raw data of Dogan et al. [27])

$\overline{U}$ =7.349 m/s	I_{act}=0.1380	n=7.976	B=0.3441
u' =101.4 cm/s	I_{calc}=0.1380	$P(1)$=0.3968	A=0.9625

f	ΔG	x	k	L	$P_R(x)$	$P_L(x)$
Hz	-	-	cm^{-1}	cm	-	-
0		-	-	-	0.3968	0.3968
	0.1431					
1		0.8148	0.1159	8.626	0.3459	0.2409
	0.1159					
2		1.034	0.1829	5.466	0.2839	0.1956
	0.2505					
5		1.362	0.3381	2.958	0.1783	0.1370
	0.1619					
10		1.573	0.5492	1.821	0.1164	0.1061
	0.1092					
20		1.732	0.9241	1.082	0.0781	0.0863
	0.0930					
50		1.884	1.952	0.5123	0.0498	0.0702
	0.0476					
100		1.981	3.555	0.2813	0.0360	0.0613
	0.0338					
200		2.060	6.621	0.1510	0.0270	0.0547
	0.0294					
500		2.135	15.48	0.0646	0.0201	0.0489
	0.0112					
1000		2.169	29.88	0.0335	0.0175	0.0465
	0.0038					
2000		2.181	58.36	0.0171	0.0166	0.0457
	0.0006					
5000		2.184	143.5	0.0070	0.0164	0.0455
	0.00001					
10000		2.184	285.4	0.0035	0.0164	0.0455

Table B.12: Results of Dogan et al.-Case 2-Point 2D (from raw data of Dogan et al. [27])

$\overline{U}$ =7.982 m/s	I_{act}=0.1187	n=9.468	B=0.3144
u' =94.74 cm/s	I_{calc}=0.1187	$P(1)$=0.3984	A=0.9643

f	ΔG	x	k	L	$P_R(x)$	$P_L(x)$
Hz	-	-	cm^{-1}	cm	-	-
0		-	-	-	0.3984	0.3984
	0.1292					
1		0.7864	0.1230	8.130	0.3617	0.2419
	0.0940					
2		0.9778	0.1982	5.046	0.3082	0.2020
	0.2094					
5		1.272	0.3751	2.666	0.2094	0.1480
	0.1729					
10		1.496	0.6148	1.627	0.1360	0.1139
	0.1353					
20		1.683	1.032	0.9689	0.0851	0.0901
	0.1184					
50		1.867	2.153	0.4645	0.0481	0.0707
	0.0562					
100		1.982	3.876	0.2580	0.0317	0.0604
	0.0378					
200		2.073	7.147	0.1399	0.0220	0.0532
	0.0318					
500		2.159	16.55	0.0604	0.0150	0.0470
	0.0121					
1000		2.199	31.77	0.0315	0.0125	0.0444
	0.0041					
2000		2.213	61.84	0.0162	0.0116	0.0435
	0.0007					
5000		2.216	151.7	0.0066	0.0115	0.0433
	0.00001					
10000		2.216	301.3	0.0033	0.0115	0.0433

APPENDIX C

RESULT TABLES OF CASES OF ABDULRAHIM ET AL.

C.1 Abdulrahim et al.-Case 3

Table C.1: Results of Abdulrahim et al.-Case 3-Point 3A (from raw data of Abdulrahim et al. [1])

$\overline{U}$ =7.117 m/s	I_{act}=0.1320	n=8.389	B=0.3241
u' =94.63 cm/s	I_{calc}=0.1320	$P(1)$=0.3972	A=0.9629

f	ΔG	x	k	L	$P_R(x)$	$P_L(x)$
Hz	-	-	cm^{-1}	cm	-	-
0		-	-	-	0.3972	0.3972
	0.0313					
1		0.4909	0.2001	4.998	0.4060	0.3097
	0.0273					
2		0.6146	0.3202	3.123	0.3900	0.2828
	0.1043					
5		0.8852	0.5858	1.707	0.3301	0.2244
	0.1373					
10		1.117	0.9175	1.090	0.2592	0.1783
	0.1255					
20		1.298	1.467	0.6815	0.1992	0.1462
	0.1657					
50		1.514	2.884	0.3467	0.1320	0.1133
	0.1187					
100		1.682	4.962	0.2015	0.0882	0.0916
	0.1066					
200		1.848	8.724	0.1146	0.0545	0.0735
	0.1077					
500		2.037	18.98	0.0527	0.0282	0.0564
	0.0487					
1000		2.154	34.82	0.0287	0.0176	0.0476
	0.0212					
2000		2.218	65.20	0.0153	0.0133	0.0432
	0.0058					
5000		2.238	154.6	0.0065	0.0121	0.0419

Table C.2: Results of Abdulrahim et al.-Case 3-Point 3B (from raw data of Abdulrahim et al. [1])

$\overline{U}$ =9.560 m/s	I_{act}=0.0697	n=17.01	B=0.2957
u' =66.63 cm/s	I_{calc}=0.0697	$P(1)$=0.4030	A=0.9744

f	ΔG	x	k	L	$P_R(x)$	$P_L(x)$
Hz	-	-	cm^{-1}	cm	-	-
0		-	-	-	0.4030	0.4030
	0.0271					
1		0.4655	0.2877	3.476	0.4361	0.3031
	0.0212					
2		0.5714	0.4696	2.130	0.4269	0.2783
	0.0777					
5		0.8022	0.8815	1.135	0.3817	0.2263
	0.1242					
10		1.033	1.396	0.7166	0.3068	0.1797
	0.1573					
20		1.258	2.219	0.4506	0.2181	0.1407
	0.2198					
50		1.529	4.250	0.2353	0.1171	0.1026
	0.1389					
100		1.731	7.142	0.1400	0.0612	0.0801
	0.0974					
200		1.907	12.33	0.0811	0.0296	0.0640
	0.0846					
500		2.096	26.46	0.0378	0.0112	0.0500
	0.0351					
1000		2.207	48.37	0.0207	0.0057	0.0431
	0.0135					
2000		2.260	90.59	0.0110	0.0040	0.0401
	0.0032					
5000		2.274	215.4	0.0046	0.0036	0.0393

Table C.3: Results of Abdulrahim et al.-Case 3-Point 3C (from raw data of Abdulrahim et al. [1])

$\overline{U}$ =11.02 m/s	I_{act}=0.0055	n=229.9	B=0.1930
u' =6.107 cm/s	I_{calc}=0.0055	$P(1)$=0.4101	A=0.9975

f	ΔG	x	k	L	$P_R(x)$	$P_L(x)$
Hz	-	-	cm^{-1}	cm	-	-
0		-	-	-	0.4101	0.4101
	0.0581					
1		0.5967	2.137	0.4680	0.4597	0.2591
	0.0255					
2		0.6821	3.746	0.2670	0.4459	0.2387
	0.0666					
5		0.8443	7.791	0.1284	0.4022	0.2028
	0.1146					
10		1.044	13.24	0.0755	0.3210	0.1639
	0.1402					
20		1.245	22.23	0.0450	0.2230	0.1312
	0.1957					
50		1.494	44.77	0.0223	0.1098	0.0982
	0.1294					
100		1.696	77.02	0.0130	0.0472	0.0772
	0.1055					
200		1.907	134.1	0.0075	0.0139	0.0598
	0.0538					
500		2.066	289.5	0.0035	0.0042	0.0492
	0.0386					
1000		2.208	530.3	0.0019	0.0011	0.0412
	0.0259					
2000		2.319	985.0	0.0010	0.0003	0.0359
	0.0461					
5000		2.513	2263	0.0004	0.00002	0.0281

Table C.4: Results of Abdulrahim et al.-Case 3-Point 3D (from raw data of Abdulrahim et al. [1])

$\overline{U}$ =10.93 m/s	I_{act}=0.0052	n=244.9	B=0.1149
u' =5.691 cm/s	I_{calc}=0.0052	$P(1)$=0.4101	A=0.9977

f	ΔG	x	k	L	$P_R(x)$	$P_L(x)$
Hz	-	-	cm^{-1}	cm	-	-
0		-	-	-	0.4101	0.4101
	0.2916					
1		1.022	1.221	0.8190	0.3315	0.1680
	0.0502					
2		1.106	2.259	0.4427	0.2916	0.1531
	0.0827					
5		1.232	5.092	0.1964	0.2291	0.1330
	0.0709					
10		1.341	9.382	0.1066	0.1761	0.1174
	0.0845					
20		1.471	17.24	0.0580	0.1189	0.1009
	0.1054					
50		1.640	38.53	0.0260	0.0614	0.0826
	0.0796					
100		1.798	70.65	0.0142	0.0275	0.0683
	0.0647					
200		1.959	129.4	0.0077	0.0096	0.0561
	0.0458					
500		2.107	292.4	0.0034	0.0029	0.0467
	0.0426					
1000		2.267	544.8	0.0018	0.0006	0.0383
	0.0290					
2000		2.394	1019	0.0010	0.0001	0.0327
	0.0528					
5000		2.620	2340	0.0004	0.000003	0.0245

C.2 Abdulrahim et al.-Case 4

Table C.5: Results of Abdulrahim et al.-Case 4-Point 4A (from raw data of Abdulrahim et al. [1])

$\overline{U}$ =6.777 m/s	I_{act}=0.1388	n=7.926	B=0.3130
u' =94.02 cm/s	I_{calc}=0.1388	$P(1)$=0.3967	A=0.9624

f Hz	ΔG -	x -	k cm^{-1}	L cm	$P_R(x)$ -	$P_L(x)$ -
0		-	-	-	0.3967	0.3967
	0.1181					
1		0.7644	0.1272	7.859	0.3576	0.2519
	0.0864					
2		0.9496	0.2052	4.873	0.3091	0.2129
	0.1473					
5		1.181	0.3934	2.542	0.2368	0.1681
	0.1337					
10		1.367	0.6557	1.525	0.1767	0.1363
	0.1058					
20		1.515	1.119	0.8933	0.1323	0.1141
	0.1255					
50		1.690	2.370	0.4219	0.0874	0.0913
	0.0880					
100		1.832	4.268	0.2343	0.0588	0.0756
	0.0763					
200		1.970	7.783	0.1285	0.0376	0.0623
	0.0737					
500		2.123	17.58	0.0569	0.0212	0.0499
	0.0309					
1000		2.208	33.01	0.0303	0.0149	0.0439
	0.0116					
2000		2.246	63.01	0.0159	0.0126	0.0414
	0.0027					
5000		2.256	152.1	0.0066	0.0121	0.0408

Table C.6: Results of Abdulrahim et al.-Case 4-Point 4B (from raw data of Abdulrahim et al. [1])

$\overline{U}$ =8.420 m/s	I_{act}=0.0959	n=12.01	B=0.3202
u' =80.74 cm/s	I_{calc}=0.0959	$P(1)$=0.4004	A=0.9681

f	ΔG	x	k	L	$P_R(x)$	$P_L(x)$
Hz	-	-	cm^{-1}	cm	-	-
0		-	-	-	0.4004	0.4004
	0.1755					
1		0.8696	0.1316	7.596	0.3503	0.2184
	0.1248					
2		1.086	0.2113	4.734	0.2796	0.1757
	0.2078					
5		1.359	0.4022	2.486	0.1794	0.1298
	0.1220					
10		1.529	0.6717	1.489	0.1227	0.1062
	0.1158					
20		1.699	1.154	0.8666	0.0760	0.0860
	0.1067					
50		1.875	2.461	0.4064	0.0412	0.0685
	0.0539					
100		1.992	4.473	0.2236	0.0254	0.0586
	0.0402					
200		2.095	8.281	0.1208	0.0158	0.0509
	0.0355					
500		2.200	19.15	0.0522	0.0092	0.0440
	0.0128					
1000		2.246	36.66	0.0273	0.0071	0.0413
	0.0040					
2000		2.262	71.18	0.0140	0.0064	0.0403
	0.0008					
5000		2.265	174.3	0.0057	0.0063	0.0401

Table C.7: Results of Abdulrahim et al.-Case 4-Point 4C (from raw data of Abdulrahim et al. [1])

$\overline{U}$ =9.571 m/s	I_{act}=0.0711	n=16.64	B=0.3248
u' =68.08 cm/s	I_{calc}=0.0711	$P(1)$=0.4028	A=0.9740

f	ΔG	x	k	L	$P_R(x)$	$P_L(x)$
Hz	-	-	cm^{-1}	cm	-	-
0		-	-	-	0.4028	0.4028
	0.1296					
1		0.7844	0.1743	5.738	0.3856	0.2305
	0.0997					
2		0.9824	0.2788	3.587	0.3245	0.1896
	0.1895					
5		1.252	0.5266	1.899	0.2204	0.1419
	0.1890					
10		1.493	0.8629	1.159	0.1293	0.1073
	0.1401					
20		1.693	1.442	0.6934	0.0705	0.0841
	0.1142					
50		1.886	2.990	0.3345	0.0330	0.0659
	0.0521					
100		2.009	5.359	0.1866	0.0184	0.0562
	0.0380					
200		2.116	9.835	0.1017	0.0102	0.0487
	0.0325					
500		2.222	22.60	0.0442	0.0053	0.0423
	0.0113					
1000		2.267	43.16	0.0232	0.0039	0.0397
	0.0034					
2000		2.282	83.74	0.0119	0.0035	0.0389
	0.0008					
5000		2.286	205.0	0.0049	0.0034	0.0388

Table C.8: Results of Abdulrahim et al.-Case 4-Point 4D (from raw data of Abdulrahim et al. [1])

$\overline{U}$ =10.93 m/s	I_{act}=0.0211	n=59.38	B=0.4284
u' =23.05 cm/s	I_{calc}=0.0211	$P(1)$=0.4082	A=0.9910

f	ΔG	x	k	L	$P_R(x)$	$P_L(x)$
Hz	-	-	cm^{-1}	cm	-	-
0		-	-	-	0.4082	0.4082
	0.0413					
1		0.5335	0.8941	1.118	0.4569	0.2776
	0.0535					
2		0.7179	1.330	0.7520	0.4291	0.2338
	0.1273					
5		0.9754	2.296	0.4356	0.3460	0.1799
	0.1559					
10		1.204	3.547	0.2819	0.2432	0.1402
	0.1815					
20		1.439	5.610	0.1783	0.1371	0.1070
	0.1847					
50		1.691	10.84	0.0923	0.0542	0.0793
	0.0996					
100		1.883	18.46	0.0542	0.0201	0.0627
	0.0688					
200		2.062	32.28	0.0310	0.0060	0.0501
	0.0589					
500		2.255	70.17	0.0143	0.0011	0.0393
	0.0187					
1000		2.338	129.5	0.0077	0.0005	0.0354
	0.0064					
2000		2.370	245.4	0.0041	0.0003	0.0340
	0.0035					
5000		2.387	589.3	0.0017	0.0003	0.0332